Stochastic optimization of fiber reinforced composites considering uncertainties

Stochastische Optimierung der Faserparameter in Faserverbundwerkstoffen unter Bercksichtigung Unsicherheiten

DISSERTATION

Zur Erlangung des akademischen Grades eines

Doktor-Ingenieur

an der Fakultät Bauingenieurwesen

der Bauhaus-Universität Weimar

vorgelegt von

M.Sc. Hamid Ghasemi Meyghani

(interner Doktorand)

geboren am 06. Juni 1981 in

Arak, Iran

Mentor: Prof. Dr.-Ing. Timon Rabczuk

Weimar, Mai 2016

To my wife and my little daughter ...

Acknowledgements

Hamid Ghasemi
Weimar, Germany
May 2016

Abstract

Briefly, the two basic questions that this research is supposed to answer are:

1. How much fiber is needed and how fibers should be distributed through a fiber reinforced composite (FRC) structure in order to obtain the optimal and reliable structural response?

2. How do uncertainties influence the optimization results and reliability of the structure?

Giving answer to the above questions a double stage sequential optimization algorithm for finding the optimal content of short fiber reinforcements and their distribution in the composite structure, considering uncertain design parameters, is presented. In the first stage, the optimal amount of short fibers in a FRC structure with uniformly distributed fibers is conducted in the framework of a Reliability Based Design Optimization (RBDO) problem. Presented model considers material, structural and modeling uncertainties. In the second stage, the fiber distribution optimization (with the aim to further increase in structural reliability) is performed by defining a fiber distribution function through a Non-Uniform Rational B-Spline (NURBS) surface. The advantages of using the NURBS surface as a fiber distribution function include: using the same data set for the optimization and analysis; high convergence rate due to the smoothness of the NURBS; mesh independency of the optimal layout; no need for any post processing technique and its non-heuristic nature. The output of stage 1 (the optimal fiber content for homogeneously distributed fibers) is considered as the input of stage 2. The output of stage 2 is the Reliability Index (β) of the structure with the optimal fiber content and distribution. First order reliability method (in order to approximate the limit state function) as well as different material models including Rule of Mixtures, Mori-Tanaka, energy-based approach and stochastic multi-scales are implemented in different examples. The proposed combined model is able to capture the role of available uncertainties in FRC structures through a computationally efficient algorithm using all sequential, NURBS and sensitivity based techniques. The methodology is successfully implemented for interfacial shear stress optimization in sandwich beams and also for optimization of the internal cooling channels in a ceramic matrix composite.

Finally, after some changes and modifications by combining Isogeometric Analysis, level set and point wise density mapping techniques, the computational framework is extended for topology optimization of piezoelectric / flexoelectric materials.

Contents

List of Figures

List of Tables

Chapter 1

Introduction

1.1 Motivation

Fiber Reinforced Composite (FRC) materials have been heavily investigated in the last decades and are widely used in advanced applications such as aerospace, structural, military and transportation industries due to their elevated mechanical properties values to weight (or cost) ratio. Thanks to their excellent structural qualities like high strength, fracture toughness, fatigue resistance, light weight, erosion and corrosion resistance, a particular interest has been born not only in engineers for the use of FRCs in advanced industrial applications, but also in researchers to develop and optimize their particular and useful characteristics.

The general behavior of a FRC depends on the characteristics of the composite constituents such as fiber reinforcements, resin and additives; each of these constituents has an important role in the composite characteristics and such aspects have driven some researchers to combine them differently for obtaining enhanced materials. Regardless of the roles of resins and additives which are out of the scope of this research, the mechanical properties of composites depend on many fiber's variables such as fiber's material, volume fraction, size and mesostructure. This latter aspect which deals with fiber configuration, orientation, layout and dispersion is an almost open issue in the literature. Generally, increasing the fiber volume fraction in a FRC composite will increase its structural strength and stiffness. However the existence of a practical upper limit should be considered. Normally, composite structural elements under mechanical actions have some regions which are on the edge of design constraints (e.g. the maximum allowable stress is exceeded) and can be identified as failure zones. Usually these failure zones dictate the required content of the reinforcing element in order to get a properly strengthened overall structure, fulfilling everywhere the design constraints. Considering uniform distribution of fibers through the structure, initially safe regions that already fulfill the design constraints will inevitably increase

their fiber content. Thus, an efficient optimization approach which seeks towards optimal fiber content should also pay attention to optimal distribution of fibers in order to strengthen only those portions of the structure (failure zones) for which it is necessary to improve their bearing capacity. From the above discussions it appears that the joint manipulation of these two parameters (i.e. fiber content and its distribution) will be a necessary approach towards more efficient and reliable structural optimization. Previous researches aimed at the optimization of composite's performance with respect to the above mentioned fiber related variables, have been focused on improving specific performance of a classical laminated or Functionally Graded (FG) composites by changing the fiber's layout (ply orientation) or fiber volume fraction, by using heuristic optimization methods, especially the so-called Genetic Algorithm (GA). Basically, the use of evolutionary algorithms, such as GA in [Brighenti, 2005], often leads to some limitations; in fact it is well-known as GA is problematic in some issues. Among them, its heuristic nature, high computational cost and sometimes the tendency to converge towards local optima instead of global optima- if proper so-called mutation strategies are not considered in the method- can be counted.

The present research aims to develop a computational platform for fiber distribution optimization within the matrix material in order to obtain enhanced structural behavior. In order to smoothly approximate given set of nodal points, the idea of utilizing Non-Uniform Rational B-Spline (NURBS) basis functions has been developed. Useful characteristics of NURBS basis functions - such as compact support and higher order elements - not only provides mesh independent distribution results but also makes it possible to use coarse meshes to decrease computational time, while maintaining the accuracy of the results. Moreover instead of using heuristic optimization methods, the sensitivity based method which uses gradient of the objective function evaluated with respect to design variables to find next direction in searching process (tending toward the optimum point), is implemented. Such an approach shows lots of merit particularly for complex geometries such as those often used in industrial applications.

Actual characteristics of a composite material involve many uncertainties. These emanate from a variety of sources such as constituent material properties, manufacturing and process imperfections, loading conditions and geometry. Neglecting the role of uncertainties in composite materials might result in either unsafe or unnecessary conservative design. This issue is addressed in the present approach within the framework of a Reliability Based Design Optimization (RBDO) problem. Taking into account of above, this research presents a comprehensive optimization package for composite materials which uses NURBS basis functions; works based on sensitivity analysis and capture available uncertainties aiming to obtain optimal content and distribution of fibers inside the matrix.

1.2   Literature Review

FRC materials have been heavily investigated in the last decades. Available literatures aimed at the optimization of composite's performance with respect to the fiber related variables, have been focused on improving specific performance of a classical laminated or FG composites by changing the fiber's layout (ply orientation) or fiber volume fraction, by using heuristic optimization methods such as GA [Almeida & Awruch, 2009; Apalak & Yildirim, 2008; Kim & Lim, 2013; Lee & Morillo, 2012;Lee & Kweon, 2013; Omkar & Mudigere, 2008; Zehnder & Ermanni, 2006]. Salzar, 1995 tried to optimize a pressurized cylindrical pressure vessel by functionally grading the fiber volume fraction through the thickness of vessel. The work of Nadeau & Ferrari, 1999 addressed microstructural optimization of a FG layer subjected to thermal gradient, assuming that its parameters vary through the thickness of the layer; in their work the microstructure was characterized by fiber volume fraction, aspect ratio and orientation distribution. Honda & Narita, 2011 optimized vibration characteristics of a laminated structure by changing the orientation of fibers and intentionally providing local anisotropy; in their work fiber orientation angle and GA were implemented as design variable and optimization methodology respectively. Murugan & Flores, 2012 performed optimization to minimize the in-plane stiffness and maximize the out of plane bending stiffness of a morphing skin used in aircraft wing made of laminate composite, by spatially varying the volume fraction of the fibers in the different layers; in particular the laminate was discretized through its thickness and equivalent material properties in each element were obtained based on homogenization technique using multi-scale constitutive model. Smooth particle hydrodynamics was implemented in Kulasegaram *et al.*, 2011 and Kulasegaram & Karihaloo, 2012 works in order to model and optimize short steel fibers distribution and orientation in self compacting concrete flow. Huang & Haftka, 2005 tried to optimize fibers orientation (not their distribution) near a hole in a single layer of multilayer composite laminates in order to increase the load caring capacity by GA. Brighenti in [2004c, 2006 and 2007] used GA in his series of works on fiber distribution and patch repair optimization for cracked plates (to get the maximum exploitation of a given available patch element area by determining its best conformation around the cracked zone). The presence of the patch in a point of the structure is accounted for by properly modifying (i.e. increasing) the elastic modulus, similarly to what has been done with fiber distribution optimization in FRC material [Brighenti, 2005]. In particular the optimum distribution of the short fibers in a FRC, obtained by using GA, has been usually addressed in the literatures by assuming a constant value of the total fiber content, the optimum layout for fiber distribution has been determined in order to fulfill some given objective functions.

The characteristics of composite materials are influenced by many uncertainties. There are some methods for considering the role of uncertainties in design performance. One of these methods is the so-called RBDO which tries to find optimal per-

formance considering some probabilistic design constraints. Motivated by capabilities of RBDO in uncertainty quantification, some researchers have implemented it in the design of composite structures. Though there are some exceptions, most of these researches are related to composite laminates. However, to the knowledge of the author, the solid FRC structures are not thoroughly explored. Thanedar & Chamis, 1995 developed a procedure for the tailoring of layered composite laminates subjected to probabilistic constraints and loads. The work of Jiang *et al.*, 2008 suggested a methodology to optimize the plies orientations of a composite laminated plate having uncertain material properties. Gomes & Awruch, 2011 addressed the problem of composite laminate optimization by using GA and Artificial Neural Networks (ANN); while Antonio & Hoffbauer, 2009 presented reliability based robust design optimization methodology. Noh & Kang., 2013 have implemented RBDO methodology for purpose of optimizing volume fraction in a FG laminate composite.

Uncertainty propagation in nanocomposite structures remains an unsolved issue. Rouhi & Rais-Rohani, 2013 measured the failure probability of a nanocomposite cylinder under buckling, accounting for uncertain design conditions. However, they used micromechanical equations at the nano-scale by simply replacing the lattice structure of a Carbon Nano Tube (CNT) with a solid fiber (which can lead to inappropriate results Shokrieh & Rafiee, 2010c). Moreover, they disregard several important CNT parameters such as the CNT length, diameter, agglomeration and dispersion without any sensitivity evaluation. Furthermore, modeling errors including discretization- and approximation errors have not been addressed in detail.

1.3 Objectives of the dissertation

The final goal of this research is presentation of an efficient computational algorithm enabling to find both optimal content and distribution of fiber reinforcements within the structure encountering with uncertainties in design conditions. This algorithm can be implemented for complex geometries with different material models and multiphysics.

1.4 Innovations of the dissertation

The novelties of the present work can be pointed out within five categories: 1) utilizing NURBS basis functions for fiber distribution optimization in FRC structures using gradient-based approach which its advantages are already illustrated; 2) investigating the role of available uncertainties in composites on reliability of the structure. These uncertainties are classified in three major groups of material, structural and modeling uncertainties; 3) presenting the sequential optimization approach which is computa-

tionally efficient and links RBDO and fiber distribution optimization; 4) implementing the methodology in innovative applications including interfacial shear stress optimization in sandwich beam and optimization of internal cooling channels in Ceramic Matrix Composite (CMC); 5) adopting the computational framework for topology optimization of piezoelectric / flexoelectric materials.

1.5   Outline

In the previous sections, the topic, objective, innovations, literature review and methodology of the thesis are introduced. The remainder of this dissertation is organized as follows:

Chapter 2 contains fundamental formulations of Isogeometric Analysis (IGA) and NURBS basis functions which are used in this dissertation.

Chapter 3 deals with structural reliability concept. The notions of reliability assessment, RBDO and First Order Reliability Method (FORM) which are frequently used in this dissertation are introduced.

Chapter 4 deals with the optimization of short fibers distribution in continuum structures made of FRC by adopting an efficient gradient based optimization approach. NURBS basis functions have been implemented to define continuous and smooth mesh independent fiber distribution function as well as domain discretization. Some numerical examples related to the structural response under static loading as well as the free vibration behavior are conducted to demonstrate the capabilities of the model.

Chapter 5 focuses on the uncertainties propagation and their effects on reliability of polymeric nanocomposite (PNC) continuum structures, in the framework of the combined geometry and material optimization. Presented model considers material, structural and modeling uncertainties. The material model covers uncertainties at different length scales (from nano-, micro-, meso- to macro-scale) via a stochastic approach. It considers the length, waviness, agglomeration, orientation and dispersion (all as random variables) of CNTs within the polymer matrix. To increase the computational efficiency, the expensive-to-evaluate stochastic multi-scale material model has been surrogated by a kriging metamodel. This metamodel-based probabilistic optimization has been adopted in order to find the optimum value of the CNT content as well as the optimum geometry of the component as the objective function while the implicit finite element based design constraint is approximated by the first order reliability method. Illustrative examples are provided to demonstrate the effectiveness and applicability of the approach.

Chapter 6 presents double stage sequential optimization algorithm for finding the optimal fiber content and its distribution in solid composites, considering uncertain design parameters. In the first stage, the optimal amount of fiber in a FRC structure with uniformly distributed fibers is conducted in the framework of a RBDO problem. In the second stage, the fiber distribution optimization having the aim to more increase in structural reliability is performed by defining a fiber distribution function through a NURBS surface. Some case studies are performed to demonstrate the capabilities of the model.

Chapter 7 contains the first application of the methodology in sandwich beams with polymeric core to decrease interfacial stresses by presenting the optimal distribution of reinforcing ingredients in the polymeric matrix. This application aims at the local stress minimization within any arbitrary zone of the design domain. The core and face sheets are modeled as multi-patches and compatibility in the displacement field is enforced by the penalty method. An adjoint sensitivity method is devised to minimize the objective function within areas of interest defined over arbitrary regions in the design domain. The method is verified by several examples.

Chapter 8 contains the second application of the methodology for optimization of the internal cooling channels in Ceramic Matrix Composite (CMC) under thermal and mechanical loadings. The algorithm finds the optimal cooling capacity of all channels (which directly minimizes the amount of coolant needed). In the first step, available uncertainties in the constituent material properties, the applied mechanical load, the heat flux and the heat convection coefficient are considered. Using RBDO approach, the probabilistic constraints ensure the failure due to excessive temperature and deflection will not happen. The deterministic constraints restrict the capacity of any arbitrary cooling channel between two extreme limits. A series system reliability concept is adopted as a union of mechanical and thermal failure subsets. Having the results of the first step for CMC with uniformly distributed carbon (C-) fibers, the algorithm presents the optimal layout for distribution of the C-fibers inside the ceramic matrix in order to enhance the target reliability of the component. A sequential approach and B-spline finite elements have overcome the cumbersome computational burden. Numerical examples are presented.

Chapter 9 presents a design methodology based on a combination of IGA, level set and point wise density mapping techniques for topology optimization of piezoelectric / flexoelectric materials. The fourth order partial differential equations (PDEs) of flexoelectricity, which require at least C^1 continuous approximations, are discretized using NURBS. The point wise density mapping technique with consistent derivatives is directly used in the weak form of the governing equations. The boundary of the

design domain is implicitly represented by a level set function. The accuracy of the IGA model is confirmed through numerical examples including a cantilever beam under a point load and a truncated pyramid under compression with different electrical boundary conditions. Numerical examples demonstrate the usefulness of the method.

Chapter 10 summarizes the works and outlines the main contributions. Finally, some recommendations for future work are suggested.

Chapter 2

Fundamentals of NURBS

2.1   An introduction to Isogeometric Analysis

The main tool that is used by Computer Aided Design (CAD) for representation of the complex geometries is the Non-Uniform Rational B-spline (NURBS). Using NURBS, certain geometries including conic and circular sections, can be represented exactly. That is while polynomial shape functions are able to just approximate the geometries. The main idea behind the seminal work of Hughes *et al.*, 2005 was using NURBS not only for describing the geometry but also to construct finite approximations for analysis. The phrase 'Isogeometric Analysis' (IGA) was firstly used by Hughes *et al.* to unify CAD and Computer Aided Engineering (CAE). In the following fundamental formulations of IGA which are used in this dissertation are introduced. Readers are referred to [Cottrell *et al.*, 2009] to know more about IGA.

2.2   Knot vector

There are two different spaces in IGA named physical space and parameter space. Each element in the physical space is the image of a corresponding element in the parameter space, but the mapping itself is global to the whole patch, rather than to the elements themselves. The parameter space is discretized by knot vectors. A knot vector in one dimension is a non-decreasing set of coordinates in the parameter space, written $\Xi = \left\{ \xi_1, \xi_2, ..., \xi_{n+p+1} \right\}$, where $\xi_i \in R$ is the ith knot, i is the knot index, $i = 1, 2, ..., n + p + 1$, p is the polynomial order and n is the number of basis functions used to construct the B-spline curve. Element boundaries in the physical space are simply the images of knot lines under the B-spline mapping (See Fig. 2.1). Equally spaced knots in the parameter space provide uniform knot vectors, otherwise they are non-uniform. A knot vector is said to be open if its first and last knot values appear $p + 1$ times. Open knot vectors are the standard in the CAD literature. In one dimension, basis functions

a) Parent element   **b)** Parameter space   **c)** Physical space

d) Typical shape functions of order p and q

Figure 2.1: Different NURBS domains (a-c) and typical basis functions (d); Approximating nodal values of $\varphi_{i,j}$ defined on control points by using NURBS surface η_p (c)

formed from open knot vectors are interpolatory at the ends of the parameter space interval, $\left[\xi_1, \xi_{n+p+1}\right]$, and at the corners of patches in multiple dimensions, but they are not, in general, interpolatory at interior knots. This is a distinguishing feature between knots and nodes in finite element analysis (see[Cottrell *et al.*, 2009]).

2.3 NURBS functions and surfaces

2.3.1 NURBS basis functions and derivatives

NURBS basis is given by

$$R_i^p(\xi) = \frac{N_{i,p}(\xi)\, w_i}{W(\xi)} = \frac{N_{i,p}(\xi)\, w_i}{\sum_{i'=1}^{n} N_{i',p}(\xi)\, w_{i'}} \tag{2.1}$$

where $N_{i,p}(\xi)$ are B-spline basis functions recursively defined by using Coxde Boor formula and starting with piecewise constants ($p = 0$) [Cottrell *et al.*, 2009]

$$N_{i,0}(\xi) = \begin{cases} 1 & if\ \xi_i \leq \xi < \xi_{i+1} \\ 0 & otherwise \end{cases} \tag{2.2}$$

while for $p = 1, 2, 3, \ldots$.

$$N_{i,p}(\xi) = \frac{\xi - \xi_i}{\xi_{i+p} - \xi_i} N_{i,p-1}(\xi) + \frac{\xi_{i+p+1} - \xi}{\xi_{i+p+1} - \xi_{i+1}} N_{i+1,p-1}(\xi) \tag{2.3}$$

w_i is also referred to as the ith weight while $W(\xi)$ is weighting function defined as follows:

$$W(\xi) = \sum_{i=1}^{n} N_{i,p}(\xi) w_i \tag{2.4}$$

Simply applying the quotient rule to Eq. (2.1) yields:

$$\frac{d}{d\xi} R_i^p(\xi) = w_i \frac{W(\xi) N_{i,p}'(\xi) - W'(\xi) N_{i,p}(\xi)}{(W(\xi))^2} \tag{2.5}$$

where

$$N_{i,p}'(\xi) = \frac{p}{\xi_{i+p} - \xi_i} N_{i,p-1}(\xi) - \frac{p}{\xi_{i+p+1} - \xi_{i+1}} N_{i+1,p-1}(\xi) \tag{2.6}$$

and

$$W'(\xi) = \sum_{i=1}^{n} N'_{i,p}(\xi) w_i \tag{2.7}$$

Among NURBS basis functions characteristics, the most important ones are partition of unity property, compact support of each basis function and non-negative values. It can be also noted that if the weights are all equal, then $R_i^p(\xi) = N_{i,p}(\xi)$; so, B-spline is the special case of NURBS. Details related to higher order derivatives formulations can be found in [Cottrell *et al.*, 2009].

2.3.2 NURBS curves and surfaces

A NURBS curve is defined as:

$$C(\xi) = \sum_{i=1}^{n} R_i^p(\xi) B_i \tag{2.8}$$

where $B_i \in R^d$ are control points and $i = 1, 2, ..., n$, number of control points. Similarly, for definition of a NURBS surface, two knot vectors $\boldsymbol{E} = \left\{ \xi_1, \xi_2, ..., \xi_{n+p+1} \right\}$ and $\boldsymbol{H} = \left\{ \eta_1, \eta_2, ..., \eta_{m+q+1} \right\}$ (one for each direction) as well as a control net $B_{i,j}$ are required. A NURBS surface is defined as:

$$S(\xi, \eta) = \sum_{i=1}^{n} \sum_{j=1}^{m} R_{i,j}^{p,q}(\xi, \eta) B_{i,j} \tag{2.9}$$

where $R_{i,j}^{p,q}(\xi, \eta)$ is defined according to the following Eq. (2.10), while $N_{i,p}(\xi)$ and $M_{j,q}(\eta)$ are univariate B-spline basis functions of order p and q corresponding to knot vector $\boldsymbol{E}$ and $\boldsymbol{H}$, respectively.

$$R_{i,j}^{p,q}(\xi, \eta) = \frac{N_{i,p}(\xi) M_{j,q}(\eta) w_{i,j}}{\sum_{i'=1}^{n} \sum_{j'=1}^{m} N_{i',p}(\xi) M_{j',q}(\eta) w_{i',j'}} \tag{2.10}$$

Chapter 3

Structural reliability

3.1 Reliability assessment

The fundamentals of structural reliability are briefly presented below however, interested readers can refer to [Ditlevsen & Madsen, 1996] and references therein for more details. The structural reliability concept can be simply described by the example of a steel rod with constant cross sectional area under uniaxial tension (see Fig. 3.1). In the deterministic case, if the applied load (L) is less than rod strength (R), failure will not occur and the rod will be safe and the conventional safety factor index ($S.F = \frac{R}{L}$) is used to quantify the system level of confidence. In probabilistic case, (L) and (R) are not fixed values but instead they are random variables containing uncertainties. In this case $X(L)$ and $X(R)$ are non-negative independent random variables with Probability Density Functions (PDF) $f_L(x_L)$ and $f_R(x_R)$, respectively. In essence, for a vector of random variables $X = \{x_1,...,x_n\}^T$, the PDF can be calculated by $f_X(x) = \frac{d}{d_x}F_X(x)$, where $F_X(x)$ is the so called Cumulative Distribution Function (CDF) and relates the probability of a random event to a prescribed deterministic value x, (i.e. $F_X(x) = Prob\ X{<}x$).

In considering the rod example, the boundary between safe (*i.e.* $x_R{>}x_L$) and failure (*i.e.* $x_R{<}x_L$) regions can be defined by $g(x) = x_R - x_L$ which is called Limit State Function (LSF). Thus, $g(x) \leq 0$ denotes a subset of the space, where failure occurs.

The concept of Reliability Index (β) which has been proposed by Hasofer & Lind, 1974 requires standard normal non-correlated variables; so the transformations from correlated non-Gaussian variables X to uncorrelated Gaussian variables U (with zero means and unit standard deviations) is needed. According to this definition of β, the design point is chosen such as to maximize the PDF within the failure domain. Geometrically, it corresponds to the point in failure domain having the shortest distance from the origin of reduced variables to the limit state surface (i.e. $g(U) = 0$), as shown

in Fig. 3.1). Mathematically, it is a minimization problem with an equality constraint:

$$\begin{cases} \beta = \min \left(\boldsymbol{U}.\boldsymbol{U}^T \right)^{\frac{1}{2}} \\ s.t : \\ g \left(\boldsymbol{U} \right) = 0 \end{cases} \tag{3.1}$$

which leads to the Lagrangian function:

$$L = min\{\frac{1}{2}\boldsymbol{U}^T\boldsymbol{U} + \lambda g \left(\boldsymbol{U} \right)\} \tag{3.2}$$

The solution of Eq. (3.2) is called the Most Probable Point (MPP) and can be obtained by a standard optimization solver.
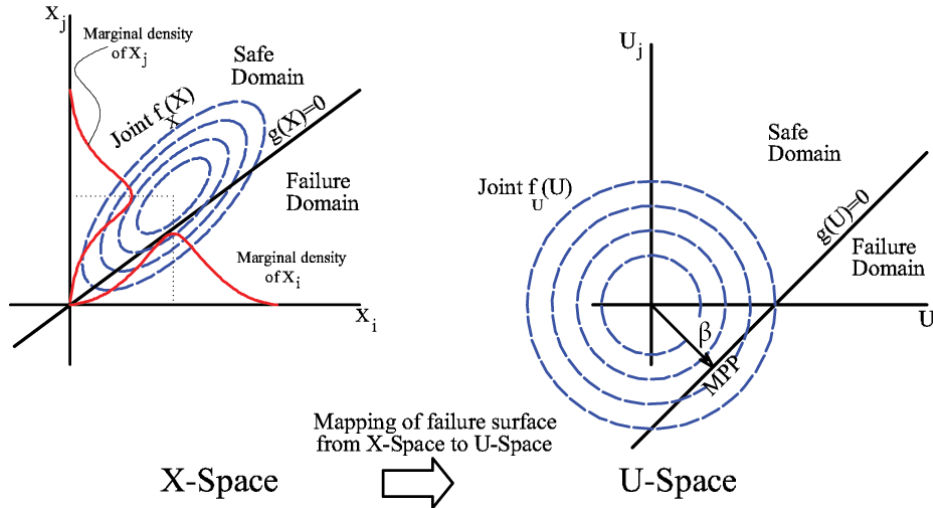
Figure 3.1: Structural reliability concept

The failure probability, P_f , can be measured by the probability integral as:

$$P_f = Prob\left[g \left(x \right) \leq 0\right] = \int_{x|g(x)\leq 0} f_X \left(x \right) dx \tag{3.3}$$

The evaluation of the integral in Eq. (3.3) (the fundamental equation of reliability analysis) in most cases is not an easy task and needs specific solution techniques. One approach is to analytically approximate this integral, in order to get simpler functions for P_f . Such techniques can be categorized into two major groups: First and Second Order Reliability Method (FORM and SORM) which respectively approximate LSF with the first order and the second order of Taylor expansion at the MPP (Fig. 3.1)).

There are also alternative methods for calculating the probability integral: among them Monte Carlo Method (MCM) may be the most important one since it is usually

used as the reference method due to its precision to calculate failure probability. Each of the above cited methods has advantages and disadvantages which should be considered precisely before implementation. For instance even though MCM is a precise method, it shows a serious drawback in the case of small values of the failure probability [Chiachio *et al.*, 2012]. Computational cost is another dominant parameter for selecting the appropriate solution method. Methods based on the SORM and MCM approaches are usually numerically more expensive in comparison with FORM. In practical problems an appropriate balance must be necessarily considered between accuracy and cost of the analysis. In the present work FORM has been implemented since it is suitable for cases with a small number of random variables. Such an approach is usually sufficiently accurate to be used for real applications of structural design [Zhao & Ono, 1999]. In the following, the implementation of the FORM is briefly described, however more details about available methods for structural reliability analysis can be found in [Chiachio *et al.*, 2012].
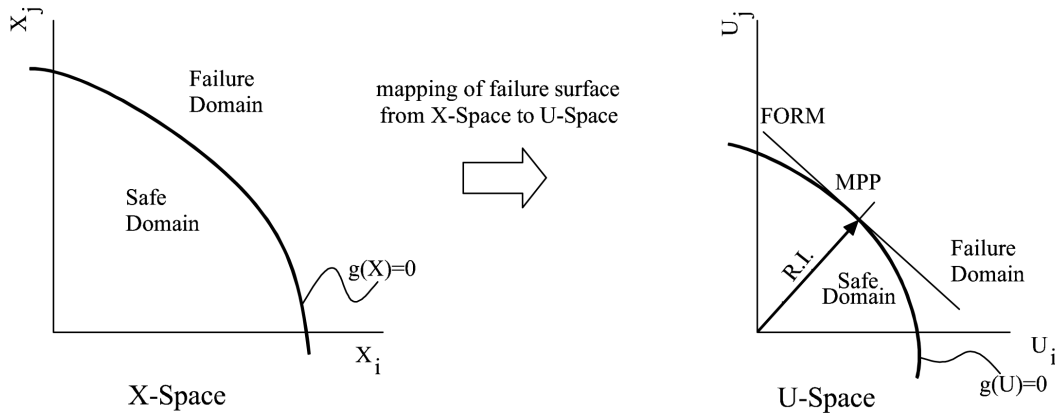
Figure 3.2: Graphical representation of the FORM approximation

3.1.1   First order reliability method (FORM)

The FORM approximation can be traced back to First Order Second Moment (FOSM) method which is based on first order Taylor series approximation of the LSF, linearized at the mean values of random variables, while a Second Moment statistics (means and covariances) is used. In this context the limit state function can be approximated as below:

$$g(x) = g(x_0) + \sum_{i=1}^{n} \frac{\partial g}{\partial x_i}\big|_{x=x_0}(x_i - x_{i0}) + \frac{1}{2}\sum_{i=1}^{n}\sum_{k=1}^{n}\frac{\partial^2 g}{\partial x_i \partial x_k}$$
$$\big|_{x=x_0}(x_i - x_{i0})(x_k - x_{k0}) + \dots \tag{3.4}$$

Terminating the series after the linear terms yields:

$$\mathbb{E}[Z] = \mathbb{E}[g(\boldsymbol{X})] = g(x_0) + \sum_{i=1}^{n} \frac{\partial g}{\partial x_i} \mathbb{E}[x_i - x_{i0}] \tag{3.5}$$

where $\mathbb{E}$ stands for expected value (or ensemble average) of a random quantity $g(\boldsymbol{X})$ and can be defined in terms of the probability density function of x as:

$$\mathbb{E}[g(\boldsymbol{X})] = \int_{-\infty}^{+\infty} g(x) f_X(x) \, dx \tag{3.6}$$

If the mean value vector $\overline{X}$ is chosen as the starting expansion point x_0 for the Taylor series, then $\mathbb{E}[Z] = g(x_0)$ and the variance becomes:

$$\sigma_Z^2 = \mathbb{E}\left[(Z - \overline{Z})^2\right] = \mathbb{E}\left[(g(\boldsymbol{X}) - g(\overline{\boldsymbol{X}}))^2\right] = \mathbb{E}\left[\left(\sum_{i=1}^{n} \frac{\partial g}{\partial X_i}(X_i - \overline{X_i})\right)^2\right]$$

$$= \sum_{i=1}^{n} \sum_{k=1}^{n} \frac{\partial g}{\partial x_i} \frac{\partial g}{\partial x_k} \mathbb{E}[(X_i - \overline{X_i})(X_k - \overline{X_k})] \tag{3.7}$$

finally the distribution function $F_z(z)$ is approximated by a normal distribution:

$$F_z(Z) = \Phi\left(\frac{z - \overline{Z}}{\sigma_Z}\right) \tag{3.8}$$

then we obtain the approximate result:

$$P_f = F_z(0) = \Phi\left(-\frac{\overline{Z}}{\sigma_Z}\right) \tag{3.9}$$

the reliability R can finally be expressed as:

$$R = \Phi(\beta) \tag{3.10}$$

where $\beta = \frac{\overline{z}}{\sigma_z}$ and the probability of failure consequently becomes expressed as:

$$P_f = 1 - R = 1 - \Phi(\beta) = \Phi(-\beta) \tag{3.11}$$

3.1.2   RBDO

In its basic form the problem of RBDO can be expressed as below:

$$\textit{Minimize } C(\boldsymbol{\theta}) \textit{ s.t. } \left| \begin{array}{l} f_1(\boldsymbol{\theta}), \dots, f_{q-1}(\boldsymbol{\theta}) \leq 0 \\ f_q(\boldsymbol{X}, \boldsymbol{\theta}) = \beta_t - \beta(\boldsymbol{X}, \boldsymbol{\theta}) \leq 0 \end{array} \right. \tag{3.12}$$

where $\boldsymbol{\theta}$ is the vector of the design variables, $C(\boldsymbol{\theta})$ is the cost or objective function, $f_1(\boldsymbol{\theta}),...,f_{q_1}(\boldsymbol{\theta})$ is a vector of $q-1$ deterministic constraints over the design variables $\boldsymbol{\theta}$, $f_q(\boldsymbol{X},\boldsymbol{\theta})$ is the reliability constraint enforcing the respect of LSF and considering the uncertainty to which some of the model parameters $\boldsymbol{X}$ are subjected to. β_t is the target safety index. In this dissertation, to solve Eq. (3.12), the open source software FERUM 4.1 ([Bourinet, 2010]) has been implemented and linked to FE code which evaluates the LSF.

Chapter 4

Optimization of fiber distribution in fiber reinforced composite

4.1 Introduction

The mechanical properties of composites depend on many fiber's variables such as fibers material, volume fraction, size and mesostructure. This latter aspect deals with fiber configuration, orientation, layout and dispersion. As reviewed in Chapter 1, available literatures aimed at the optimization of composite's performance with respect to the above mentioned fiber related variables, have been focused on improving specific performance of a classical laminated or Functionally Graded (FG) composites by changing the fiber's layout (ply orientation) or fiber volume fraction, by using heuristic optimization methods, especially the so-called Genetic Algorithm (GA).

Computational cost is a very important aspect in optimization problem, particularly in industrial applications. Basically, the use of evolutionary algorithms, such as GA, often leads to some limitations; in fact it is well-known as GA is problematic in some issues. Among them, its heuristic nature, high computational cost and sometimes the tendency to converge towards local optima instead of global optima - if proper so-called mutation strategies are not considered in the method - can be counted. In contrary with GA, gradient based methods which use gradient of the objective function evaluated with respect to design variables to find next direction in searching process (tending toward the optimum point), shows lots of merit particularly for complex geometries such as those often used in industrial applications.

There are also some limitations in using FE mapping of the fiber content [Brighenti, 2005] due to the element wise poor representation of the fiber layout: the first one is the possibility of mesh dependency for the results, since the final fibers arrangement resulting from the optimization is commonly determined based on fiber content of each finite element. Secondly, it could be easily understood that in order to have good

layout representation, fine mesh and consequently costly computation should be done; moreover further post processing technique such as filtering or smoothing becomes necessary when this method is implemented. Thirdly, it must be also considered that, before economical and technological evaluations are performed, to fabricate element-wise variation of fiber content in a discretized continuum structure is still a daunting step with present available technologies. Fig. 4.1 schematically shows such limitations involved in FE mapping representation.
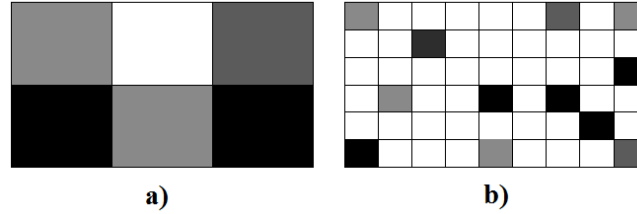
Figure 4.1: Schematic illustration of mesh dependency in element-based representation of fiber volume fraction: a) Coarse mesh b) Fine mesh

Instead of using element-based fiber volume fraction description, as has been already done in other researches, the idea of utilizing quadratic NURBS basis functions in order to smoothly and continuously approximate given set of nodal points are developed. Useful characteristics of NURBS basis functions such as compact support and higher order elements not only provides mesh independent distribution results but also makes it possible to use coarse meshes to decrease computational time, while maintaining the accuracy of the results. The presented novel computational approach combines NURBS based and gradient based optimization methodologies to get an efficient optimization algorithm, which has been verified to be enough accurate, computationally fast and convenient for real industrial applications.

4.2   FRC homogenization methodology

Basically the aim of homogenization techniques is to determine equivalent material characteristics in a Representative Volume Element (RVE) of composite material. There are some classical approaches in order to model the material properties of composites; among which the rule of mixture, Hashin-Shtrikman type bounds [Hashin, 1962 and Hashin & Shtrikman, 1963], Variational Bounding Techniques [Paul, 1960], Self Consistency Method [Hill, 1965] and Mori-Tanaka Method [Mori & Tanaka, 1973] can be mentioned. The homogenization approach used in this chapter is a simplified version of recently developed mechanical model [Brighenti, 2004a], to get the FRC constitutive behavior based on the shear stress distribution along the fiber-matrix interface during the loading process. The adopted model for fiber homogenization can be con-

sidered to be mechanically based, since the fiber contribution to the FRC mechanical properties are determined from the effective stress transfer between matrix and fibers; moreover the possibility of fiber-matrix debonding can be easily taken into account. Since the goal of this research is to focus on fiber distribution through the structure rather than developing micromechanical model, for sake of simplicity this issue is neglected in the present work. Moreover it can be considered that for not too high stressed composite elements (as followed in presented numerical examples) leading to shear fiber-matrix interface stresses well below the allowable limit shear bimaterial stress, the debonding phenomenon can reasonably assumed not to occur as well as fiber breaking. This approach is briefly summarized below; however interested reader can refer to [Brighenti, 2004a], [Brighenti, 2012] and [Brighenti, 2004b] for more details.

The equivalent elastic properties of a fiber reinforced composite material for which the hypotheses of short, homogeneously and randomly dispersed fibers are made can be obtained by equating the virtual work rate of constituents for a RVE (it is assumed that the RVE characteristic length d is much more smaller that the structure characteristic length D) of the composite material (Fig. 4.2) with the equivalent homogenized one

$$
w' = \overbrace{\int_V \kappa(\boldsymbol{x})\dot{\tilde{\boldsymbol{\varepsilon}}} : \boldsymbol{\sigma}\,dV + \int_V \chi(\boldsymbol{x})\dot{\tilde{\varepsilon}}_f \cdot \sigma_f\,dV}^{\text{composite's work rate}}
$$
$$
\underbrace{\phantom{w' = \int_V \kappa(\boldsymbol{x})}}_{\text{homogenized material's work rate}}
$$
$$
= \overbrace{\int_V \dot{\tilde{\boldsymbol{\varepsilon}}} : \boldsymbol{\sigma}_{eq}dV} \tag{4.1}
$$

where $\dot{\tilde{\varepsilon}}_f$; σ_f are the virtual strain rate and the stress in a fiber, respectively, while the scalar functions $\kappa(\boldsymbol{x})$ and $\chi(\boldsymbol{x})$ assume the following meaning:

$$
\kappa(\boldsymbol{x}) = \left\{ \begin{array}{ll} 1 & if\ (\boldsymbol{x}) \in V_m \\ 0 & if\ (\boldsymbol{x}) \notin V_m \end{array} \right. \quad and \quad \chi(\boldsymbol{x}) = \left\{ \begin{array}{ll} 1 & if\ (\boldsymbol{x}) \in V_f \\ 0 & if\ (\boldsymbol{x}) \notin V_f \end{array} \right. \tag{4.2}
$$

allowing to identify the location of the material point $\boldsymbol{x}$ either in the matrix or in the reinforcing phase.

The constitutive relationships of the fibers and of the bulk material can be simply expressed through the following linear relations:

$$
\sigma_f = E_f \cdot (\boldsymbol{i} \otimes \boldsymbol{i}) : \boldsymbol{\varepsilon} \quad and \quad \boldsymbol{\sigma}_{eq}(\boldsymbol{x}) = \boldsymbol{C}_{eq}(\boldsymbol{x}) : \boldsymbol{\varepsilon} \tag{4.3}
$$

in which E_f is the fibers' Young's modulus, ε_f is the fiber strain, $\boldsymbol{C}_{eq}$ is the composite equivalent elastic tensor while $\boldsymbol{\varepsilon}$ is the actual matrix strain tensor. Eq. (4.3) has been written by taking into account that the matrix strain measured in the fiber direction is given by $\varepsilon_f = (\boldsymbol{i} \otimes \boldsymbol{i}) : \boldsymbol{\varepsilon}$ where $\boldsymbol{i} = (\sin\theta\cos\phi \ \sin\theta\sin\phi \ \cos\theta)$ is the unit vector identifying the generic fiber direction, (Fig. 4.2) and analogously for the virtual $\tilde{\varepsilon}_f$ and

the virtual strain rate,

$$\tilde{\varepsilon}_f = (\boldsymbol{i}\otimes\boldsymbol{i}) : \tilde{\boldsymbol{\varepsilon}} \quad and \quad \dot{\tilde{\varepsilon}}_f = (\boldsymbol{i}\otimes\boldsymbol{i}) : \dot{\tilde{\boldsymbol{\varepsilon}}} \tag{4.4}$$

By substituting the above expressions in the virtual work rate equality (Eq. (4.1)) one can finally identify the composite equivalent elastic tensor

$$\begin{aligned}\boldsymbol{C}_{eq}(\boldsymbol{x}) &= \frac{1}{V}\int_V \{\kappa(\boldsymbol{x})\,\boldsymbol{C}_m + \chi(\boldsymbol{x})\,E_f[\boldsymbol{Q}\otimes\boldsymbol{Q}]\}dV \\ &= \mu\boldsymbol{C}_m + \eta_p E_f \int_V \boldsymbol{Q}\otimes\boldsymbol{Q}\,dV\end{aligned} \tag{4.5}$$

where the second-order tensor $\boldsymbol{Q}=(\boldsymbol{i}\otimes\boldsymbol{i})$ has been introduced and the matrix and fiber volume fractions $\mu = \frac{1}{V}\int_V \kappa(\boldsymbol{x})\,dV = \frac{V_m}{V}$ and $\eta_p = \frac{1}{V}\int_V \chi(\boldsymbol{x})\,dV = \frac{V_f}{V}$ have been used. It can be easily deduced as the equivalent material is macroscopically homogeneous at least at the scale of the RVE with volume V - i.e. the equivalent elastic tensor $\boldsymbol{C}_{eq}(\boldsymbol{x})$ does not depend on the position vector, i.e. $\boldsymbol{C}_{eq}(\boldsymbol{x}) = \boldsymbol{C}_{eq}$.

The calculation of the equivalent elastic tensor $\boldsymbol{C}_{eq}$ through Eq. (4.5), requires to evaluate the integral in Eq. (4.5) over a sufficiently large volume, representative of the macroscopic characteristics of the composite. The above integral can be suitably assessed on a hemisphere volume which allows considering all possible fiber orientations in the composite
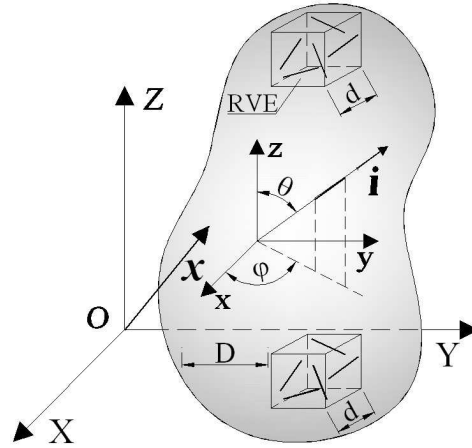
Figure 4.2: Fiber reinforced composite material: definition of the RVE (with a characteristic length d, while the composite has a characteristic length $D>>d$) and of the fiber orientation angles ϕ, θ, Ref. [Brighenti, 2012]

$$\frac{1}{V_{hem}} \int_{V_{hem}} \boldsymbol{Q} \otimes \boldsymbol{Q} dV = \int_0^R \int_0^{2\pi} \int_0^{\pi/2} (\boldsymbol{Q} \otimes \boldsymbol{Q}) r \, d\phi \, r \sin\theta d\theta \, dr$$

$$= \frac{R^3}{3} \frac{1}{\frac{2\pi R^3}{3}} \int_0^{2\pi} \int_0^{\pi/2} (\boldsymbol{Q} \otimes \boldsymbol{Q}) d\phi \sin\theta \, d\theta \qquad (4.6)$$

$$= \frac{1}{2\pi} \int_0^{2\pi} \int_0^{\pi/2} (\boldsymbol{Q} \otimes \boldsymbol{Q}) d\phi \sin\theta \, d\theta$$

In the above expression the case of fibers randomly distributed in the 3D space has been considered, but the generic case of preferentially oriented fibers can be also treated in a similar way [Brighenti & Scorza, 2012].

4.3   Definition of the optimization problem

Lots of structural characteristics or responses can be adopted as optimization objectives. As representative examples one can mention weight, stiffness, natural frequencies or a combination of them. Optimization aimed at obtaining structures with minimum strain energy (minimum structural compliance), which alternatively means maximum structural stiffness, is the most common approach in this field. Nevertheless, though combination of elastic compliance with structural volume or weight constraints is comprehensive for static problems, obtained designs are not essentially optimum considering dynamic behavior of the structure. One important example is represented by vibrating structures to be designed in such a manner to avoid resonance for external excitation loads varying with a given frequency. This goal is usually obtained by maximizing the fundamental eigenfrequency or the gap between two consecutive eigenfrequencies of the structure [Du & Olhoff, 2007].

In the context of this chapter just the optimization of fiber distribution through the structure will be addressed. Definition of single objective function either for pure static loading or free vibration is considered. Extension of this methodology into multi-objective problems, which deals with systematic and concurrent solution of a collection of objective functions, will be straight forward in formulation. Typical multi-objective optimization problem consists of a weighted sum of all objective functions combined to a form of single function. Final solution of this function is totally dependent on the allocated weights. On the other hand from the technological point of view, engineers need to know a specific volume fraction for design and manufacturing of a FRC product. Generally there is no single global solution for multi-objective optimization problems and selection of a set of points as a final solution among thousands of possible solutions requires to develop a comprehensive selection criteria which is behind the scope of this chapter. To review the multi-objective optimization methods in engineering, interested readers can refer to [Marler & Arora, 2004].

4.3.1 Objective function and optimization formulation for static problems

Strain energy can be considered as the work done by internal forces through the deformation of the body. This energy is considered as the objective function of the optimization problem. For the problem with m-load cases we have

$$U = \sum_{i=1}^{m} \lambda_i U^i \quad \lambda_i > 0 \tag{4.7}$$

where U and U^i are the total strain energy and elastic strain energy for the ith load case respectively; while λ_i is the weight associated to the strain energy which has been considered equal to unity unless otherwise specified.
The terms U^i can be defined as

$$U^i = [\sum_{e=1}^{nel} \frac{1}{2} \int_V \boldsymbol{\varepsilon}_e^T \boldsymbol{C}_{eq} \, \boldsymbol{\varepsilon}_e dV]^i \tag{4.8}$$

in the above equation $\boldsymbol{\varepsilon}_e$ is the strain vector associated with element e and $\boldsymbol{C}_{eq}$ is the homogenized elastic tensor of the composite at each point according to Eq. (4.5), while nel is the number of elements in the structural component being analyzed.

Nodal fiber volume fraction $\varphi_{i,j}$ (the subscripts i and j belong to counterpart control point, $B_{i,j}$) on control points are defined as design variables and fiber distribution is approximated by using NURBS surface (see Eq. (2.10) and Fig. 2.1(c)) based on formulation provided in Chapter 2. Every point on parametric mesh space of the design domain will be mapped to geometrical space having two distinguished identifications, i.e. geometrical coordinates and fiber volume fraction value. Intrinsically, even using coarse meshes, distribution function described through a NURBS surface is smooth enough to have clear representation with no need to any further image processing technique.

Fiber distribution function $\eta_p(x,y)$- which indicates the fiber amount at every design point and will be used for obtaining homogenized mass and stiffness of finite elements- is defined according to the following relationship

$$\eta_p(x,y) = \sum_{i=1}^{n} \sum_{j=1}^{m} R_{i,j}^{p,q} (\xi, \eta) \, \varphi_{i,j} \tag{4.9}$$

Once the fiber volume fraction at each point is available, by substitution in Eq. (4.5), we can define the equivalent mechanical characteristics of the domain through the following equations

$$\boldsymbol{C}_{eq}(x,y) = (1 - \eta_p) \boldsymbol{C}_m + \eta_p E_f \int_V \boldsymbol{Q} \otimes \boldsymbol{Q} \, dV \tag{4.10}$$

$$\rho(x,y) = \left(1 - \eta_p\right)\rho_m + \eta_p\rho_f \tag{4.11}$$

where $\rho(x)$ is the equivalent density at every point in the design domain, obtained by using the rule of mixtures. ρ_m and ρ_f are matrix material and fiber material density, respectively. The optimization problem can be finally summarized as follows

$$\begin{cases} Minimize : U \\ s.t. \\ w_f = \int_V \eta_p\rho_f \, dV = w_{f0} \\ \boldsymbol{Ku = f} \\ \varphi_{i,j} - 1 \leq 0 \\ -\varphi_{i,j} \leq 0 \end{cases} \tag{4.12}$$

where w_f is the total fiber weight in every optimization iteration and w_{f0} is an arbitrary initial fiber weight which must be set at the beginning of the optimization process. $\boldsymbol{K}$, $\boldsymbol{u}$ and $\boldsymbol{f}$ in Eq. (4.12) (which represent the general system of equilibrium equations in linear elastic finite elements method) are the global stiffness matrix of the system, the displacement and the force vector, respectively.

By introducing a proper Lagrangian objective function, l, and by using the Lagrangian multipliers method we have

$$l = U - \lambda \left(w_f - w_{f0}\right) - \sum_{i,j=1}^{ncp} \psi_1 \left(\varphi_{i,j} - 1\right) - \sum_{i,j=1}^{ncp} \psi_2 \left(-\varphi_{i,j}\right) \tag{4.13}$$

where λ, ψ_1 and ψ_2 are volume, upper and lower bounds Lagrange multipliers while ncp is the number of control points. By setting the first derivative of Eq. (4.13) to zero we will obtain

$$\frac{\partial l}{\partial \varphi_{i,j}} = \frac{\partial U}{\partial \varphi_{i,j}} - \lambda \frac{\partial w_f}{\partial \varphi_{i,j}} - \psi_1 + \psi_2 = 0 \tag{4.14}$$

Eq. (4.14) can be solved numerically by using different approaches such as the so-called method of moving asymptotes (MMA) algorithm [Svanberg, 1987]. In this work optimality criteria (OC) based optimization [Zhou & Rozvany, 1991] has been implemented unless otherwise specified. OC represents a simple tool to be implement and allows a computationally efficient solution because updating of each design variables takes place independently. The updating scheme of OC is based on sensitivity analysis which is performed in Section 4.3.3.

4.3.2 Objective function and optimization formulation for free vibration problems

Maximization of fundamental eigenvalue, which is herein considered as objective function for free vibration problems, can be formulated as follows

$$
\begin{cases}
Maximize : \omega_{min} \\
s.t : \\
w_f = \int_V \eta_p \rho_f \, dV = w_{f0} \\
(\boldsymbol{K} - \omega_i \boldsymbol{M}) \boldsymbol{\phi}_i = \boldsymbol{0} \quad i = 1, \ldots, no. \ of \ DOF \\
\varphi_{i,j} - 1 \leq 0 \\
-\varphi_{i,j} \leq 0
\end{cases}
\tag{4.15}
$$

where ω_i stands for the ith eigenvalue, ω_{min} is the fundamental frequency of the structure, $\boldsymbol{M}$ is the system mass matrix and ϕ_i is the eigenvector associated with the ith eigenfrequency. The second constraint in Eq. (4.15) represents the standard elastodynamic formulation for free vibration problems without damping.

4.3.3 Sensitivity analysis

Basically, in order to update design variables toward the optimized solution, OC needs to determine how different values of the independent variable (i.e. $\varphi_{i,j}$) influence the objective function under a given set of design constraints. One method to do this is to consider the partial derivative of the objective function and constraints with respect to design variables.

In Eq. (4.14) we can calculate $\frac{\partial U}{\partial \varphi_{i,j}}$ and $\frac{\partial w_f}{\partial \varphi_{i,j}}$ through the following expressions

$$
\frac{\partial U}{\partial \varphi_{i,j}} = \sum_{i=1}^{m} \lambda_i \frac{\partial U^i}{\partial \varphi_{i,j}}
\tag{4.16}
$$

where

$$
\frac{\partial U^i}{\partial \varphi_{i,j}} = \frac{1}{2} \int_V \boldsymbol{\varepsilon}^T \frac{\partial \boldsymbol{C}_{eq}}{\partial \varphi_{i,j}} \boldsymbol{\varepsilon} \, dV
\tag{4.17}
$$

while

$$
\frac{\partial \boldsymbol{C}_{eq}}{\partial \varphi_{i,j}} = - \frac{\partial \eta_p}{\partial \varphi_{i,j}} \boldsymbol{C}_m + \frac{\partial \eta_p}{\partial \varphi_{i,j}} E_f \int_V \boldsymbol{Q} \otimes \boldsymbol{Q} \, dV
\tag{4.18}
$$

and

$$
\frac{\partial \eta_p}{\partial \varphi_{i,j}} = R_{i,j}^{p,q} (\xi, \eta)
\tag{4.19}
$$

24

It should be declared that in order to calculate Eq. (4.18), the value $\frac{\partial C_m}{\partial \varphi_{i,j}} = 0$ has been considered since the Poisson's ratios for both fiber and matrix are assumed to be the same. On the other hand $\frac{\partial w_f}{\partial \varphi_{i,j}}$ can be also calculated as follows

$$\frac{\partial w_f}{\partial \varphi_{i,j}} = \int_V \frac{\partial \eta_p}{\partial \varphi_{i,j}} \rho_f \, dV \tag{4.20}$$

For the problem of free vibration, we follow the same procedure in order to perform sensitivity analysis; so we calculate partial derivatives of each term of the second constraint in Eq. (4.15) with respect to $\varphi_{i,j}$

$$\left(\frac{\partial K}{\partial \varphi_{i,j}} - \frac{\partial \varpi_i}{\partial \varphi_{i,j}} M - \varpi_i \frac{\partial M}{\partial \varphi_{i,j}} \right) \phi_i = 0 \tag{4.21}$$

by rewriting Eq. (4.21) and normalizing eigenvector with respect to the kinetic energy (i.e. $\phi_i^T M \phi_i$), we will finally have

$$\frac{\partial \varpi_i}{\partial \varphi_{i,j}} = \phi_i^T \left(\frac{\partial K}{\partial \varphi_{i,j}} - \varpi_i \frac{\partial M}{\partial \varphi_{i,j}} \right) \phi_i \tag{4.22}$$

where

$$\frac{\partial K}{\partial \varphi_{i,j}} = \int_V B^T \frac{\partial C_{eq}}{\partial \varphi_{i,j}} B \, dV \tag{4.23}$$

where B is the standard finite element compatibility matrix containing the derivatives of the shape functions while $\frac{\partial C_{eq}}{\partial \varphi_{i,j}}$ can be obtained through Eq. (4.18). Derivative of consistent mass matrix with respect to design variables can be calculated as follows

$$\frac{\partial M}{\partial \varphi_{i,j}} = \int_V N^T \frac{\partial \rho}{\partial \varphi_{i,j}} N dV \tag{4.24}$$

while

$$\frac{\partial \rho}{\partial \varphi_{i,j}} = - \frac{\partial \eta_p}{\partial \varphi_{i,j}} \rho_m + \frac{\partial \eta_p}{\partial \varphi_{i,j}} \rho_f \tag{4.25}$$

in Eq. (4.24) N is the matrix of shape functions while $\frac{\partial \eta_p}{\partial \varphi_{i,j}}$ can be calculated by Eq. (4.19).

4.3.4 Optimization procedure

In the present optimization procedure, after definition of the optimization problem according to Section 4.3.1 and 4.3.2, once discretized the structural element domain

through finite elements, the obtained discrete model is analyzed based on the considered design parameters (i.e. geometry, loading, boundary conditions, material constraints, etc.), starting from the initial value of the design variable (i.e. available fiber volume fraction). Afterwards the optimizer does sensitivity analysis (as explained in Section 4.3.3) and then OC updates design variables. This computational procedure is performed iteratively till no sensible changes (limit can be set as a design parameter) occur in design variables. Fig. 4.3 summarizes this procedure.
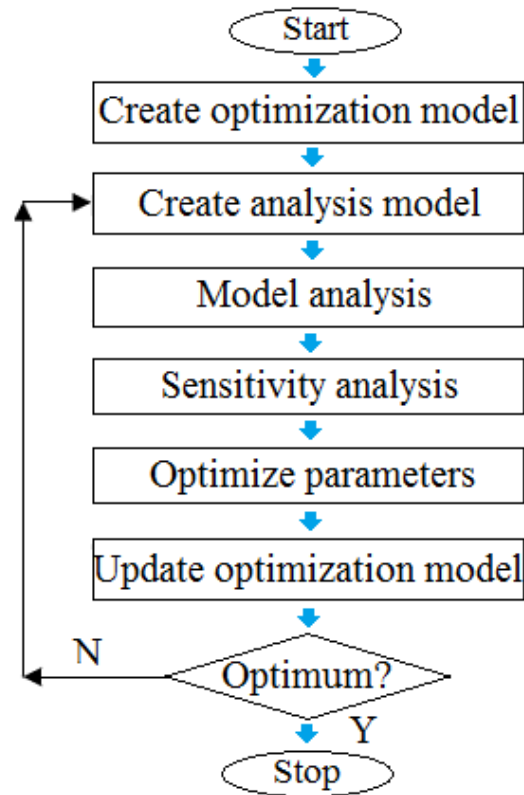
Figure 4.3: Optimization algorithm

4.4   Case studies

In this section the applicability of the model has been investigated by conducting some numerical examples in order to demonstrate the advantages of the proposed optimization model.

In the present algorithm the minimum and the maximum values of fiber content in each design point can be set by designer before optimization process commencement. For the case of random distribution of fiber in the matrix, the maximum fiber content

practically can range between 30% and 60%. The minimum value of the fiber content has been also considered 0.1% through this chapter unless otherwise specified.

4.4.1 Three-point bending of a wall beam

The first example involves a three point bending problem of a plane stress wall beam. Schematic view and design parameters are as shown in Fig. 4.4 and Table 4.1, respectively. A constant total fiber volume fraction equal to 10% is considered and the optimization problem for obtaining the minimum structural compliance is solved. Fig. 4.5(a) shows result of fiber distribution optimization in half of the wall beam. Regions with white color stand for minimum fiber content (which is set equal to 0.1%), while black regions depict maximum fiber content and gray regions have the value between minimum and maximum.
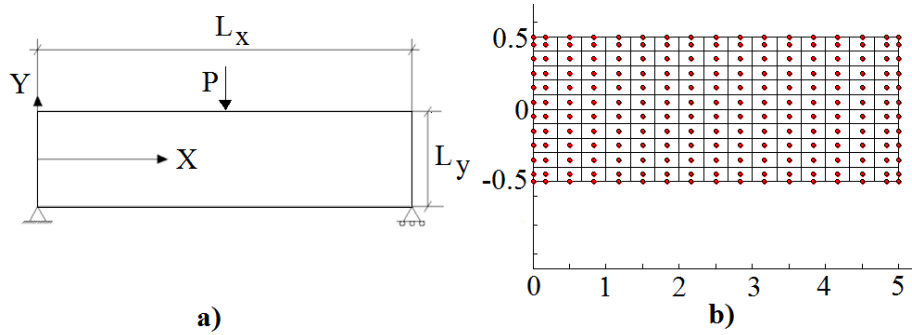
Figure 4.4: Geometry (a) and FE mesh with control points indicated by dots (b) of a three-point bending wall beam

Table 4.1: Problem definitions, wall beam under three-point bending

L_x	L_y	E_m	E_f	v	ρ_m	ρ_f	P	V_f	V_{fmax}	ncp
5	1	20	200	0.1	1000	1450	1000	10%	60% and 30%	$22 \times 12 = 264$

$Length : m, E : GPa, P : Applied\ load\ (N), v : Poisson's\ ratio, \rho : density \left(\frac{kg}{m^3}\right) m : matrix, f : fiber, V_f :$
$fiber\ volume\ fraction, V_{fmax} : max.\ fiber\ vol.\ frac.$

Fig. 4.5(b) shows the benchmark result as presented in [Brighenti, 2005]. Using the same number of elements for both Fig. 4.5(a) and Fig. 4.5(b), although there are some local differences which can be mainly referred to the heuristic nature of GA and element based demonstration of results used in [Brighenti, 2005], one can figure out the general conformity between two categories of results since in both results, fibers are more concentrated on regions under the loaded point, regions with maximum displacements and around supports. Readers should also notice that this comparison is just for general verification of the presented method not for detail adaptation. This is due to the fact that both categories of results are slightly dependent on variables
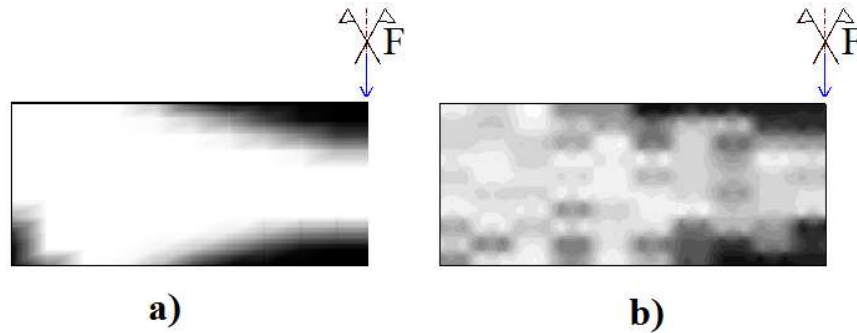
Figure 4.5: Optimized fiber distribution through left half of the beam (a) current methodology and (b) Ref. [Brighenti, 2005]

setting (initial populations, probability of cross over, probability of mutation for results of [Brighenti, 2005] and maximum fiber volume fraction, end point of optimization algorithm, solution tolerance for the present work).

Fig. 4.6(a) shows the obtained results for the case that maximum fiber content in each design point is allowed to be increase up to 60%, while for the case Fig. 4.6(b) this value is assumed to be equal to 30%. Results provided by subsequent optimization iterations are shown from top to bottom; as expected, by decreasing the upper limit of local fiber content, the obtained fiber layout occupies more area of admissible design domain while total used fibers is the same for (a) and (b). Having assumed a constant total fiber volume fraction and considering different admissible values for maximum fiber content in each element, normalized elastic compliance (using 264 control points) versus the number of iterations are accordingly plotted in Fig. 4.7. High rate and smooth convergence can be appreciated; these desirable computational characteristics have been obtained thanks to both implemented methodologies (particularly optimization based on sensitivity analysis instead of heuristic method) and NURBS finite elements. It is also noteworthy to point out that, by increasing maximum admissible fiber volume in each element, lower compliance will be obtained. This simply can be explained by considering that, increasing maximum admissible fiber volume will cause fibers to gather up more and more in the most appropriate design points having the highest influence on increasing the structural stiffness, not in somewhere around the best points.

Readers should distinguish between the so called "fiber gathering up" and "fiber agglomeration". The former, which stands for increase in fiber volume fraction, happens in structural design domain (i.e. at the macro scale) but the latter, basically is addressed in RVE scale. Moreover in contrary with agglomeration which reduces the structural stiffness (in comparison with uniformly distributed fibers), optimum fiber distribution always yields to an increase in structural stiffness.
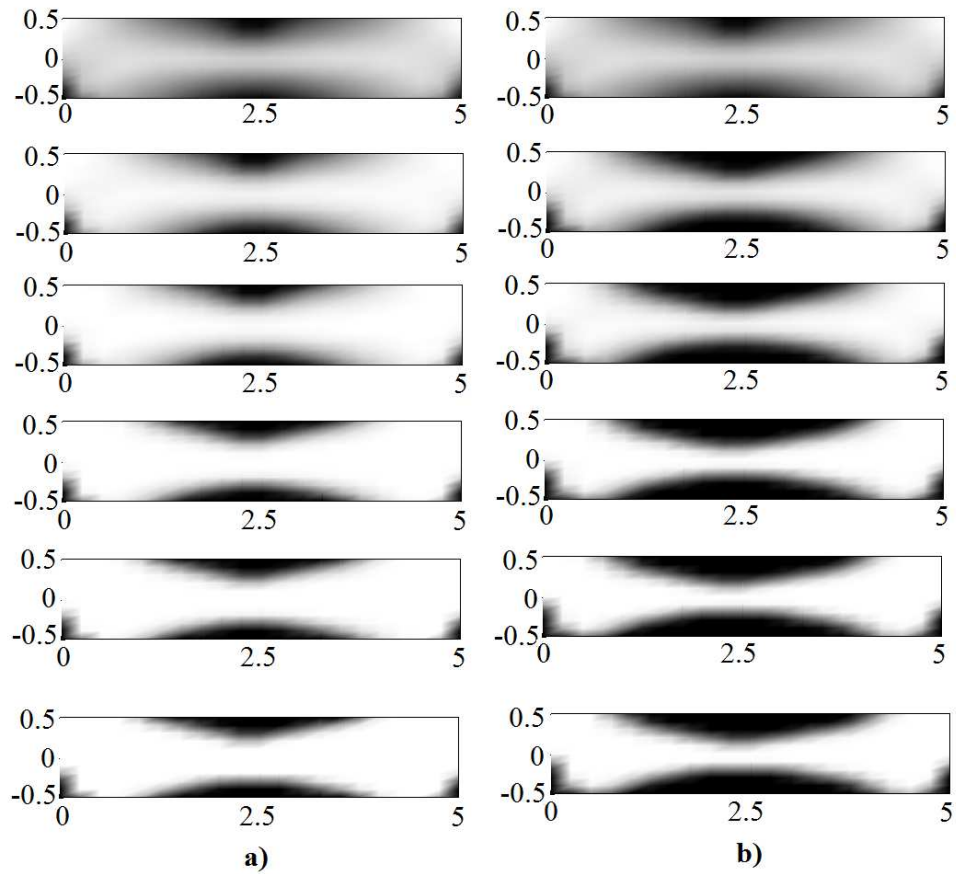
Figure 4.6: Optimum fiber distribution in beam considering a constant total fiber volume equal to 10%; the maximum local fiber content is assumed equal to (a) 60% and (b) 30%; iterations results are displayed from top to bottom for each case
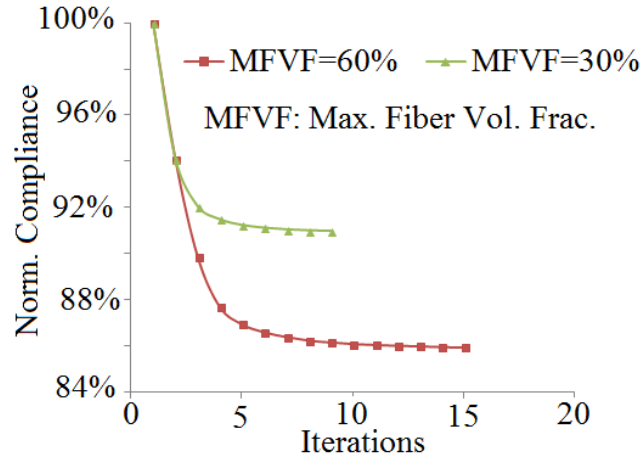
Figure 4.7: Normalized compliance versus number of iterations for different values of maximum fiber content in each element, using 264 control points

4.4.2 Free vibration of a beam

In the second example free vibration of a FRC beam under different support conditions has been considered. As indicated in Fig. 4.8 a cantilever beam (Fig. 4.8(a)) and a clamped beam (Fig. 4.8(b)) have been assumed. Design parameters are according to Table 4.2 and FE discretization is the same as in the previous example.
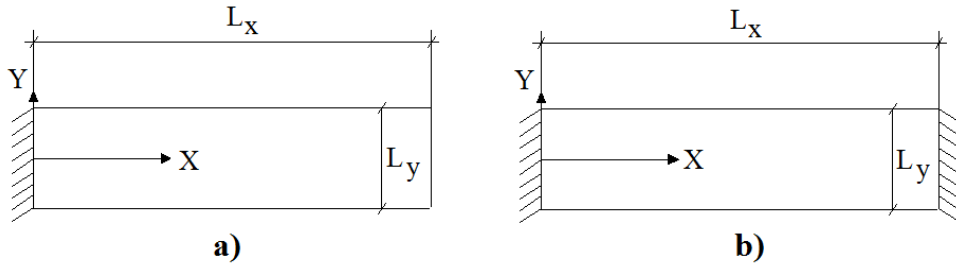
Figure 4.8: Schematic view of problem geometry, (a) cantilever beam (b) clamped beam

Table 4.2: Problem definitions, free vibration of a beam.

L_x	L_y	E_m	E_f	ν	ρ_m	ρ_f	V_f	V_{fmax}	ncp
8	1	20	200	0.1	1000	1450	10%	60%	$22 \times 12 = 264$

Length : m, E : GPa, ν : Poisson's ratio, ρ : density $\left(\frac{kg}{m^3}\right)$, m : matrix, f : fiber, V_f : fiber volume fraction, V_{fmax} : max. fiber vol. frac.

In this problem the adopted objective function aims to get the maximum value of the fundamental frequency by optimizing fiber distribution through the beam domain.

First modal shape as well as fiber distribution optimization results for both cantilever and clamped beams are demonstrated in Fig. 4.9(a-b), respectively. Fig. 4.10 shows the

a)   b)
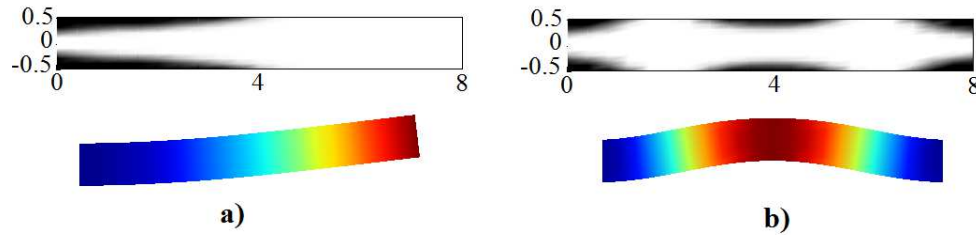
Figure 4.9: First modal shapes and optimum fiber distribution for a cantilever beam (a) and a clamped beam (b)

patterns of the objective function (fundamental frequency of the beam normalized with respect to the case of uniformly reinforced material) versus the optimization iterations. It can be observed as the increasing in fundamental frequencies are around 11% for cantilever and 7% for clamped beams.
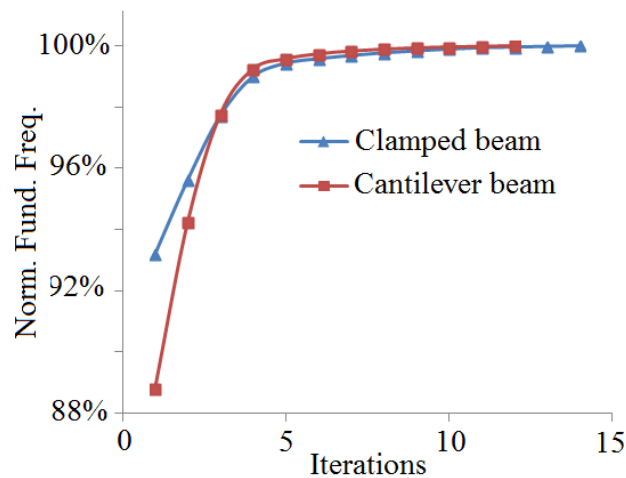
Figure 4.10: Normalized fundamental frequency versus iterations for beam with different supporting conditions

4.4.3 Square plate with a central circular hole under tension

As the third example, a square plate with central hole under constant distributed edge load was studied. Due to the double symmetry only one quarter of this plate is modeled. Fig. 4.11(a-b) and Table 4.3 show analysis model, the FE domain discretization and the design parameters, respectively. The problem of obtaining minimum elastic compliance (objective function) is solved by using quadratic NURBS meshes.

Table 4.3: Problem definitions, plate with a central circular hole under tension

L	R	E_m	E_f	ν	ρ_m	ρ_f	P	V_{fmax}	ncp
4	1	20	200	0.1	1000	1450	510	60%	$180, 612, 2244$

$Length: m, \; E: GPa, \; P: Load\,(N/m), \; \nu: Poisson's\;ratio, \; \rho: density\left(\frac{kg}{m^3}\right), \; m: matrix, \; f: fiber, \; V_{fmax}:$
$max.\;fiber\;vol.\;frac.$
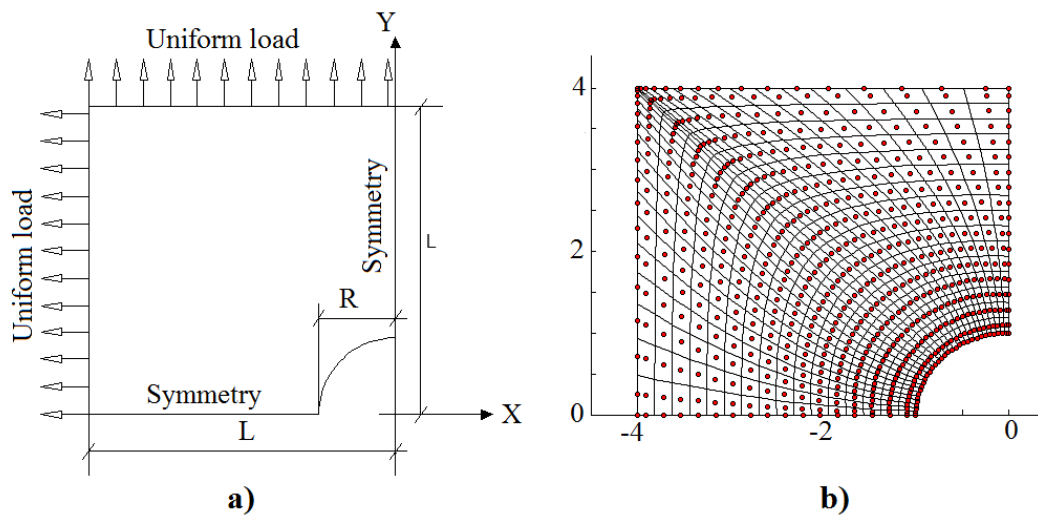
Figure 4.11: (a) Schematic view of the model under uniform edges load P and (b) mesh with control points (dots)

Fig. 4.12 presents optimum fiber distribution through the structure. Results represented in Fig. 4.12(a-c) correspond to meshes with 180, 612 and 2244 control points, respectively; as can be observed, smooth solution can be also obtained not necessarily by implementing fine meshes.
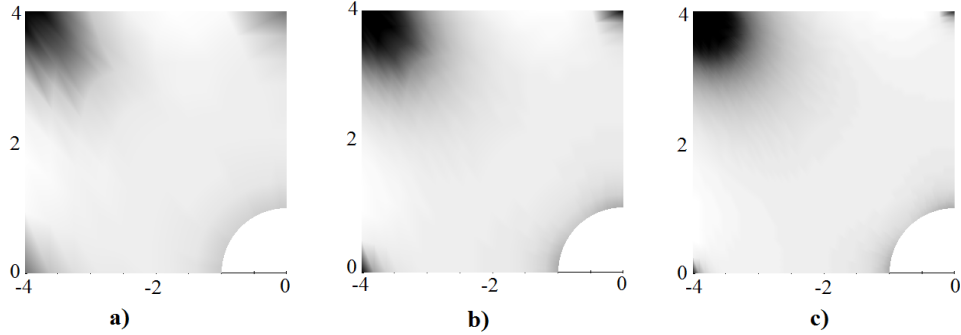
Figure 4.12: Optimum fiber distribution using (a) 180 control points, (b) 612 control points and (c) 2244 control points

Histories of objective function (normalized elastic compliance) versus the iteration steps for different mesh sizes are plotted in Fig. 4.13; it can be noted as the deviation between results less than 2% can be obtained by using coarse meshes with respect to the finer one, while computational cost is obviously lower by using rough discretization. On the other words, the use of coarse NURBS mesh maintains precision of the results while decreasing the computational time.

4.5   Concluding remarks

The efficient gradient based optimization of fiber distribution in fiber reinforced continuum elements, has been developed in the present chapter through the use of NURBS functions. The adopted computational technique has been implemented and used for both domain discretization and definition of fiber distribution function. The proposed approach allows to get a high rate and smooth convergence to the optimum condition sought while results are also mesh independent. The method allows considering generic objective functions. In particular here the minimization of elastic strain energy and maximization of fundamental frequency for static and free vibration problems have been considered respectively; by varying the fibers distribution characteristics in the body under study. Nodal volume fraction of fiber has been used as the optimization design variable, whose distribution function has been smoothly approximated by using a NURBS surface. The mechanical behavior of the composite has been macroscopically described through a homogenization approach that considers a random orientation of fibers in the matrix. Some representative numerical examples have finally been
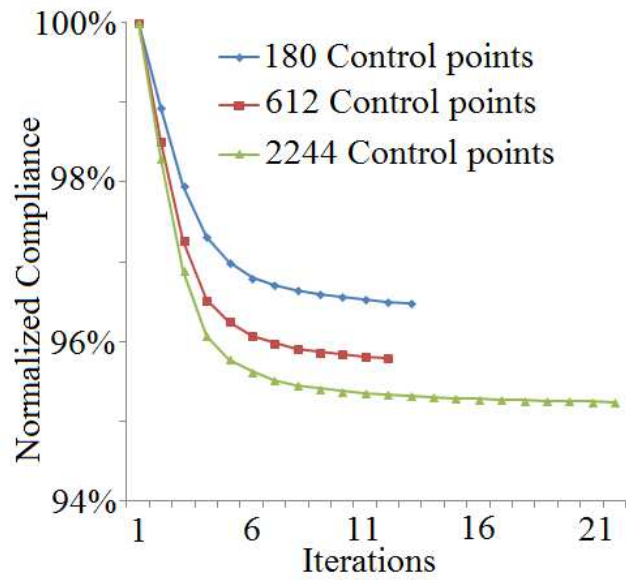
Figure 4.13: Normalized compliance versus number of iterations for different mesh sizes

presented; both optimization related to the structural response under static loading and the free vibration behavior of composite structural elements, have been considered in order to demonstrate that combining NURBS approximation and sensitivity based optimization method yields to high convergence rate and mesh independent optimization results.

Chapter 5

Uncertainties propagation in optimization of CNT/polymer composite

5.1 Introduction

Carbon Nano Tube (CNT) in polymer matrix which is called CNT/polymer composites have received attention thanks to their enhanced mechanical, electrical and thermal properties [Lau *et al.*, 2006]. Different approaches have been used in order to characterize Polymeric Nano Composites (PNCs): atomistic modeling, continuum modeling (which can be also subdivided into analytical and numerical approaches) and multi-scale methods [Shokrieh & Rafiee, 2010c]. Molecular dynamics (MD) simulations restrict the model to one CNT in a polymer matrix with very short length. Pure continuum modeling approaches which usually deal with evaluating the composite response in the scale of a Representative Volume Element (RVE), do not account for phenomena taking place on finer scales. Therefore, multi-scale methods were employed coupling MD methods and continuum methods. An overview of multi-scale methods for PNCs has been presented in [Shokrieh & Rafiee, 2012].

The characteristics of a Carbon Nano Tube Reinforced Polymer (CNTRP) material are influenced by many uncertainties. These uncertainties include material properties, the geometry, loading and boundary conditions and the model uncertainties. Hence, probabilistic approaches are needed to determine the reliability of the behavior of nanocomposite structures.

In this chapter, uncertainties are classified in three major groups: material uncertainties, structural uncertainties and modeling uncertainties (Fig. 5.1). Material uncertainties include the molecular interactions and the CNT diameter at nano-scale, the CNT length and CNT-resin interaction at micro-scale, the CNT content, agglomera-

tion, curvature, orientation at meso-scale and the CNT dispersion at macro-scale. Each component e.g. the resin can also experience uncertainties in its material properties (such as Young's modulus and Poisson's ratio). Structural uncertainties lie for instance in the geometry, boundary and loading conditions while typical model uncertainties concern the mathematical model, the discretization and approximation errors. These uncertainties will propagate over different length scales affecting the overall reliability of the structural component.

Uncertainty propagation in nanocomposite structures remains an unsolved issue. Rouhi & Rais-Rohani, 2013 measured the failure probability of a nanocomposite cylinder under buckling, accounting for uncertain design conditions. However, they used micromechanical equations at the nano-scale by simply replacing the lattice structure of a CNT with a solid fiber (which can lead to inappropriate results [Shokrieh & Rafiee, 2010c]). Moreover, they disregard several important CNT parameters such as the CNT length, diameter, agglomeration and dispersion without any sensitivity evaluation. Furthermore, modeling errors including discretization- and approximation errors have not been addressed in detail. In this chapter firstly the most feasible uncertain design parameters and variables in the model are considered in order to get a more realistic insight towards uncertainties and their effects on the final nanocomposite product design. Secondly, the design optimization of nanocomposite components are extended from a pure geometry oriented approach to a material oriented approach and a hybrid approach accounting for the simultaneous optimization of the geometry and material.

For a specific load, the optimal structural results obviously will be obtained for idealistic straight, aligned and not aggregated CNTs. Perfect manipulation of these parameters with current technologies seems to be impractical. On the other hand, the behavior of CNTRP can be changed more efficiently by varying the content of the CNT rather than changing other parameters. To the author's best knowledge, this is the first approach optimizing the CNT content in generic nanocomposite solids considering nearly all CNT parameters. It will answer the question how much CNTs should be added to a resin for an optimal and reliable response of the structural component.

5.2 Stochastic multi-scale CNT/polymer material model

The stochastic multi-scale model has been adopted from [Shokrieh & Rafiee, 2010d ; Shokrieh & Rafiee, 2010b and Shokrieh & Rafiee, 2010a]. Fig. 5.2 illustrates the bottom-up approach including bridging the nano-scale up to the macro-scale (N3M). The CNT is modeled by a quasi-continuum method using beam elements at the nano-scale. Therefore, the strain energy of the beam elements is equated to the interatomic potential energy of Carbon-Carbon (C-C) bonds accounting for the 3-D frame structure of the molecular lattice. Using beam elements instead of spring or truss elements reduces the number of elements in the FE model and consequently reduces the computa-

Figure 5.1: Uncertainties sources and their propagation over different length scales and sources

tional cost (to find reasons reader can refer to [Shokrieh & Rafiee, 2010d]). Neglecting
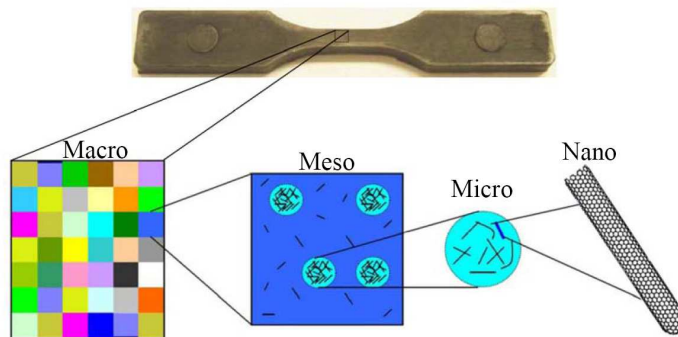
Figure 5.2: Involved scales in simulation of CNTRP [Shokrieh & Rafiee, 2010d]

electrostatic interactions between the CNTs and the surrounding matrix, the interphase region is modeled by non-bonded van der Waals (vdW) interactions. The polymer matrix of the PNC is based on a continuum model at the micro-scale as shown in Fig. 5.3. The interphase behavior is modeled by the adaptive vdW Interaction (AVI) based on 3D truss elements. The material behavior of the micromodel is up-scaled by developing the concept of equivalent fibers accounting for different CNT length and the complex interphase behavior [Shokrieh & Rafiee, 2010b].

(a) Cut section of RVE   (b) Side view of RVE with short CNT
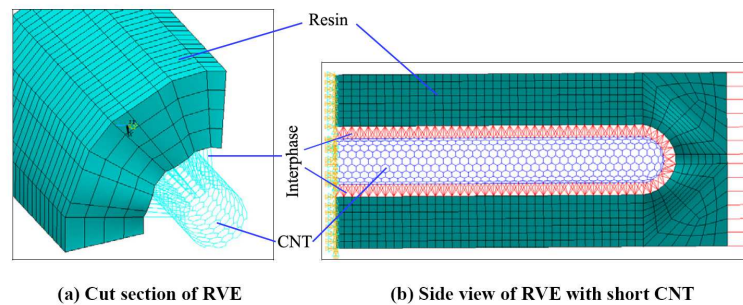
Figure 5.3: Concurrent multi-scale FE model of RVEs as micro-scale [Shokrieh & Rafiee, 2010d]

Randomly distributed and orientated embedded equivalent fibers at meso-scale can experience straight and wavy forms. They can be also concentrated in local aggregates or dispersed in some other areas. A schematic view of RVE at meso-scale is shown in Fig. 5.4. Using equivalent fiber technique, micromechanics theories can be used at proper scale of meso instead of nano. So, implementing improved micromechanics model by Shi *et al.*, 2004, based on Mori & Tanaka, 1973, the Young's modulus and Poisson's ratio of the block of Fig. 5.4 can be obtained. The effect of the CNT waviness (the state of non straight shape of CNT) is also captured by considering upper and lower

bounds of longitudinal and transverse stiffness. More details about waviness modeling are presented in Section 5.5.1.
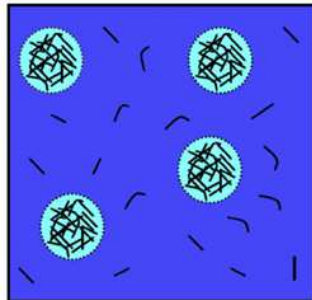
Figure 5.4: RVE of composite at meso-scale [Shokrieh & Rafiee, 2010d]

A Voigt model has been used to determine the overall properties of the material region at the macro-scale. Monte Carlo Simulations (500 realization on an 80×80 material region mesh), for the N3M multi-scale model account for the stochastic uncertainties in CNTRP. The N3M algorithm is summarized in Fig. 5.5.

5.3 Metamodeling

5.3.1 Concept and application

In simulation based optimization, implicit forms of objective functions and constraints dealing with either gradient based or gradient free optimization techniques are computationally expensive, particularly with increasing number of variables and function evaluations. In order to improve the computational efficiency in such design problems, the concept of "metamodel" approximating the physical model has been introduced. The metamodel is constructed based on a sufficient number of sampling points, typically determined through experiments. Selecting a Design Of Experiment (DOE) method for data generation, choosing a model to represent the data, fitting the model and finally model validation are the four basic steps in metamodeling [Park & Dang, 2010]. In this work, the kriging method [Lophaven *et al.*, 2002] has been utilized to approximate the multi-scale material model.

5.3.2 Kriging method

In the kriging method, the unknown value of a response for an input sample point should be the weighted average of the known values of the responses at its neighbors.
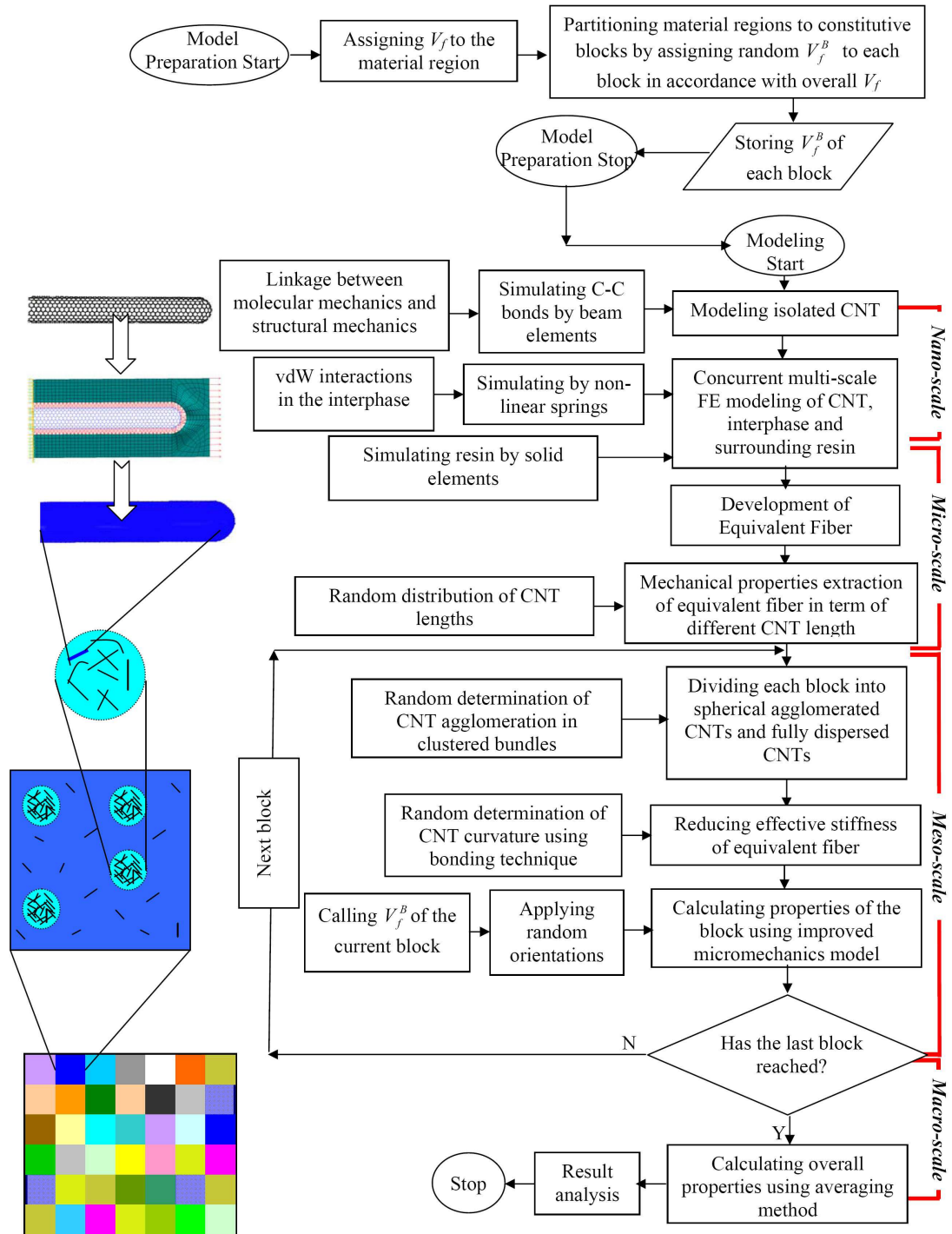
Figure 5.5: Flowchart of developed full stochastic N3M multi-scale material model [Shokrieh & Rafiee, 2010d]

The basic form of the kriging estimator is

$$Z^*\left(\boldsymbol{u}\right) - m\left(\boldsymbol{u}\right) = \sum_{\alpha=1}^{n(u)} \lambda_\alpha[\boldsymbol{Z}\left(\boldsymbol{u}_\alpha\right) - \boldsymbol{m}(\boldsymbol{u}_\alpha)] \qquad (5.1)$$

where $Z(\boldsymbol{u})$ is the random field with a trend component $m(\boldsymbol{u})$ and a residual component $R(\boldsymbol{u}) = Z(\boldsymbol{u}) - m(\boldsymbol{u})$; $\boldsymbol{u}$ being the location vector for an estimation point; $n(\boldsymbol{u})$, $m(\boldsymbol{u})$ and $\lambda_\alpha(\boldsymbol{u})$ are the number of data points in the local neighborhood of the estimated point, the expected (mean) value of $Z(\boldsymbol{u})$ and the assigned kriging weights, respectively. The superimposed * also indicates estimated value. The goal is to determine the weights, λ_α, that minimize the variance of the estimator

$$\sigma_E^2\left(\boldsymbol{u}\right) = Var\left\{\boldsymbol{Z}^*\left(\boldsymbol{u}\right) - \boldsymbol{Z}\left(\boldsymbol{u}\right)\right\} = \boldsymbol{0} \qquad (5.2)$$

under the unbiased constraint $\mathbb{E}\left(Z^*(\boldsymbol{u}) - Z(\boldsymbol{u})\right) = 0$, where $\mathbb{E}(.)$ is the expected value or ensemble average. A computer implementation of the kriging [Lophaven *et al.*, 2002] method has been used to find the unknown weights, λ_α. Fig. 5.6(a) compares actual and estimated values of CNTRP stiffness obtained by N3M and metamodel, respectively. Fig. 5.6(b) shows mean squared error for each predicted point. It can be observed that N3M model can be substituted by kriging metamodel with high level of accuracy and very cheap computational cost.
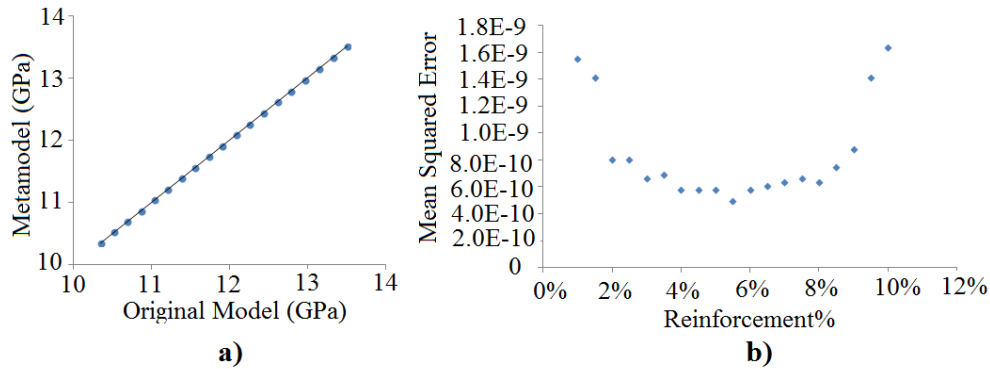
Figure 5.6: Verification of the metamodel (a) mean squared error of each predicted point (b)

5.4 RBDO and metamodel based RBDO

Uncertainties influencing the material and structural response of nanocomposites call for optimization models which can capture the effects of random variables and yield

to reliable designs with higher level of confidence. In contrary to Deterministic Design Optimization (DDO), in RBDO, design parameters are random variables and the optimization objective function is subjected to probabilistic constraints.

Fig. 5.7 schematically compares RBDO and DDO. In DDO almost 75% of the designs around the deterministic optimum fail while RBDO finds the optimal design allowing a specific risk and target reliability level by accounting for the stochastic nature of the random parameters.
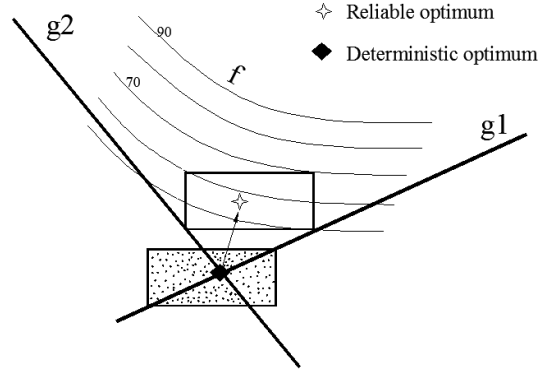
Figure 5.7: Schematic comparisons between RBDO and DDO, f stands for objective function while g_1 and g_2 represent design constraints

In this research a kriging based metamodel has been utilized in each RBDO iteration. In other words, instead of carrying out the RBDO process with the original multi-scale material model, the approximation based RBDO is conducted with the metamodel. If the function expressing the true nature of the computer analysis result is $y = f(x)$, the metamodel of the computer analysis is $\widehat{y} = \widehat{f}(x)$, and hence $y = \widehat{y} + \varepsilon$, where ε is the error of the approximation. So, the metamodel based RBDO becomes

$$\textit{Minimize } \hat{C}(\boldsymbol{\theta}) \textit{ s.t. } \left| \begin{array}{l} \hat{f}_1(\boldsymbol{\theta}),\ldots,\hat{f}_{q-1}(\boldsymbol{\theta}) \leq 0 \\ \hat{f}_q(\boldsymbol{X},\boldsymbol{\theta}) = \beta_t - \beta(\boldsymbol{X},\boldsymbol{\theta}) \leq 0 \end{array} \right. \tag{5.3}$$

Eq. (5.3) has been solved by the open source software FERUM v4.1 [Bourinet, 2010] and linked to the FE code which evaluates the LSF numerically. This software involves a nested, double loop solution procedure where the outer optimization loop includes inner loops of the reliability analysis. In each reliability analysis, the reliability index approach is used as a separate optimization procedure in the standard normal space to search for the most probable point for each active probabilistic constraint. Fig. 5.8 illustrates the nested algorithm of the RBDO procedure.
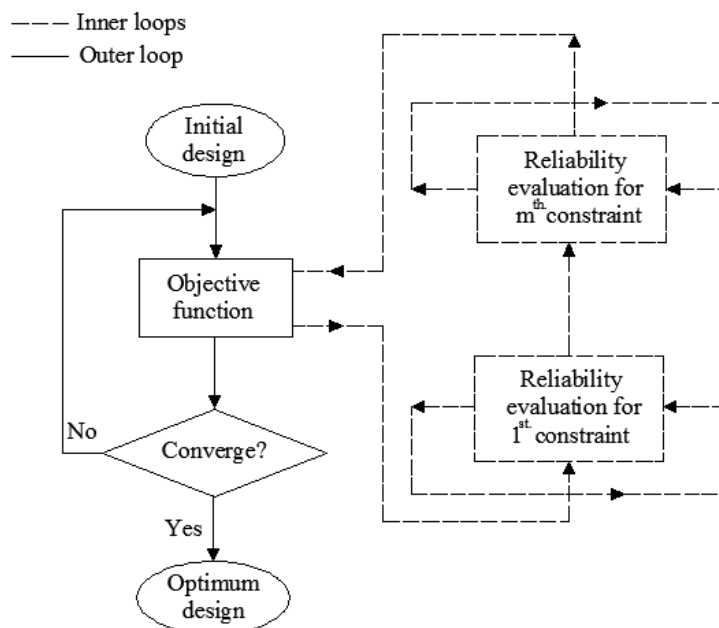
Figure 5.8: Double loop RBDO flowchart

5.5   Case studies

For case studies, firstly the RBDO is employed to find the optimal content of CNT as well as the optimal geometry of a nanocomposite component; and secondly, the sensitivity of the structural failure probability with respect to uncertain design variables is quantified. The two subsequent examples will show how the uncertainties influence the optimization of the structural performance and how the presented algorithm can capture the uncertainties effects. Note that hereinafter CNT, equivalent fiber and reinforcing agent are used interchangeably for sake of simplicity. Admittedly, readers should distinguish the difference between them during interpretation of the results. For example 7.5% fiber equivalent volume fraction as an output of the optimization algorithm, should be regarded as 5% CNT volume fraction in practice, subtracting the spatial volume of the CNT-polymer interphase region.

5.5.1   Three-point bending of a beam

The first example is a three point bending beam as already shown in Fig. 4.4(a). The cross sectional area of the beam is constant along its length. Fig. 4.4(b) also depicts the FE mesh while Table 5.1 indicates all design parameters of the beam. The design constraint is the mid deflection of the beam which should be smaller than an admissible value as mentioned in Table 5.1.

Table 5.1: Problem definitions for the beam under static loading

Parameter	L_x	L_y	E_m	v_m	$P(\mu/\sigma)$	$LSF(\delta_m)$	β	$obj.func.$
Value	5	1	10	0.3	760 / 10	0.0025	3	CNT %
Type	D	D	D	D	N	D	D	D

$Length : m, \ E : GPa, \ P : applied \ load \ (KN), \ v : Poisson's \ ratio, \ m : matrix, \ vol frac : volume \ fraction, \ D :$
$deterministic, \ N : normal \ distribution, \ \mu : mean \ value, \ \sigma : standard \ deviation, \ \beta : reliability \ index, \ \delta_m : Max. \ deflection$

Fig. 5.9(a) illustrates the reinforcing agent content as optimization objective function versus iterations; while the history of the reliability index is also presented. The same graphs are shown in Fig. 5.9(b), where the iteration is started from a different point. The final results are independent on the iteration start point yielding on optimum at 2.37% reinforcement. Results are based on the assumption of random waviness of the CNT in the resin according to the procedure discussed in Section 5.2.
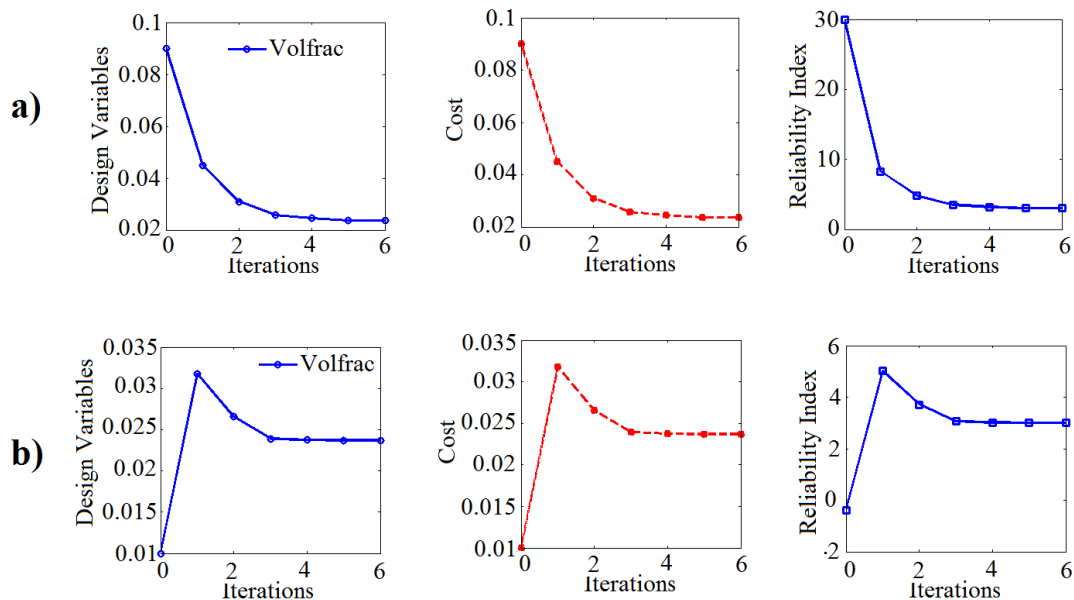
Figure 5.9: RBDO results of a three-point bending beam with initial guess of reinforcement content 9% (a) and 1% (b), optimum value is 2.37% for both (a) and (b)

Apart from finding the optimum content of the reinforcement agent, it is also important to determine how the uncertainties in the design parameters will affect the reliability of the nanocomposite structures. For this purpose, the CNT waviness and the agglomeration (material design parameters), the applied load (structural parameter) and the FE discretization (modeling parameter), have been selected for more detailed studies. According to [Rouhi & Rais-Rohani, 2013] and [Shokrieh & Rafiee, 2010d], the waviness is one of the key parameters governing the nanocomposite stiffness. The most influential parameter, the CNT content, has been optimized already.

To analyze the sensitivity of the failure probability with respect to the CNT waviness, other CNT parameters (i.e. length, dispersion, agglomeration and orientation) are considered as random parameters while the resin Young's modulus and its Poisson's ratio are considered as deterministic values because their effects on the overall characteristics of the composite are negligible [Rouhi & Rais-Rohani, 2013]. Five different levels of waviness have been defined as "waviness intensity" by limiting the upper and lower bounds of longitudinal and transverse stiffness of the RVE. In the first level (W-1: very fine waviness), the effective Young's modulus of the CNTRP is a random number between the Young's modulus of the RVEs with the longitudinal and 18° aligned CNTs (with respect to longitudinal direction). So, the effective Young's modulus for W-1 has a value between 80% and 100% of the stiffness of the RVE with longitudinally aligned CNTs. Similarly, this concept can be extended to have wavier CNTs (i.e. W-2: fine waviness, W-3: moderate waviness, W-4: severe waviness and W-5: very severe waviness) by setting a limit on the CNT incline angle. Thus W-2, W-3, W-4 imply that the effective Young's modulus of CNTRP has a value between $60\% - 100\%$, $40\% - 100\%$ and $20\% - 100\%$ of the stiffness of the RVE with longitudinal CNTs, respectively. W-5 also stands for the generic case which effective stiffness of the nanocomposite can take a random value between longitudinal and transverse stiffness of the RVE. Fig. 5.10 schematically demonstrates the definition of the so called "waviness intensity" concept. Fig. 5.11(a) depicts the Young's mod-
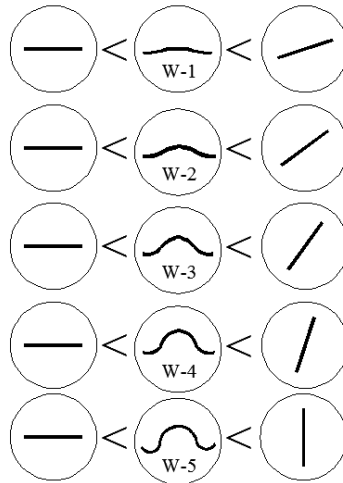
Figure 5.10: Definition of waviness intensity, a phenomenological concept

ulus of the CNTRP versus the reinforcing contents for different waviness intensities. Expectedly, an increase in content of reinforcement or decrease in the CNT waviness yields to higher composite Young's modulus. Fig. 5.11(b) shows the reliability index of the beam versus waviness intensity, for the optimum content of the reinforcement (i.e. 2.37%) while other parameters do not experience any variation. Evidently, when

the waviness increases, the structural stiffness will decrease. Hence, the beam deflection will increase and consequently the structural reliability will decrease. One should note that for the case of fully wavy CNT (i.e. W-5), the structural reliability is half the reliability of a very fine wavy CNT (i.e. W-1).
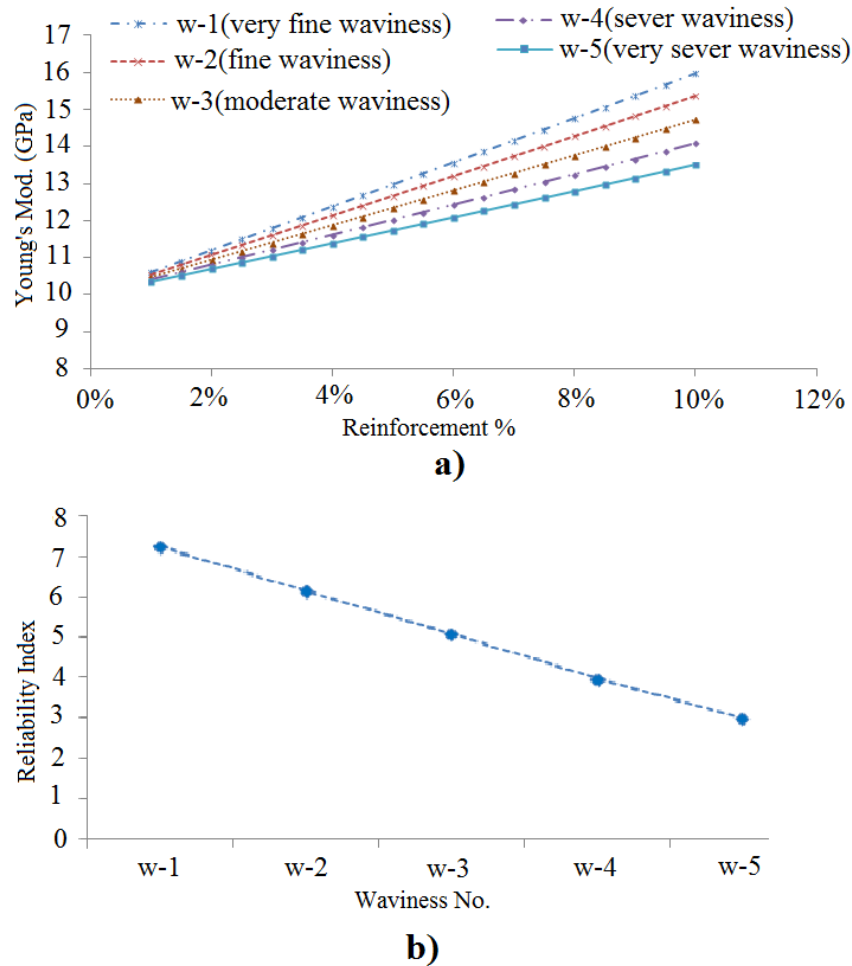
Figure 5.11: Stiffness of CNTRP versus reinforcement content for different waviness intensities (a), Reliability index of the beam versus waviness (b)

Fig. 5.12 illustrates the effect of the CNT agglomeration on the reliability of the nanocomposite component. The Young's modulus of CNTRP versus the reinforcement contents for both aggregated and non-aggregated CNTs is plotted in Fig. 5.12(a). The CNT agglomeration, reduces the CNTRP stiffness. This reduction is more pronounced for higher values of CNT contents; for CNT contents around 2% and less, the agglomeration role can be neglected. Fig. 5.12(b) shows the failure probability of the beam versus the reinforcement content with and without the CNT agglomeration. Agglom-

eration also increases the failure probability of the structure but as it can be seen from Fig. 5.12, its effect can be neglected (maximum difference in failure probability considering and disregarding CNT agglomeration is 0.144) without any structural safety concern.

The second category of uncertainties (structural uncertainties) is considered in next step, assuming a fully wavy CNT (i.e. W-5). Fig. 5.13 shows the reliability index and the failure probability of the beam in dependence on the standard deviation of the loading distribution. When the standard deviation increases, the failure probability also increases and β decreases. The rate of the reliability index changes rapidly for small standard deviations and gradually approaches zero (i.e. the system response is not sensitive anymore). An increase in the standard deviation of the loading leads to a more uncertain system that is more susceptible for failure.

Finally the influence of the discretization on the structural reliability is observed. Fig. 5.14 depicts the failure probability versus the mesh size parameter, h, which has been defined as the ratio between the beam height and the number of elements in the vertical direction. It could be observed that coarse meshes considerably underestimate the structural failure probability while next to $h = 0.05$, the failure probability reaches a constant value.

5.5.2 Thick cylinder under radial line load

The second example is a thick cylinder under radial distributed loading. Due to geometrical symmetry, only half of the ring is discretized. Fig. 5.15(a-c) and (d) depicts the geometry, loading / boundary conditions, FE discretization and deformed configuration, respectively. Table 5.2 lists all design parameters. In this example not only the material but also the geometry is simultaneously optimized. At the first step, the minimization of the CNT content and the cylinder thickness as optimization objective function, $1\% < volfrac < 10\%$ and $0.1 < t_c < 0.4$ as deterministic design constraints and the maximum transverse deflection with a specified target reliability index (according to Table 5.2) as stochastic constraint have been taken into account.

Table 5.2: Problem definitions for thick cylinder under line load

Parameter	R_c	L_c	E_m	v_m	$P(\mu/\sigma)$	$LSF(\delta_m)$	β	$obj.func.$
Value	1	1.5	10	0.3	1000 / 200	0.007	3	%CNT+t_c
Type	D	D	D	D	N	D	D	D

Length : m, E : GPa, P : applied load (KN/m), v : Poisson's ratio, m : matrix, c : cylinder, D : deterministic, N : normal distribution, μ : mean value, σ : standard deviation, β : reliability index, δ_m : Max. tarns. deflect.

The RBDO results are illustrated in Fig. 5.16(a). The optimal thickness and reinforcement content are 0.278 and 1%, respectively. In order to check the correctness of the present approach the ring thickness is restricted to an optimum 0.278 in the next simulation. This new constraint is imposed by changing the deterministic constraints

a)

b)
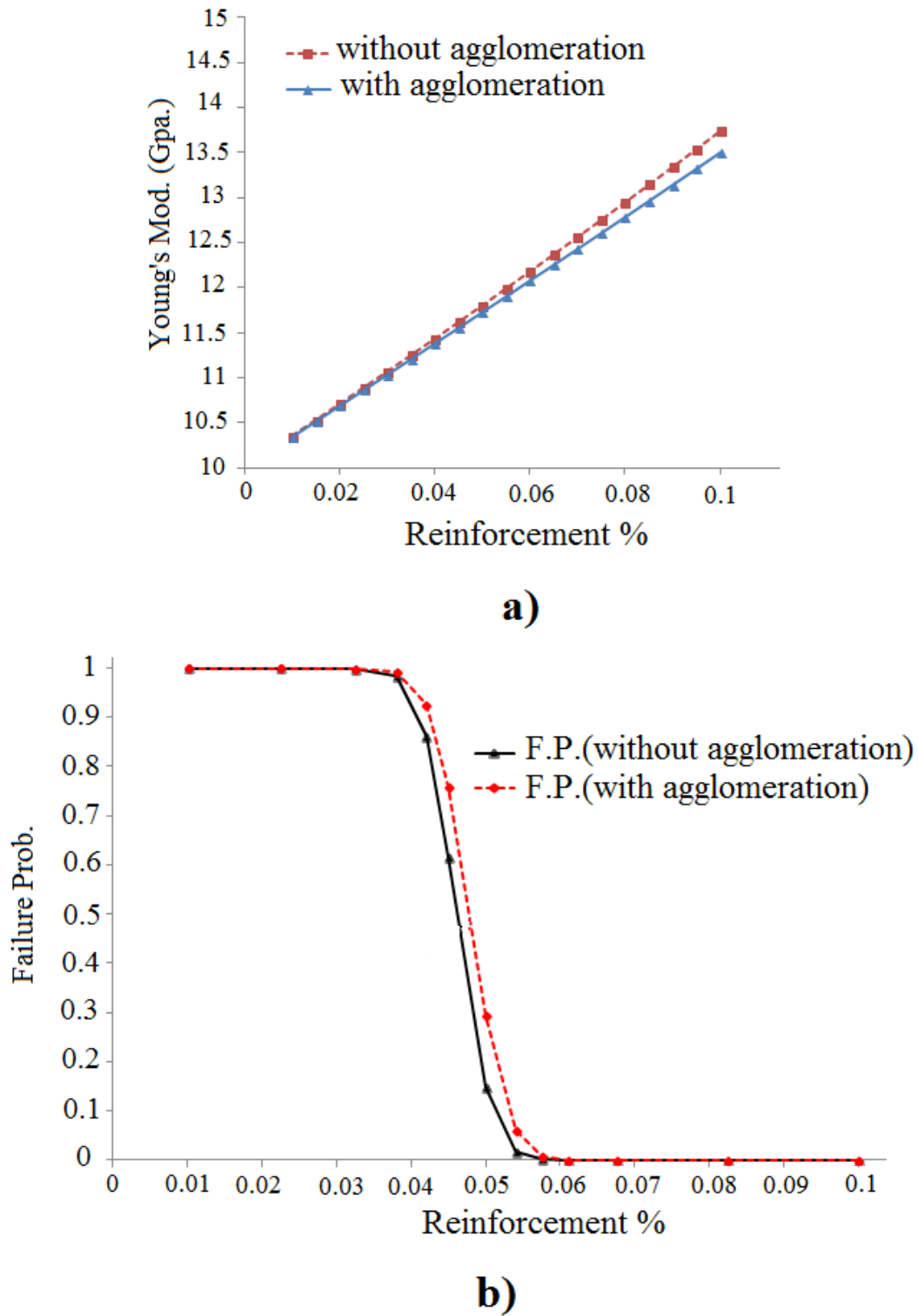
Figure 5.12: Stiffness of CNTRP versus reinforcement contents with and without CNT agglomeration (a), Failure probability of the beam versus reinforcement contents with and without CNT agglomeration (b).
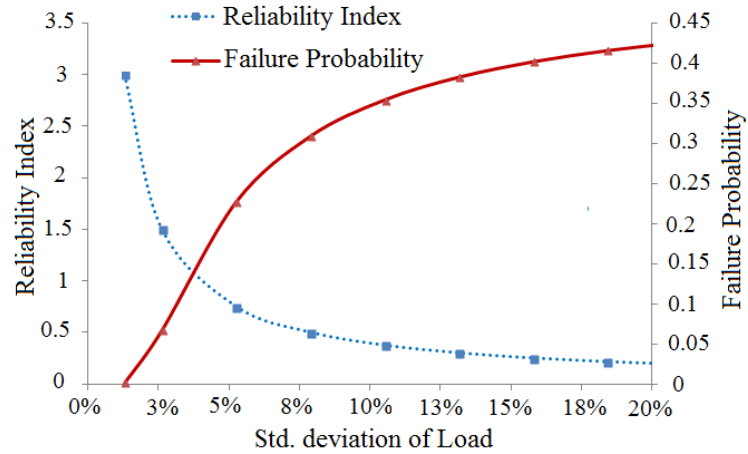
Figure 5.13: Reliability index and failure probability of the beam versus standard deviation of load.
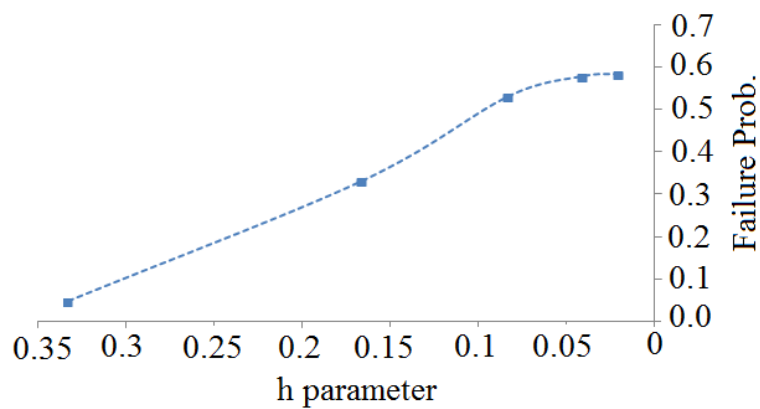
Figure 5.14: Reliability index versus FE mesh, *h*, parameter which is defined as the ratio between the beam height and the number of elements in the vertical direction
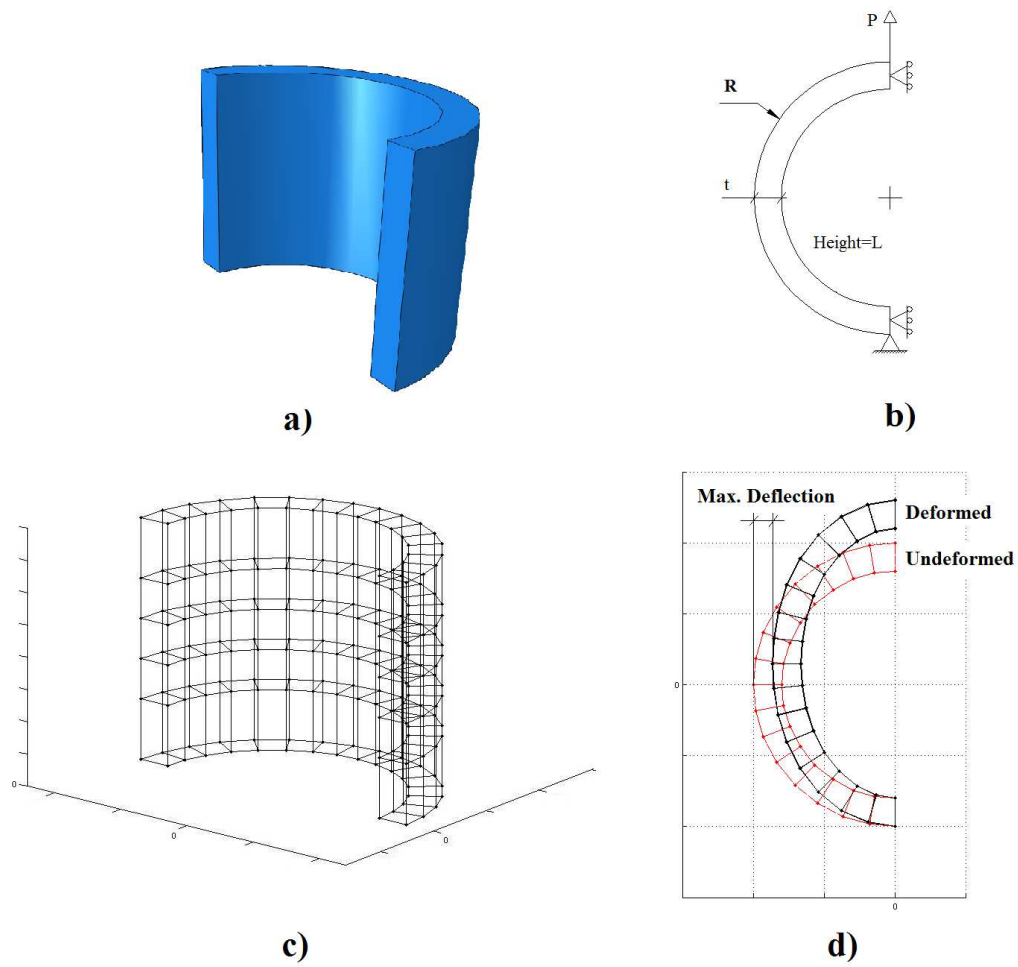
Figure 5.15: Geometry (a), loading / boundary conditions (b), FE mesh (c) and deformed configuration (d) of a thick cylinder under radial line load

to $1\% < volfrac < 15\%$ and $0.1 < t_c < 0.26$. To obtain the same reliability index, the effect of the thickness reduction should be compensated by another design variable, i.e. the CNT content. Fig. 5.16(b) shows the results under the new constraints. The optimal thickness now is 0.259 (quite close to constraint's upper limit) while the optimum reinforcement content is increased up to 9.35%.
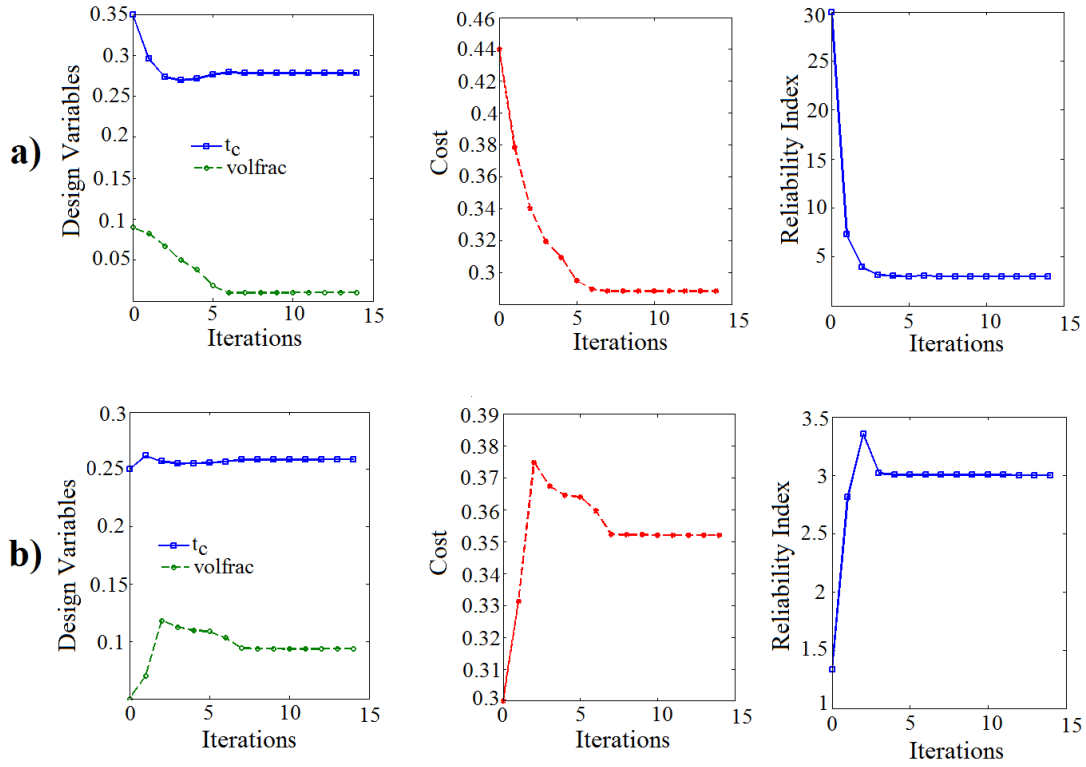
Figure 5.16: RBDO results of a thick cylinder under radial line load for design constraints as $1\% < volfrac < 10\%$, $0.1 < t_c < 0.4$ (a) $1\% < volfrac < 15\%$ and $0.1 < t_c < 0.26$ (b) for both cases t_c and $volfrac$ stand for ring thickness and reinforcement content, respectively

Subsequently, the minimization of both CNT content and cylinder volume have been followed considering the deterministic constraints $1\% < volfrac < 10\%$, $0.1 < t_c < 0.3$, $1.2 < L_c < 1.7$, $0.9 < R_c < 1.1$ and the stochastic design constraint according to Table 5.2. As Fig. 5.17 shows, $volfrac = 9.34\%$, $R_c = 0.9333$, $L_c = 1.333$ and $t_c = 0.2032$ are optimal values of the design parameters.
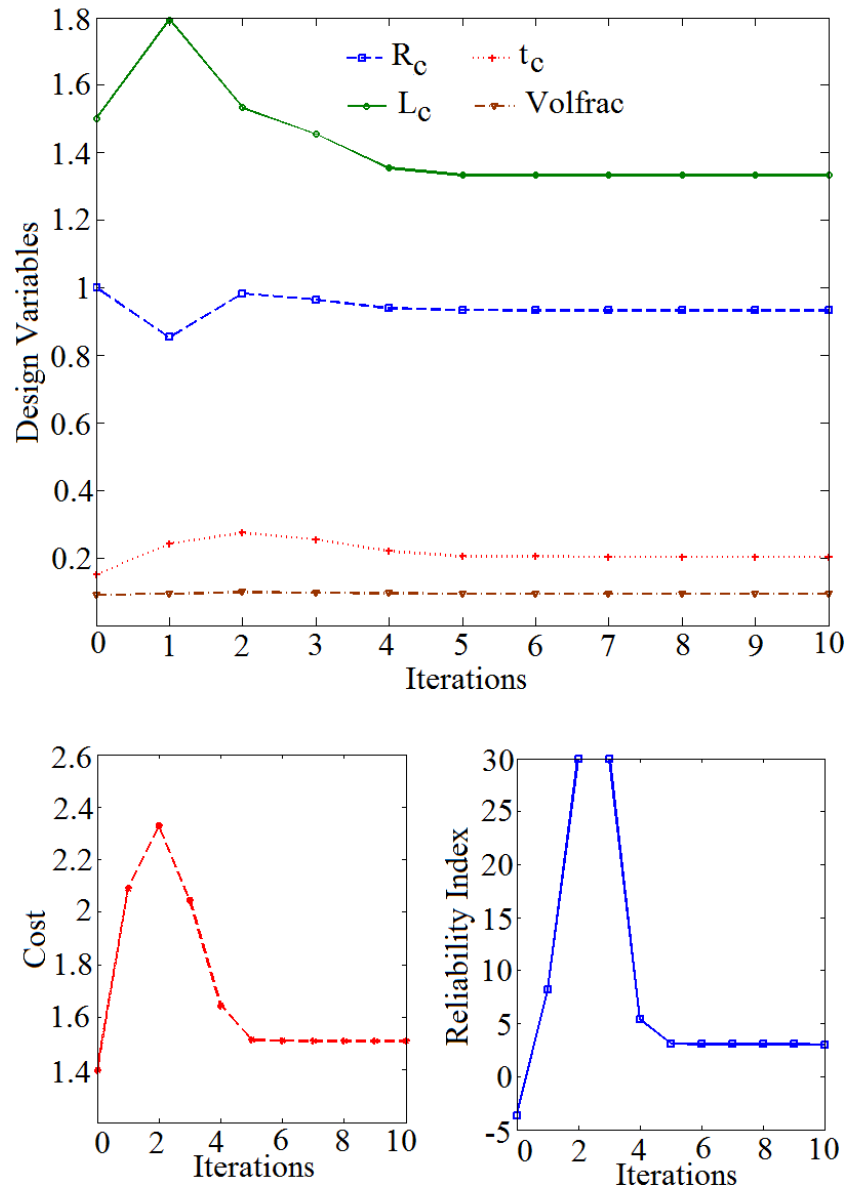
Figure 5.17: RBDO results of a thick cylinder to find min. reinforcement content and min. volume of cylinder including deterministic design constraints as $1\% < volfrac < 10\%$, $0.1 < t_c < 0.3$, $1.2 < L_c < 1.7$, $0.9 < R_c < 1.1$ and stochastic constraint as maximum transverse displacement equal to 0.007 with $b = 3$

5.6 Concluding remarks

Deterministic approaches for nanocomposite modeling and optimization might be unrealistic for certain applications and may yield to either catastrophic failure or unnecessary conservatism. Although probabilistic approaches can cover uncertainties effects, their implementations do not necessarily yield reliable nanocomposite designs. Detailed investigations on uncertainties and their propagation should be performed for realistic and reliable PNC structures. Uncertainty propagation over different length scales and through various sources have been addressed for nanocomposite components. Potential uncertainties have been categorized in material, structural and modeling levels. To fully address uncertainties in material level, a stochastic multi-scale material model (which includes all important aspects of the CNTRP including CNT length, orientation, dispersion, agglomeration and waviness, at different length scales from nano-, up to macro-scale) has been utilized. To improve the computational efficiency, the evaluation of material properties has been surrogated by a metamodel. The results for two selected examples show that the failure probability of a polymeric nanocomposite structure, strongly depends on the CNT parameters, especially the CNT volume fraction and the waviness. The influence of the CNT agglomeration is nearly negligible. It was observed that neglecting the CNT agglomeration can simplify the model and decrease the computational time without remarkable loss in model accuracy. Furthermore, the loading condition and discretization affect the reliability of the system. Coarse meshes underestimate the failure probability of a beam while fine meshes admittedly increase computational cost. Thus sufficiently refined discretization should be investigated in order to have realistic assessment of the reliability of PNC structures. An increase in the standard deviation of the applied load, which physically means more uncertainties in the system, resulted in the structure with a smaller reliability index. Finding the optimal content of CNT was also presented to optimized the material instead of the geometry. As a further step forward, concurrent optimization of material parameters and geometrical parameters (hybrid optimization) was conducted to present a comprehensive solution for current demands in fully optimized designs of nanocomposite components.

Chapter 6

Reliability and NURBS based sequential optimization approach

6.1 Introduction

Generally, increasing the fiber volume fraction in a Fiber Reinforced Composite (FRC) material will increase its structural strength and stiffness. However the existence of a practical upper limit should be considered. Normally, composite structural elements under mechanical actions have some regions which are on the edge of design constraints (e.g. the maximum allowable stress is exceeded) and can be identified as failure zones. Usually these failure zones dictate the required content of the reinforcing element in order to get a properly strengthened overall structure, fulfilling everywhere the design constraints. Considering uniform distribution of fibers through the structure, initially safe regions that already fulfill the design constraints will inevitably increase their fiber content. Thus, an efficient optimization approach which seeks towards optimal fiber content (see Chapter 5) should also pay attention to optimal distribution of fibers in order to strengthen only those portions of the structure (failure zones) for which it is necessary to improve their bearing capacity. From the above discussions it appears that the joint manipulation of these two parameters (i.e. fiber content and its distribution) while available uncertainties are also addressed, will be a necessary approach towards more efficient and reliable structural optimization.

6.2 Double sequential stages optimization procedure

The sequential optimization algorithm is schematically illustrated in Fig. 6.1. In this approach there are two successive optimization stages. Stage 1 includes a stochastic fiber content optimization algorithm and stage 2 includes a fiber distribution optimizer. In the first stage, based on the nature of the problem, the designer can decide which

parameters would be deterministic and which ones probabilistic. He can also set the initial values of the parameters, variables and solution settings. Traditional RBDO is implemented by use of a nested or double loop approach. In this method, each step of the iteration for design optimization involves another loop of iteration for reliability analysis (i.e. FORM). In this stage, minimization of fiber content is considered as optimization objective function and after convergence, the output is used as the input for the second stage. In the second stage, NURBS finite elements which are implemented and used for domain discretization, define continuous and smooth mesh independent fiber distribution function by using the nodal volume fractions of fibers as the optimization design variables. The second stage is initialized by using the fiber volume fraction value, coming as stage 1. Afterwards Optimality Criteria (OC) updates design variables. This computational procedure is executed iteratively, until no sensible changes occur in design variables (See Chapter 4).

In the presented model, two separate reliability indices (β_1 and β_2) are introduced: β_1 is the first stage reliability index (which is used for obtaining optimal fiber volume fraction through the RBDO in stage 1) and the second reliability index, β_2, is the target reliability index of the final optimized structure. β_2 represents the reliability index of the structure after fiber distribution optimization. β_1 is the model input (set by designer at the first run of the algorithm) while β_2 is the output of the model. Clearly, $\beta_1 < \beta_2$ because it is supposed that fiber distribution optimization increases the performance (such as the stiffness) of the model and provides a more reliable structure.

It is however possible to implement concurrent approach for coupling stage 1 and stage 2. In the concurrent approach (Fig. 6.2) the fulfillment of the fiber distribution optimization before evaluation of LSF is necessary in every realization of stage 1. Thus, this alternative method is computationally expensive. To see more clearly the issue, we can assume that the computational parameter of total elapsed time (T_{total}) is proportional to the number of LSF call (n_1), each call run time (t_{LSF}) and the subtotal time required for fiber distribution optimization (t_2). Taking into account the above, for the sequential model the total time is proportional to the sum of the above mentioned times, i.e:

$$T_{total\,se} \propto (n_1 \times t_{LSF} + t_2) \tag{6.1}$$

while for concurrent model we have:

$$T_{total\,co} \propto [n_1 \times (t_{LSF} + t_2)] \tag{6.2}$$

as $n_1 > 1$, thus, $T_{total\,se}$ is smaller than $T_{total\,co}$. We can write:

$$(T_{total\,co} - T_{total\,se}) = \Delta T \propto [(n_1 - 1)t_2] \tag{6.3}$$

We can use a quantitative example in order to clarify the above issue. A simple case where t_2 and n_1 are equal to 20 minutes and 10 calls respectively, the present model
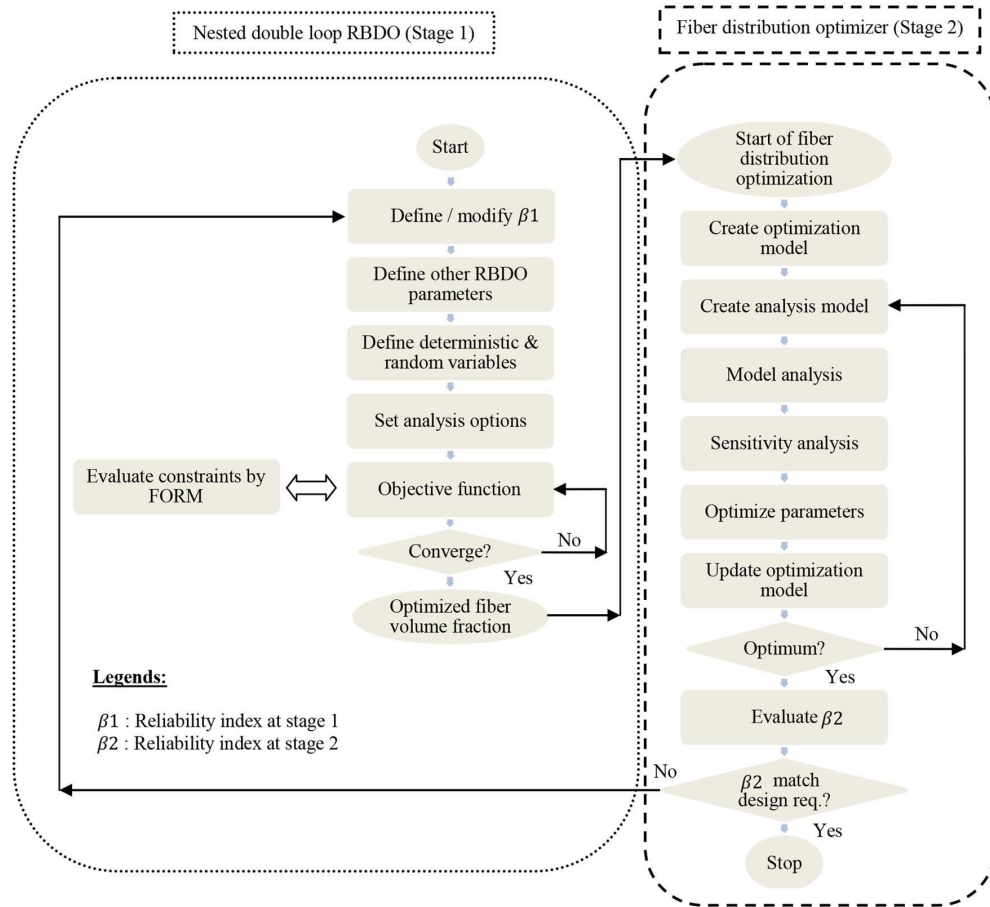
Figure 6.1: Double sequential stages optimization algorithm

is 180 minutes faster than the concurrent model. The computational advantage of this model is more evident when readers observe that t_2 and n_1 are considerably higher in real cases.
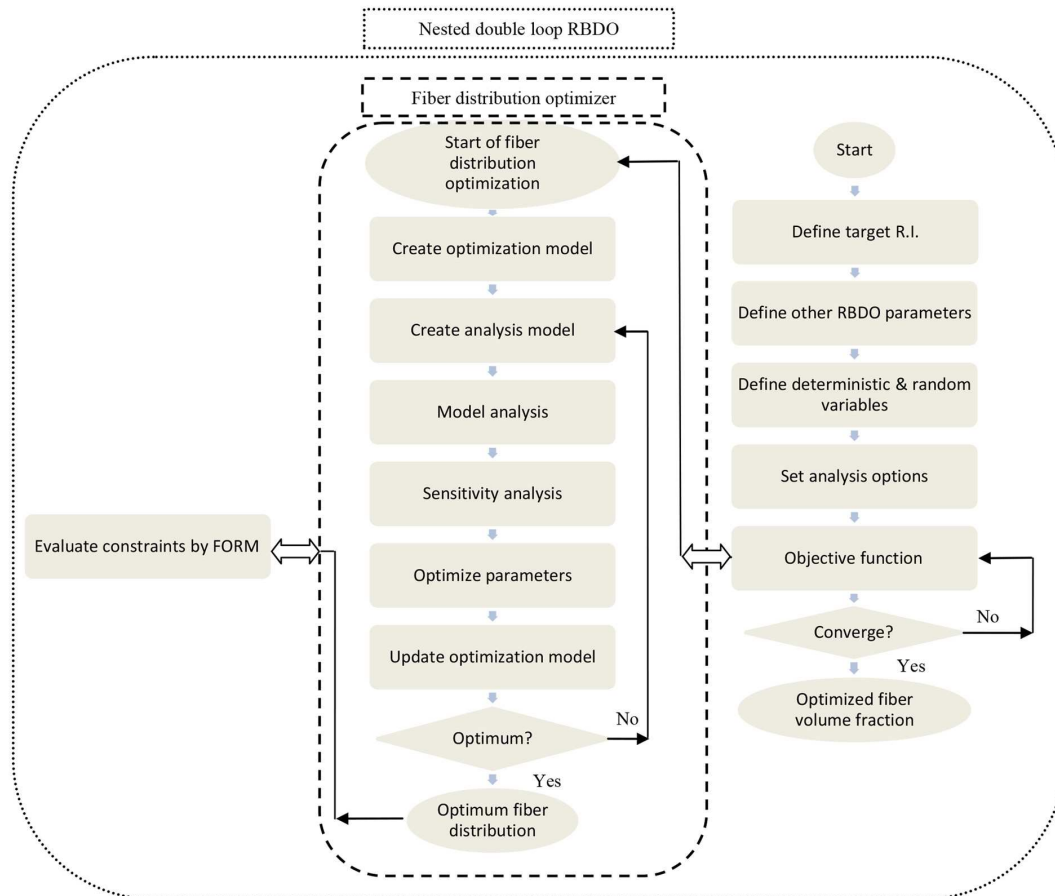
Figure 6.2: Concurrent optimization algorithm

6.3 Case studies

The aims of this section are firstly to verify the correctness and secondly to demonstrate the performance of the proposed model. Moreover the discussions related to the two presented examples will show how uncertainties influence the optimization of structural performance and how the presented algorithm can capture the effects of the uncertainties.

6.3.1 Cantilever beam under static loading, verification of the model

The first example involves a RBDO benchmark problem of a cantilever beam presented in [Togan & Daloglu, 2006] and shown in Fig. 6.3. The beam length (L) is assumed to be equal to 100 inches with constant cross section area along its length. The objective function corresponds to the minimization of the beam weight or equivalently, the cross section area ($w.t$). The limit state deals with the displacement at the free end of the beam, where the displacement attains its maximum value. F_x and F_y are independent random loads in x and y directions. R is random yield strength and E is Young's modulus. To verify the stochastic framework of the model, initially the analytical limit state function corresponding to the maximum displacement at the free end of the beam is considered. Other design parameters are assumed exactly equal to those in the benchmark problem ([Togan & Daloglu, 2006]) and are summarized in Table 6.1.
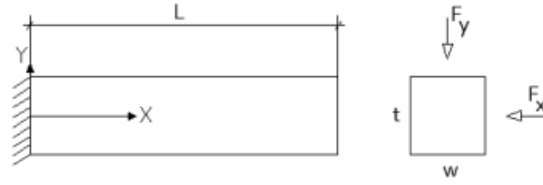
Figure 6.3: Schematic of the cantilever beam

Table 6.1: Benchmark problem definitions for cantilever beam under static loading

Parameter	L	R	F_x	F_y	E	w	t	β_1
Value	100	$\mu = 40000$	$\mu = 40000$	$\mu = 40000$	$\mu = 29e6$	$\mu = 4$	$\mu = 4$	3
		$\sigma = 2000$	$\sigma = 2000$	$\sigma = 2000$	$\sigma = 1.45e6$	$\sigma = 0.001$	$\sigma = 0.001$	
Type	D	N	N	N	N	N	N	D

L : Length, R : yield strength, F_x, F_y : load, E : Young's Modules, w,t : width, thickness D : deterministic, N : normal distribution, μ : mean value, σ : standard deviation, β : Reliability index

Table 6.2: RBDO results using analytical limit state

Method	w	t	$F = w.t$
[Togan & Daloglu, 2006]	2.700	3.410	9.206
Present Model	2.702	3.408	9.206

w, t : width, thickness, F : objective function

Table 6.2 compares the obtained results and the benchmark ones and shows that there is an agreement between them. In the next step the off-plane load (F_x) is set equal to zero in order to solve the problem in 2-D space while keeping the beam depth equal to unity. Results which are obtained by using two different limit state functions (i.e. analytical formula and those calculated by finite elements) are compared with each others in Table 6.3. Once again a good conformity was obtained.

Table 6.3: RBDO results using FEM limit state

Method for evaluation of LSF	w	t	$F = w.t$
Analytical	1	4.0095	4.0095
FEM(NURBS)	1	4.0094	4.0094

w, t : width, thickness, F : objective function

6.3.2 Beam under three-point bending

In the present example the first objective function is to find the optimal fiber volume while the limit state is the deflection at mid of the beam must be smaller than an admissible value. The schematic view of the problem is already shown in Fig. 4.4 while Table 6.4 includes the design parameters.

Table 6.4: Problem definitions of the beam under static loading

Parameter	L_x	L_y	L_m	E_f	v	P	LSF	β_1	$Obj.Func.$
Value	5	1	$\mu = 20$	$\mu = 200$	0.1	$\mu = 1000$	Max. Deflect.	3	Fiber Volume
			$\sigma = 5$	$\sigma = 50$		$\sigma = 250$	$4e^{-3}$		fraction
Type	D	D	N	N	D	N	D	D	D

Length : (M), E : (MPa), P : applied load(N), v : Poisson's ratio, m : matrix, f : fiber, D : deterministic, N : normal distribution, μ : mean value, σ : standard deviation, β_1 : reliability index

Fig. 6.4 presents optimal values of fiber volume fraction for the beam with homogeneously distributed fibers versus the different maximum allowable deflection at mid of the beam and for different reliability indices. A mesh with 91 control points has been used to reduce computational cost. As expected, either demanding smaller beam deflection or greater reliability index for the beam, yield to increase in fiber volume fraction of the FRC beam. The figure also depicts that for large reliability indices (here 4 and 5) and when there is a small allowable beam deflection (here 5 *mm*), the obtained fiber contents are approximately the same.

Results of RBDO by using 1225 control points, which represents 4120 mesh sizes, are plotted in Fig. 6.5. For this (or higher) number of control points, the numerical solutions of the LSF have been verified to converge to the exact solution.

Fig. 6.6 compares the obtained values related to the assumed objective function for different numbers of control points (mesh sizes). As can be observed, the deviation between the obtained optimal fiber volume fractions by using 1225 or 325 control points is equal to 0.03 (i.e. 3%) but the computational time is reduced to be approximately less than one tenth. This fact underlines NURBS smooth and quick convergence characteristics which yield to noticeable saving in the time of the computation. In RBDO problem, LSF which depends on FE model results, should be evaluated many times. So, any reduction in its calculation time will significantly reduce the total elapsed time. Admittedly, this time saving is justified only in the case that accuracy of the results is also maintained. This takes place in the presented model while using coarse NURBS
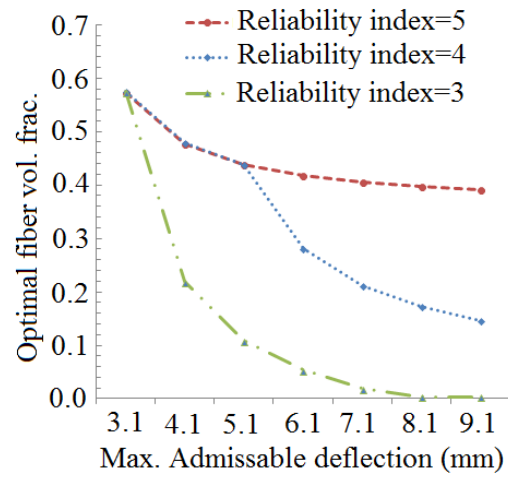
Figure 6.4: Fiber volume fraction versus change in maximum admissible deflection for different β
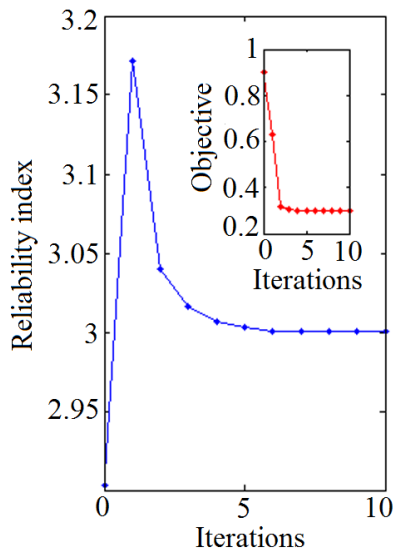
Figure 6.5: RBDO results of a three-point bending beam using 1225 control points

mesh for the evaluation of LSF, slightly changes in the accuracy of the results and leads to a significant decrease in RBDO computational time.
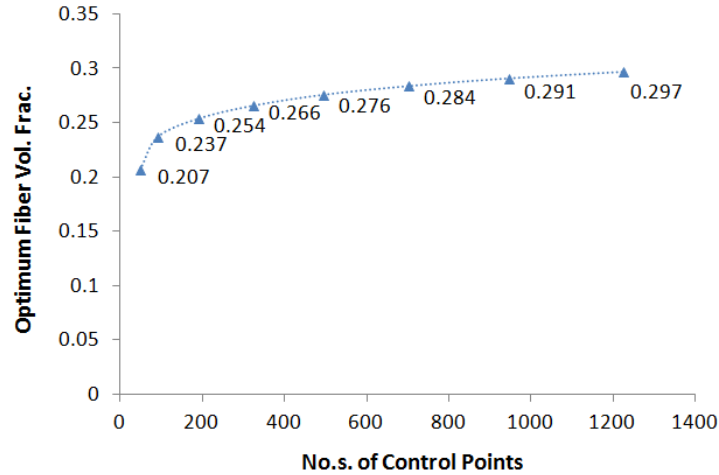
Figure 6.6: RBDO results versus number of control points (mesh size)

Once the optimal fiber content (by assuming $\beta_1 = 3$) is obtained (Fig. 6.7(a)), the second module optimizes the fiber distribution through the structure (Fig. 6.7(b)), with the aim to minimize the structural compliance. 703 control points are used for obtaining shown results. The obtained target reliability index at the end of stage 2 is $\beta_2 = 7.66$. This increase in reliability index is due to the effect of fiber distribution optimization on increasing the structural stiffness which consequently decreases the deflection of the structure. It is also noteworthy to mention that in this case the standard deviations of random variables are according to Table 6.4. If they are decreased to 70% and 40% of the current values without any change in other design parameters, since required fiber volume fractions decrease, the target reliability indices are also decreased to $\beta_2 = 6.65$ and $\beta_2 = 4.81$, respectively. Thus, we can conclude that fiber distribution optimization is more influential on increasing the reliability of the structure with higher level of uncertainties.
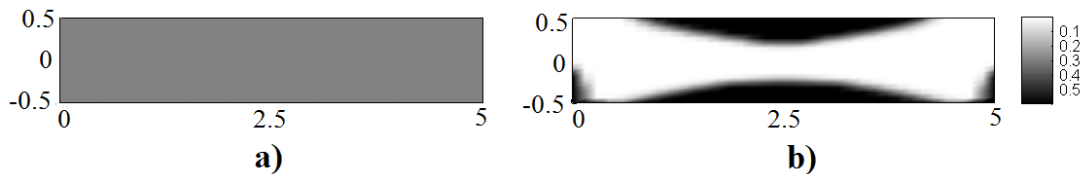
Figure 6.7: Three point bending wall beam problem using 703 control points with (a) homogenized fiber distribution and $\beta_1 = 3$, (b) optimized fiber distribution and $\beta_2 = 7.66$

6.3.3   Square plate with a central circular hole under tension

The classical problem of a square plate with a central hole under constant distributed edge load is assumed as the second example. Considering the double symmetry of the problem, just one quarter of the plate is modeled. Fig. 4.11(a) and (b) show the analysis model and the FE domain discretization. Table 6.5 shows the design parameters. The problem of obtaining optimal fiber volume fraction and distribution in order to have a reliable structure with limited deflection, is solved by using quadratic NURBS meshes.

Firstly, all the design parameters are considered as deterministic values, except the applied load which is considered as a random variable with different standard deviations. Obtained optimal fiber contents (by using 612 control points) are plotted versus the values of standard deviation of the applied load in Fig. 6.8.

Table 6.5: Problem definitions, Square plate with central hole

Parameter	L	R	E_m	E_f	v	P	LSF	β_1	$Obj.Func.$
Value	4	1	$\mu = 20$	$\mu = 200$	0.1	$\mu = 510$	Max. Deflect.	3	Fiber Volume
			$\sigma = 2$	$\sigma = 20$		$\sigma = 20, 30, 40, 50$	$6e^{-8}$		
Type	D	D	N	N	D	N	D	D	D

Length : (M), E : (GPa), P : applied load(N/m), v : Poisson's ratio, m : matrix, f : fiber, D : deterministic, N : normal distribution, μ : mean value, σ : standard deviation, β₁ : reliability index

Figure 6.8: Optimal fiber volume fraction versus standard deviation of applied load considering $\beta_1 = 3$ for 1- Random field (*load*), 2-Random fields (*load* $+ E_f$)and 3-Random fields (*load* $+ E_f + E_c$)

As can be seen, an increase in the standard deviation of the applied load (which means an increase in the uncertainty of the system) needs more fiber content. The system uncertainty will increase more when we consider the Young's modulus of fiber as another random field (i.e. 2-Random fields) and even more when the Young's modulus of the matrix material is also considered as a random variable (i.e. 3-Random fields).

In the case where only the applied load is assumed as a random variable (with mean value equal to 510 N/m and standard deviation equal to 50), the optimal fiber volume fraction is equal to 0.183. When E_f is also considered as a random variable, the optimal fiber volume is equal to 0.21. When E_m is not deterministic any more, the optimal fiber volume becomes 0.294. As can be seen, by increasing the number of random variables while keeping constant the reliability index (i.e. $\beta_1 = 3$), the required fiber volume fraction increases. Alternatively, for a constant fiber volume fraction if the number of uncertain variables of the problem increases, the reliability of the system decreases.

Using 612 control points, optimal fiber distribution leading to the minimum structural compliance is plotted in Fig. 6.9. Considering $\beta_1 = 3$, the target reliability index for this pattern of fiber distribution gives the value of $\beta_2 = 4.1$. Changes in β_1 will result in different values of β_2, for example for $\beta_1 = 2.5$ and $\beta_1 = 3.5$ the target reliability indices correspond to $\beta_2 = 3.78$ and $\beta_2 = 4.36$, respectively.
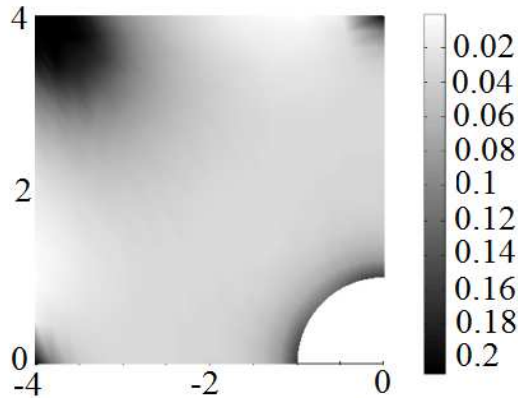
Figure 6.9: Optimal distribution of fibers with volume fraction 0.294 of plate with central hole subjected to constant loading, target reliability index $\beta_2 = 4.1$ (result for 612 control points)

6.4   Concluding remarks

An efficient sequential algorithm for finding the optimal fiber volume fraction and its distribution in structures made of FRC materials is presented. To overcome the cumbersome computational burden in stochastic optimization problems, finding the optimal fiber volume fraction and fiber distribution are performed sequentially, not concurrently. This technique along with using NURBS finite elements, allows us to get a noticeable reduction in the computational cost, without a noticeable loss in accuracy of the results. Assuming a random orientation of fibers in the matrix, in the

first optimization module (i.e. finding the optimal fiber volume fraction) uncertainties in the parameters (such as constituent's materials and loading) are fully addressed and LSF is evaluated by using First Order Reliability Method (FORM). In the second module (i.e. fiber distribution optimization) a NURBS surface which smoothly defines the fiber distribution pattern, is adopted. The presented numerical examples show as an increase in model uncertainties gives rise to unreliability of the system. More specifically, either the rise in the number of uncertain fields in the problem or the increase in the standard deviation of random variables needs more fiber content. It can be also concluded that when there is a higher level of uncertainties in design parameters, the fiber distribution optimization is more influential on increasing the reliability of the structure.

Chapter 7

Application 1: Interfacial shear stress optimization in sandwich beams

7.1 Introduction

Sandwich beams are a special class of composite materials fabricated by attaching two thin but stiff face sheets to a lightweight thick core which experiences mostly shear stresses. As a result of their high bending stiffness and high strength to weight ratios, sandwich beams have numerous applications in the automotive, aerospace, marine and construction industries [Manalo *et al.*, 2009]. A comprehensive review and assessment of various theories for modeling sandwich composites are presented in [Hu *et al.*, 2008]. Core shearing and debonding between core and face sheets are two common failure modes of these structures. Core shearing occurs when a sandwich beam is subjected to an excessive transverse shear force. Moreover, experimental evidence shows that debonding failure is influenced by the existence of a crack at the imperfect interface [Triantafillou & Gibson, 1989]. The excessive interfacial stresses between the core and the face sheet can be considered as a main cause for this failure.

To decrease the stress concentration at the interface, Functionally Graded Materials (FGMs) with continuously varying composition have been developed [Jha *et al.*, 2013]. However, Fiber Reinforced Composite (FRP) materials are also widely used in the core of sandwich beams. Available research on interfacial stresses optimization mainly concerns beams strengthened with FRP bonded plate. For instance, Krour *et al.*, 2013 and Lousdad *et al.*, 2010 tried to minimize interfacial stresses of a concrete beam strengthened with FRP plate, by finding optimal fiber orientation in the FRP plate and its end shape, respectively.

Motivated by the capabilities of the fiber distribution optimization algorithm for FRC structures which has been described in Chapter 4, the methodology is extended to present an optimization package for sandwich beams minimizing any stress state

within any arbitrary area of interest defined over the design domain. The advantages of this methodology include: The same data set is used for optimization and analysis, high convergence rate due to the smoothness of the NURBS, mesh independency of the optimal layout, no need for any post processing technique and its non-heuristic nature. In this chapter an adjoint sensitivity technique is also devised for flexible choice of regions where the stress reduction is demanded. The technique is used for efficient updating of the design variables during optimization iterations.

7.2 Introduction to FGM and homogenization technique

Mechanical characteristics at any point in FGMs depend on the volume fraction of its ingredients. The sum of the volume fraction of reinforcement V_c and the matrix V_m is equal to unity ($V_c + V_m = 1$). In a beam with a FG core, the volume fraction of reinforcement is assumed to follow the power law distribution

$$V_c = \left(\frac{1}{2} + \frac{y}{t_c} \right)^n \quad with \quad n \geq 0 \tag{7.1}$$

where n is a non-negative exponent, y is the distance from the midline of the core in the thickness direction and t_c is the FG core thickness. Fig. 7.1 depicts V_c versus the non dimensional thickness $\frac{y}{t_c}$, for different values of n. It is clear the mechanical properties of the FG core significantly depend on n.

For the sake of simplicity, the rule of mixtures as a classical homogenization approach is used in this chapter. The homogenization technique based on Mori & Tanaka, 1973 is also used for model verification purposes. A summary of the governing equations can be stated as follows:
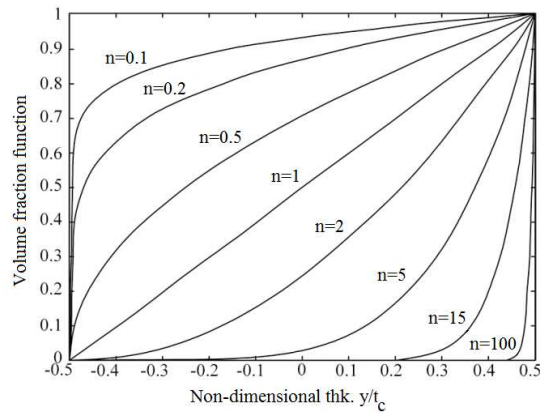
Figure 7.1: Volume fraction versus the non-dimensional thickness for various n of the FG core, figure from [Bui *et al.*, 2013]

7.2.1 Rule of mixtures (ROM) method

$$P_{eff} = P_m V_m + P_c V_c \tag{7.2}$$

By substituting Eq. (7.1) into Eq. (7.2) the effective Young's modulus E_{eff}, Poisson's ratio v_{eff} and mass density ρ_{eff} of the FG core are determined by

$$E_{eff} = E_m V_m + E_c V_c = (E_c - E_m)(\frac{1}{2} + \frac{y}{t_c})^n + E_m \tag{7.3}$$

$$v_{eff} = v_m V_m + v_c V_c = (v_c - v_m)(\frac{1}{2} + \frac{y}{t_c})^n + v_m \tag{7.4}$$

$$\rho_{eff} = \rho_m V_m + \rho_c V_c = (\rho_c - \rho_m)(\frac{1}{2} + \frac{y}{t_c})^n + \rho_m \tag{7.5}$$

7.2.2 Mori-Tanaka method

In contrast to the ROM, the Mori & Tanaka, 1973 scheme considers the forces between the matrix and particulate phases and accounts for the interaction of the elastic fields among neighboring inclusions. The effective bulk modulus K_{eff} and the effective shear modulus G_{eff} of a mixture of two constituents are determined by [Bui *et al.*, 2013]

$$\frac{K_{eff} - K_c}{K_m - K_c} = \frac{V_m}{1 + (1 - V_m)\tilde{K}} \quad with \quad \tilde{K} = \left(\frac{K_m - K_c}{K_c + \frac{4}{3}G_c}\right) \tag{7.6}$$

$$\frac{G_{eff} - G_c}{G_m - G_c} = \frac{V_m}{1 + (1 - V_m)\tilde{G}} \quad with \quad \tilde{G} = \left(\frac{G_m - G_c}{G_c + \frac{G_c(9K_c + 8G_c)}{6(K_c + 2G_c)}}\right) \tag{7.7}$$

where (K_c, G_c) and (K_m, G_m) are the bulk and the shear modulus of the reinforcement and matrix constituents respectively, obtained by

$$K_l = \frac{E_l}{3(1 - 2v_l)}; \quad G_l = \frac{E_l}{2(1 + v_l)} \quad with \quad l = m, c \tag{7.8}$$

Finally, the effective Young's modulus (E_{eff}) and Poisson's ratio (v_{eff}) are given by:

$$E_{eff} = \frac{9K_{eff}G_{eff}}{3K_{eff} + G_{eff}} \quad and \quad v_{eff} = \frac{3K_{eff} - 2G_{eff}}{2(3K_{eff} + G_{eff})} \tag{7.9}$$

7.3 Material discontinuity

In a sandwich beam, material properties for the core and the face sheets are different, so the displacement solution at the interface of the core and the face sheets is only C^0 continuous and the strain field (displacement gradient) is discontinuous across the material interface. It means there is discontinuity in gradient field. In classical C^0 FEM, weak discontinuities can be automatically captured, if the material interface is located on an element boundary (conforming mesh). However, for problems with curved interfaces, using conforming meshes may be cumbersome, especially when such interfaces evolve. Several advanced methods like the Extended Finite Element Method (XFEM) [Duddu *et al.*, 2008 and Zhao *et al.*, 2013], XIGA [Ghorashi *et al.*, 2012 and Jia *et al.*, 2014], Meshless [Zhuang *et al.*, 2012 ; Rabczuk & Belytschko, 2004 ; Rabczuk *et al.*, 2007 and Rabczuk & Belytschko, 2007] and the Numerical Manifold Method (NMM) [Cai *et al.*, 2013] have been developed for capturing material discontinuity using non conforming mesh. Recently Nguyen *et al.*, 2014 proposed very simple approaches to handle such discontinuities in IGA for composite delamination using knot insertion for cohesive interfaces.

In IGA, continuity across an interior element boundary directly depends on the polynomial order and the multiplicity of the corresponding knot. Thus, knot insertion can be used to tailor the continuity of the fields along element interface (see Fig. 7.2). Taking the knot vector in 1D as $N = \left\{\xi_1, \xi_2, ..., \xi_{n+p+1}\right\}$, where ξ_i is the ith knot, n is the number of basis functions and p is the polynomial order, the basis functions across knot ξ_i are $p - m_i$ times continuously differentiable or C^{p-m_i} continuous; where m_i is the multiplicity of knot ξ_i.

Fig. 7.2(a) and (b) present the physical and parametric spaces; Fig. 7.2(c) and (d) compare supports of the shape functions for interior (entirely inside the core or the face sheets) and interfacial elements. According to Fig. 7.2(c), control points corresponding to interior element No. 1 are $\{1, 2, 3, 4, 5, 6, 7, 8, 9\}$ and for interior element No. 2 are $\{4, 5, 6, 7, 8, 9, 10, 11, 12\}$. Two rows of control points (i.e. row $\{4, 5, 6$ and row $\{7, 8, 9\})$ are in common between these two elements. These shared control points produce overlapping shape functions as illustrated in Fig. 7.2(c). In other words, the shape functions extend beyond the elements (C^1 continuity). In contrary to the interior elements, interfacial elements have at least one edge on the material interface. Two of these elements (elements Nos. 3 and 4) are shown in Fig. 7.2(d). These two elements have only one row of control points (i.e. row $\{27, 28, 29\}$) in common due to repeated knot at the interface. This knot insertion imposes C^0 continuity in the displacement field at the position of the material interface. As shown in Fig. 7.2(d), the shape functions of elements Nos. 3 and 4 do not overlap with each others.

In the present optimization methodology, control points which define the geometry of the model, contain the nodal volume fractions of the reinforcement as optimization design variables. Note that this is an advantage due to the smoothness provided by the
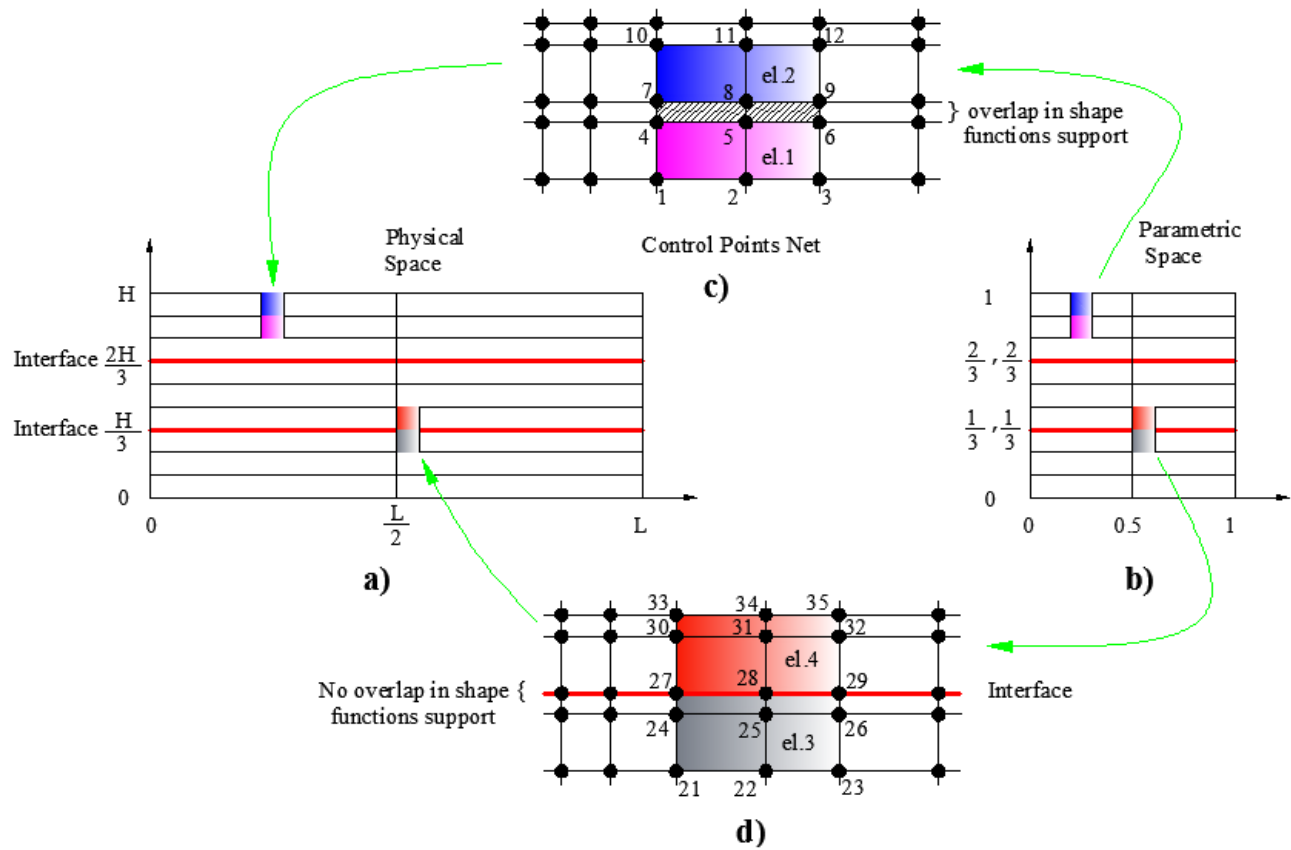
Figure 7.2: Schematic illustration of C^1 and C^0 continuity of quadratic NURBS elements, (a) physical mesh (b) parametric mesh (c) typical elements on single material without interface with C^1 continuity (d) typical elements on material interface with C^0 continuity

NURBS functions and the simplicity of dealing with only one approximation space for the geometry, reinforcement distribution and analysis. Though single knot insertion suffices to capture weak discontinuities in the analysis of sandwich beam models using IGA, it does not properly represent the situation arising at the neighborhood of material interface in the reinforcement distribution surface. Assume that material interface is being C^0 continuous. Thus, according to Fig. 7.2(d) there is a single row of control points (denoted by $\{27, 28, 29\}$) located at the interface in physical space. No control point can contain more than one value of nodal volume fraction of reinforcement as design variable in one optimization iteration. For element No. 3 corresponding control points are $\{21, 22, 23, 24, 25, 26, 27, 28, 29\}$and their counterpart design variables are $\{\varphi_{21}, \varphi_{22}, \varphi_{23}, \varphi_{24}, \varphi_{25}, \varphi_{26}, \varphi_{27}, \varphi_{28}, \varphi_{29}\}$. Analogously for element No. 4, $\{27, 28, 29, 30, 31, 32, 33, 34, 35\}$ and $\{\varphi_{27}, \varphi_{28}, \varphi_{29}, \varphi_{30}, \varphi_{31}, \varphi_{32}, \varphi_{33}, \varphi_{34}, \varphi_{35}\}$ are the vector of corresponding control points and the vector of design variables, respectively. Here $\{\varphi_{27}, \varphi_{28}, \varphi_{29}\}$ are common design variables between element Nos. 3 and 4. Since element No. 3 is located in face sheet and it is supposed that the face sheet material composition is fixed and does not change during the optimization, we set all design variables related to the face sheets to unity. So, $\{\varphi_{27}, \varphi_{28}, \varphi_{29}\}$ as a part of the face sheet should be a unit vector. However, they also belong to element No. 4 in the core of the beam with different nodal values. To overcome this discrepancy, C^{-1} continuity at the interface is imposed via the insertion of one additional knot (in total 3 knots at the parametric interface). In this case a new row of control points will coincide with the existing ones. Half of them contain the face sheet characteristics and the other half contains the core characteristics. Continuity in the displacement field along the interface is enforced by the penalty method. Fig. 7.3 schematically illustrates the implemented technique. Red dots represent interfacial control points which are duplicated and coincident at the interfaces. Green ones show typical interior control points.
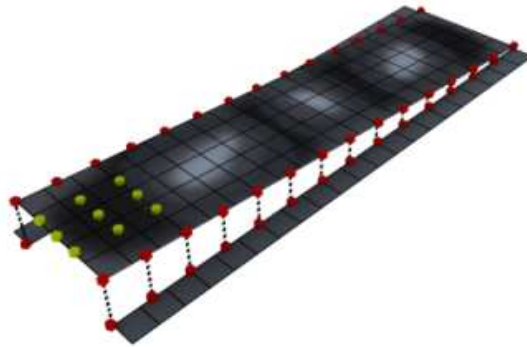
Figure 7.3: Exploded view of the sandwich beam modeled as multi-patches and glued with penalty method results in C^{-1} continuity. Interfacial control points are denoted by red dots and are coincident at interfaces. Green dots are typical interior control points

7.4   Overview of optimization methodology

As mentioned before, NURBS basis functions are used in this work not only for the analysis but also to model the reinforcement distribution. In the present methodology the nodal reinforcement volume fraction ($\varphi_{i,j}$) on control points are defined as design variables and the reinforcement distribution (η_p) is approximated as NURBS surface. Every point in the parametric space is mapped to the physical space having two attributes, geometrical coordinates and reinforcement volume fraction value. Due to the intrinsic characteristics of NURBS (higher order continuity and compact support, see [Cottrell *et al.*, 2009]), even coarse meshes yield smooth enough surfaces to clearly represent the optimization results without needing any further image processing techniques.

The distribution function $\eta_p(x,y)$, which indicates the amount of reinforcement at every design point (x,y), is defined by Eq. (4.9) and used for obtaining the homogenized stiffness. Once the reinforcement volume fraction at each point is available, the equivalent mechanical characteristics of the domain are obtained through the rule of mixtures

$$C_{eq}(x,y) = (1 - \eta_p)C_m + \eta_p C_c \qquad (7.10)$$

where C_{eq}; C_m and C_c are the homogenized, the matrix and the reinforcement elastic tensors, respectively. Subsequently, C_{eq} will be denoted by C. Since the core experiences mostly shear stresses, without loss of generality, the average value of the shear stresses within the area of interest is considered as the objective function. Other stress components (i.e. bending and peeling) can be also taken into account in the same manner. For the plane stress assumption, the stress in a vector form ($\boldsymbol{\sigma} = \{\sigma_{xx}, \sigma_{yy}, \sigma_{xy}\}$) is given by

$$\boldsymbol{\sigma} = \boldsymbol{Tu} = \boldsymbol{CQu} \qquad (7.11)$$

and also

$$\sigma_{xy} = t_{xy}\boldsymbol{u} = C_{xy}\boldsymbol{Qu} \qquad (7.12)$$

where $\boldsymbol{T}$ is the stress matrix of the element, $(.)_{xy}$ is the related row of $(.)$ corresponding to the xy direction and $\boldsymbol{Q}$ is the matrix containing the derivatives of the shape functions. Thus, the objective function ($J(\boldsymbol{u}(\boldsymbol{\varphi}), \boldsymbol{\varphi})$) can be written in the following form

$$J(\boldsymbol{u}(\boldsymbol{\varphi}), \boldsymbol{\varphi}) = \frac{1}{|\Omega_1|} \int_{\Omega_1} \sigma_{xy} \, d\Omega_1 \qquad (7.13)$$

where Ω_1 is the area of interest over which the objective function is supposed to be minimized. The optimization problem can be summarized according to Eq. (4.12) while the Lagrangian objective function and derivatives are defined according to Eq. (4.13) and Eq. (4.14), respectively. Once again the optimality criteria (OC) based optimization [Zhou & Rozvany, 1991] is implemented to numerically solve Eq. (4.14). The design variables are updated by a sensitivity analysis as presented in following section.

7.4.1   Adjoint sensitivity analysis

In gradient-based methods, to solve Eq. (4.14), one should differentiate the objective and constraint functions with respect to the design variables. The procedure to obtain these derivatives is called sensitivity analysis. Generally, there are two main groups of methods for sensitivity analysis: numerical methods (e.g. finite difference) which are approximate; and analytical methods (including direct and adjoint methods) which are exact. According to [Bendsoe & Sigmund, 2003] the most efficient method for calculating derivatives involved in Eq. (4.14) is the adjoint method since there is a large number of design variables but few functions (here two, including objective function and design constraint). Recalling Eq. (4.14), the chain-rule is used to calculate the sensitivity of $J(\boldsymbol{u}(\boldsymbol{\varphi}), \boldsymbol{\varphi})$ with respect to $\boldsymbol{\varphi}$

$$\frac{dJ}{d\boldsymbol{\varphi}} = \frac{\partial J}{\partial \boldsymbol{u}} \frac{\partial \boldsymbol{u}}{\partial \boldsymbol{\varphi}} + \frac{\partial J}{\partial \boldsymbol{\varphi}} \tag{7.14}$$

From force equilibrium ($\mathbb{F} = \boldsymbol{K}\boldsymbol{u} - \boldsymbol{f} = \boldsymbol{0}$) we have

$$\frac{d\mathbb{F}}{d\boldsymbol{\varphi}} = \left(\frac{\partial \mathbb{F}}{\partial \boldsymbol{u}}\right)^T \frac{\partial \boldsymbol{u}}{\partial \boldsymbol{\varphi}} + \frac{\partial \mathbb{F}}{\partial \boldsymbol{\varphi}} = 0 \tag{7.15}$$

$$\frac{\partial \boldsymbol{u}}{\partial \boldsymbol{\varphi}} = -\left(\frac{\partial \mathbb{F}}{\partial \boldsymbol{u}}\right)^{-T} \frac{\partial \mathbb{F}}{\partial \boldsymbol{\varphi}} \tag{7.16}$$

where $(.)^T$ denotes transpose of $(.)$. Substitution of Eq. (7.16) in Eq. (7.14) yields to

$$\frac{dJ}{d\boldsymbol{\varphi}} = -\frac{\partial J}{\partial \boldsymbol{u}} \left[\left(\frac{\partial \mathbb{F}}{\partial \boldsymbol{u}}\right)^{-T} \frac{\partial \mathbb{F}}{\partial \boldsymbol{\varphi}}\right] + \frac{\partial J}{\partial \boldsymbol{\varphi}} \tag{7.17}$$

Introducing

$$\boldsymbol{\lambda} = -\frac{\partial J}{\partial \boldsymbol{u}} \left(\frac{\partial \mathbb{F}}{\partial \boldsymbol{u}}\right)^{-T} \tag{7.18}$$

and knowing that $\frac{\partial \mathbb{F}}{\partial \boldsymbol{u}} = \boldsymbol{K}$, we can write

$$\boldsymbol{K}\boldsymbol{\lambda} = -\frac{\partial J}{\partial \boldsymbol{u}} \tag{7.19}$$

Eventually Eq. (7.14) can be written in the form

$$\frac{dJ}{d\boldsymbol{\varphi}} = (\boldsymbol{\lambda})^T \frac{\partial \mathbb{F}}{\partial \boldsymbol{\varphi}} + \frac{\partial J}{\partial \boldsymbol{\varphi}} \tag{7.20}$$

The second terms of Eq. (7.20) are obtained as follows

$$\frac{\partial J}{\partial \boldsymbol{\varphi}} = \frac{1}{|\Omega_1|} \int_{\Omega_1} \frac{\partial \boldsymbol{C}_{xy}}{\partial \boldsymbol{\varphi}} \boldsymbol{Q} \boldsymbol{u} \, d\Omega_1 \tag{7.21}$$

with

$$\frac{\partial \boldsymbol{C}_{xy}}{\partial \boldsymbol{\varphi}} = -\frac{\partial \eta_p}{\partial \boldsymbol{\varphi}} \boldsymbol{C}_{mxy} + \frac{\partial \eta_p}{\partial \boldsymbol{\varphi}} \boldsymbol{C}_{cxy} \tag{7.22}$$

$\boldsymbol{C}_{mxy}$ and $\boldsymbol{C}_{cxy}$ in right hand side of Eq. (7.22) are related rows of $\boldsymbol{C}_m$ and $\boldsymbol{C}_c$ corresponding to the shear (xy) component. Considering Eq. (4.9), one can write

$$\frac{\partial \eta_p}{\partial \varphi_{i,j}} = R_{i,j}^{p,q}(\xi, \eta) \tag{7.23}$$

to complete Eq. (7.20), $\frac{\partial J}{\partial \boldsymbol{u}}$ and $\frac{\partial \mathbb{F}}{\partial \boldsymbol{\varphi}}$ are needed

$$\frac{\partial J}{\partial \boldsymbol{u}} = \frac{1}{|\Omega_1|} \int_{\Omega_1} \boldsymbol{C}_{xy} \boldsymbol{Q} \, d\Omega_1 \tag{7.24}$$

and

$$\frac{\partial \mathbb{F}}{\partial \boldsymbol{\varphi}} = \int_{\Omega} \frac{\partial \boldsymbol{K}}{\partial \boldsymbol{\varphi}} \boldsymbol{u} \, d\Omega \tag{7.25}$$

where

$$\frac{\partial \boldsymbol{K}}{\partial \boldsymbol{\varphi}} = \int_{\Omega} \boldsymbol{Q}^T \frac{\partial \boldsymbol{C}_{eq}}{\partial \boldsymbol{\varphi}} \boldsymbol{Q} \, d\Omega \tag{7.26}$$

Finally, the term $\frac{dV_f}{d\boldsymbol{\varphi}}$ can be written as

$$\frac{dV_f}{d\boldsymbol{\varphi}} = \frac{\partial V_f}{\partial \boldsymbol{\varphi}} = \int_{\Omega} \frac{\partial \eta_p}{\partial \boldsymbol{\varphi}} \, d\Omega \tag{7.27}$$

where $\frac{\partial \eta_p}{\partial \boldsymbol{\varphi}}$ can be obtained from Eq. (7.23).

7.5   Case studies

In this section, the NURBS-based finite element model is verified by performing both static and dynamic benchmark problems. Afterwards the performance of the optimization algorithm is studied.

7.5.1 Verification of the IGA model

7.5.1.1 Static analysis of a sandwich beam with a homogeneous elastic core

To demonstrate the accuracy and convergence of the IGA model, in particular with respect to the imposed discontinuity at the interface, firstly a sandwich beam is analyzed as sketched in Fig. 7.4 under 100 N/m uniform distributed load at the top of the beam. The beam is 4.8 long and 1.2 m wide and clamped at the left edge. The design parameters are listed in Table 7.1. The model is discretized by a 21×12 quadratic NURBS mesh.
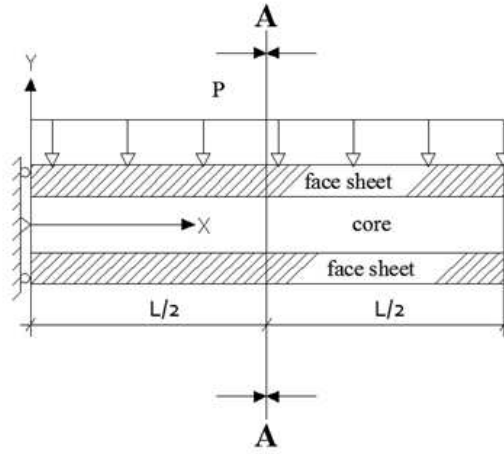
Figure 7.4: Model of the cantilever sandwich beam

Table 7.1: Design data of the sandwich beam with a homogeneous elastic core

Property	Elastic core	Face sheets
Young's Modulus E (GPa)	0.617	1.67
Poisson's ratio (v)	0.3	0.3
Thickness (CM)	0.8	0.2

Fig. 7.5 and Fig. 7.6 show the solution for the displacements and the stresses at the middle section $x = \frac{L}{2}$ (cut $A - A$ in Fig. 7.4). As can be observed from the graphs, displacements are continuous as required by the compatibility condition. The jump in σ_{xx} is properly reproduced at the interfaces as well as the slope discontinuity in shear stresses, σ_{xy}. The results agree well with the benchmark problem in [Zong et al., 2005].

Replacing the distributed load a parabolic traction at right edge of the beam, the displacement and energy norms are evaluated by

$$e_{energy} = \left[\frac{1}{2} \int_{\Omega} (\boldsymbol{\varepsilon}_{num} - \boldsymbol{\varepsilon}_{exact}) \cdot \boldsymbol{D} \cdot (\boldsymbol{\varepsilon}_{num} - \boldsymbol{\varepsilon}_{exact}) \, d\Omega \right]^{\frac{1}{2}} \qquad (7.28)$$

a)   **b)**
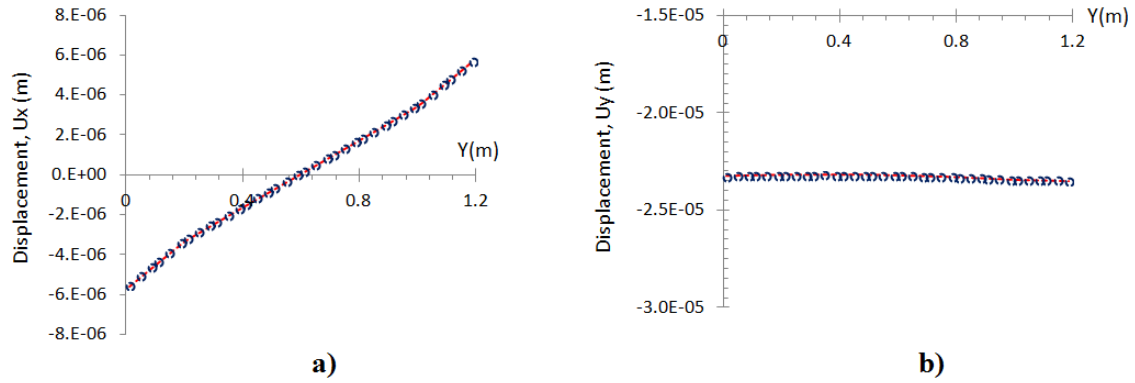
Figure 7.5: Displacements in the x (a) and y direction (b) of a sandwich cantilever beam along cut $A - A$ $(x = \frac{L}{2})$ shown in Fig. 7.4

a)   **b)**
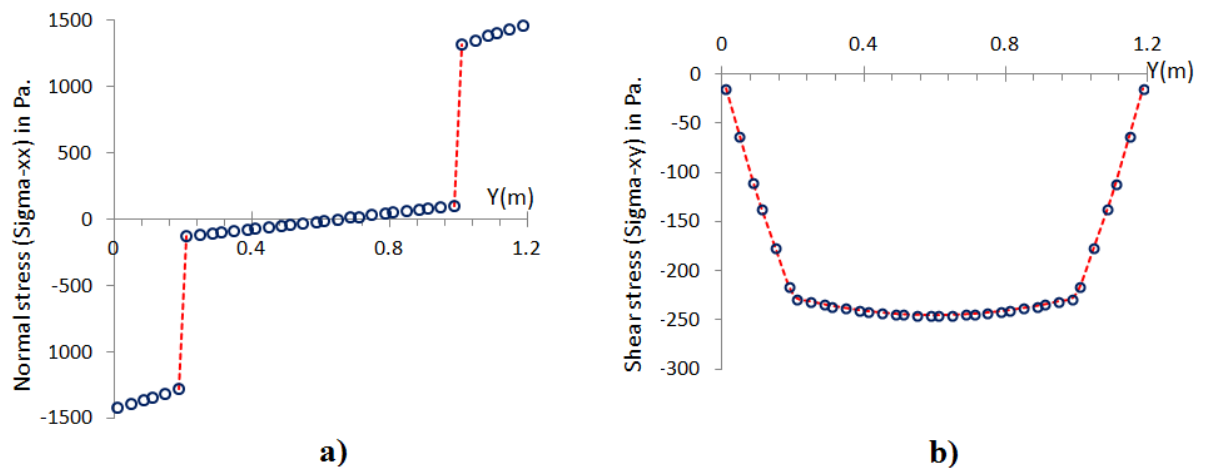
Figure 7.6: Normal stress (a) and shear stress (b) in a sandwich cantilever beam along cut $A - A$ $(x = \frac{L}{2})$ shown in Fig. 7.4

$$e_{displacement} = \left\{ \frac{\int_\Omega [(\boldsymbol{u}_{num} - \boldsymbol{u}_{exact}) \cdot (\boldsymbol{u}_{num} - \boldsymbol{u}_{exact})] \, d\Omega}{\int_\Omega [\boldsymbol{u}_{exact} \cdot \boldsymbol{u}_{exact}] \, d\Omega} \right\}^{\frac{1}{2}} \tag{7.29}$$

where $\boldsymbol{\varepsilon}$ and $\boldsymbol{u}$ are the strain and displacement vectors while the subscripts *num* and *exact* denote *numerical* and *exact*, respectively. The exact displacements as derived in [Liu *et al.*, 2012] are imposed on the entire boundary of the beam using the least squares method (see [Nguyen *et al.*, 2015]). The convergence results are shown in Fig. 7.7. The mesh parameter h is defined as the ratio between the beam height and the number of elements in the vertical direction. Using quadratic mesh, the optimal convergence rates (three for displacement norm and two for energy norm) are obtained.
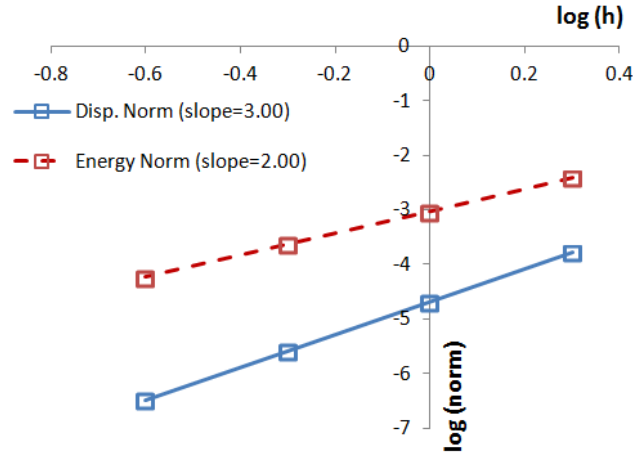
Figure 7.7: Energy and displacement norms for the sandwich cantilever beam under parabolic loading at the right edge

7.5.1.2 Free vibration of a sandwich beam with a FG core

This example includes a sandwich beam with the FG core made of Aluminum and Zirconia ($AlZrO_2$). The length of the beam is $L = 200$ *mm*, its height is $D = 20$ *mm* and the core thickness is $t_c = 14$ *mm*. Other relevant data is listed in Table 7.2. Geometry, loading and support conditions are as in Fig. 7.4.

Table 7.2: Material properties of the sandwich beam with the FG core

Property	Aluminum	Zirconia	Facesheets
Young's Modulus E (GPa)	70	151	210
Poisson's ratio (ν)	0.3	0.3	0.3
Mass density (kg/m^3)	2700	5700	7860

Table 7.3 shows the first six natural frequencies of the sandwich beam with the FG core. Results obtained by other methods [Bui *et al.*, 2013] are also presented. Using IGA with coarse meshes yields to accuracy around 0.1% comparing with reference results (fine mesh FEM using ANSYS) as presented in Table 7.3.

Table 7.3: The first six natural frequencies for a sandwich beam with FG core

Mode	Mori-Tanaka					ROM Tech.				
	t-RPIM	IGA	t-RPIM	IGA	FEM*	t-RPIM	IGA	t-RPIM	IGA	FEM*
	21×11		101×11		-	21×11		101×11		-
1	461.7	458.01	459.2	457.8	458.2	461.5	459.28	459.4	459.02	459.5
2	2729.4	2695.65	2709.2	2694.1	2697.1	2727.8	2707.1	2708.7	2705.5	2708.6
3	6443.7	6368.67	6432.9	6367.4	6374.1	6443.0	6436.0	6440.7	6434.7	6440.8
4	7105.9	6944.8	6954.7	6940.0	6950.2	7065.4	6985.8	6995.8	6981.1	6991.3
5	12651.9	12341.3	12462.2	12330	12353	12634.2	12434.5	12446.4	12423	12446.0
6	18999.3	18465.8	18594.6	18441	18483	18990.8	18630.4	18659.5	18606	18647.0

*with ANSYS

Though, the aim of this example is not to demonstrate the advantages of IGA in sandwich beam modeling, Fig. 7.8 shows smooth convergence of the NURBS results. This coarse model accuracy is beneficial for iterative design procedure and optimization especially when FE model is computationally expensive.

7.5.2 Optimization case studies

After the verification of the IGA model, the optimization of the reinforcement distribution is proceeded. Again the cantilever sandwich beam with uniformly distributed load is considered as shown in Fig. 7.4. All design parameters are summarized in Table 7.4.

Fig. 7.9 illustrates the chosen subdomains which are considered for the definition of the objective function. Areas are considered at mid span, mid height and in the vicinity of the interfaces. As mentioned before, since core shearing and debonding failure states are mostly due to shear stresses, this example concentrates on the minimization of the shear stresses. However, other components of the stresses can be also taken into account.

Table 7.4: Problem definition, cantilever sandwich beam with uniformly top load

L_x	L_y	E_m	E_c	E_f	ν	P	t_f	t_c	V_c	V_{cmax}
1.25	0.25	3.5	72.4	210	0.3	10	0.025	0.2	10%	60%

L_x, L_y, t_f, t_c : *beam length, thickness, face thk. and core thk.*(m); Vc : *total reinforc. vol.*, E_m, E_c, E_f : *Young's modulus of matrix, reinforcement and face sheet*(GPa), P : *Applied load*(KN/m); ν : *Poisson's ratio*, V_{cmax} : *the maximum nodal reinforcement*

Fig. 7.10(a) depicts the optimal layout of the reinforcement distribution in the core minimizing the shear stresses inside the area of interest #1. Fig. 7.10(b) shows the evolution of the objective function during the iterative process. The shear stress inside the nominated sub-domain, converges smoothly towards a minimum value.
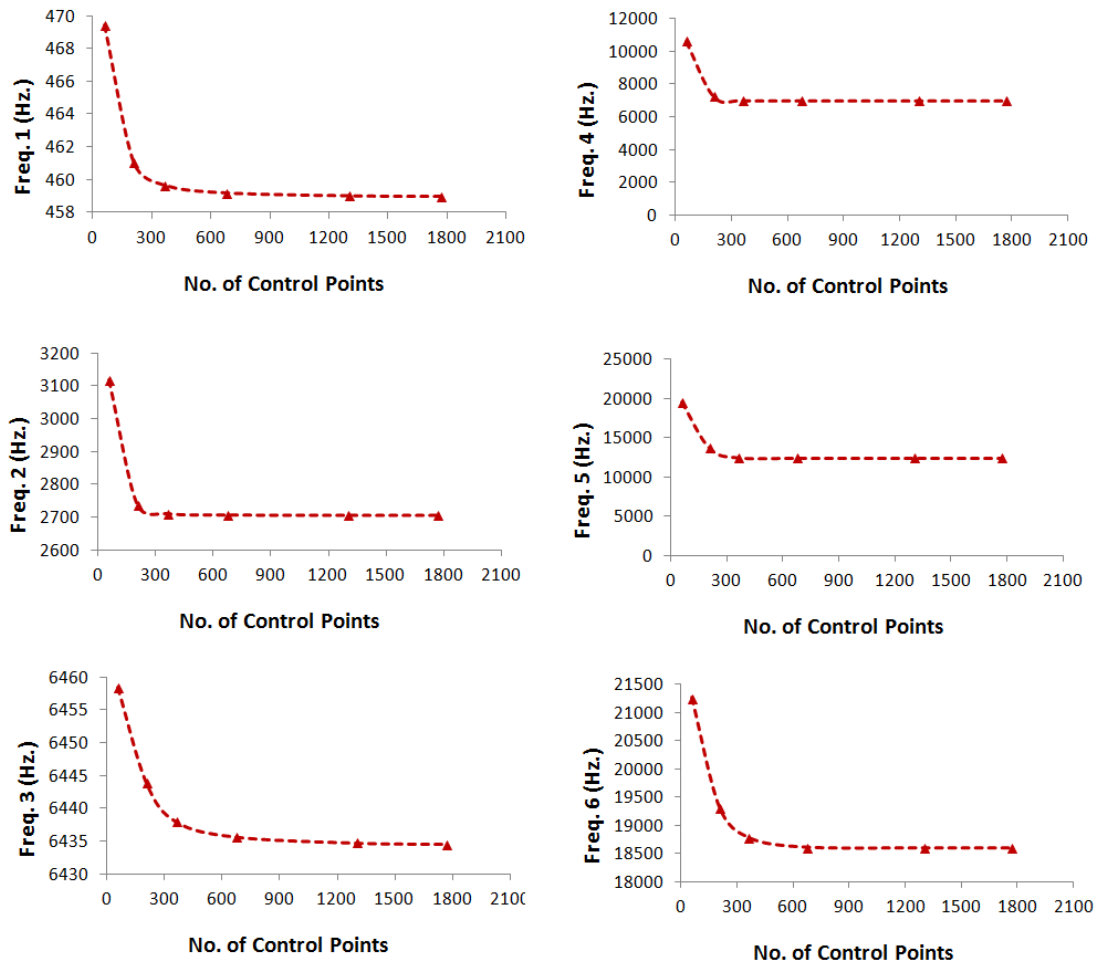
Figure 7.8: The first six natural frequencies of the sandwich beam with FG core versus number of control points of the model
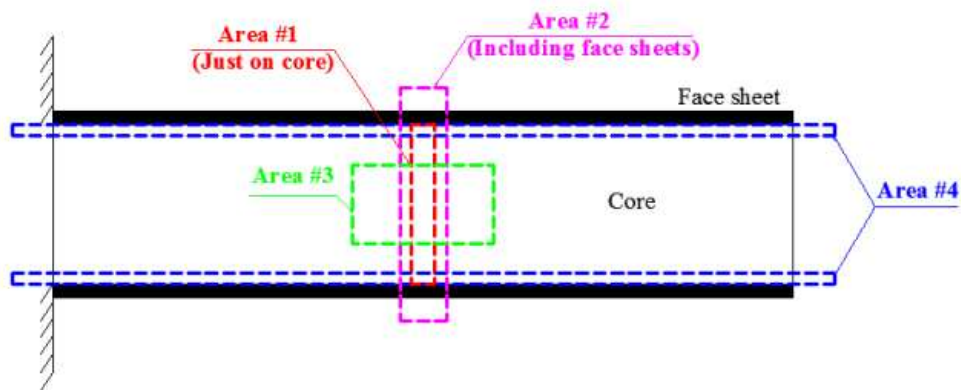
Figure 7.9: Definition of area of interest

a)

b)
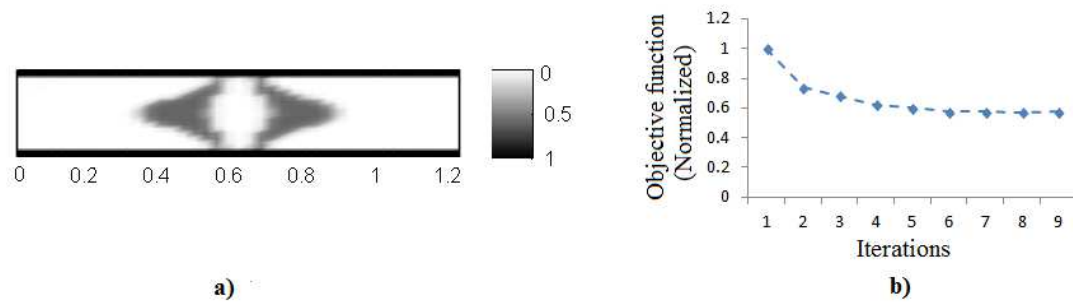
Figure 7.10: Optimal distribution of reinforcing ingredients considering area of interest #1 (a), objective function versus iterations (b)

Fig. 7.11 compares the shear stress across the thickness of the beam at mid of area #1 considering homogeneous and optimal distributions of reinforcements. The graph clearly shows that the shear stress profile improves inside the area of interest (around 50% reduction); however, for the face sheets which are outside area of interest #1(dash lines), the shear stress increases.
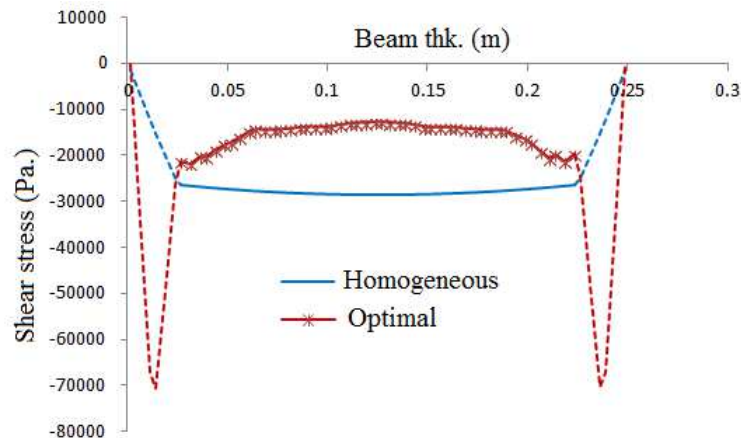
Figure 7.11: Shear stress profile for area #1 considering homogeneous and optimal distribution of reinforcements, dash lines stand for face sheets which are outside of area #1

To demonstrate the correctness of the model, area of interest #1 is extended to include face sheets. The extended area is called area of interest #2 (see Fig. 7.9). The optimal distribution of the reinforcement and the history of objective function are plotted in Fig. 7.12(a) and (b), respectively. Fig. 7.13 compares the shear stress profiles before and after optimization. As expected, the shear stresses improve within area #2.

In the next case, area of interest #3 is defined on the core of the beam and includes central elements of the core as illustrated in Fig. 7.9. The same types of results are presented in Fig. 7.14(a) and (b).

a)   b)
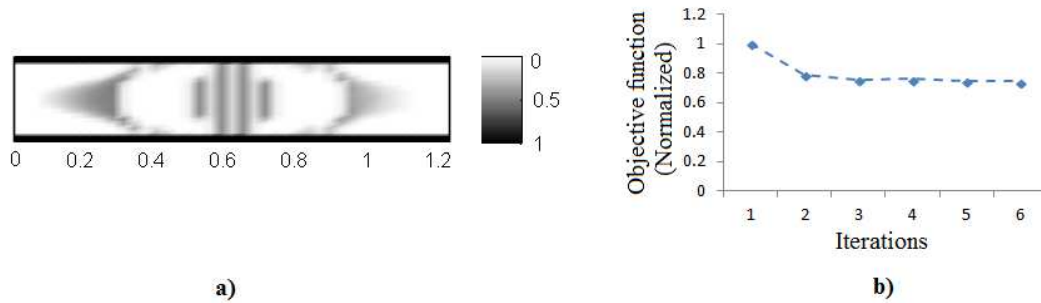
Figure 7.12: Optimal distribution of reinforcing ingredients considering area of interest #2 (a), objective function versus iterations (b)
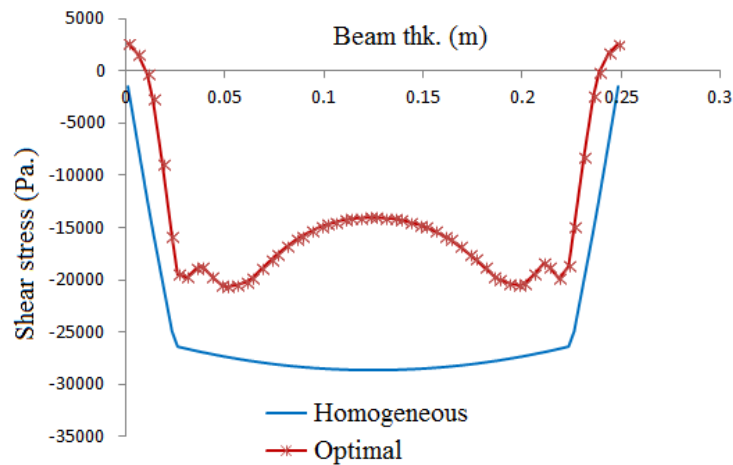
Figure 7.13: Shear stress profile for area #2 considering homogeneous and optimal distribution of reinforcements

a)   b)
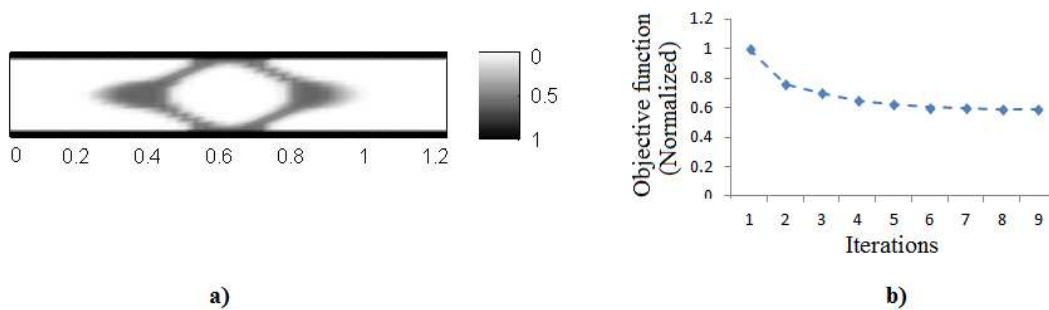
Figure 7.14: Optimal distribution of reinforcing ingredients considered area of interest #3 (a), objective function versus iterations (b)

Fig. 7.15 shows the shear stress profile before and after optimization along a section at mid width (Fig. 7.15(a)) and mid span (Fig. 7.15(b)). In both figures, dash lines refer to zones which are outside the interested area #3. Again, the graphs clearly illustrate that the shear stresses considerably decrease in the area of interest.
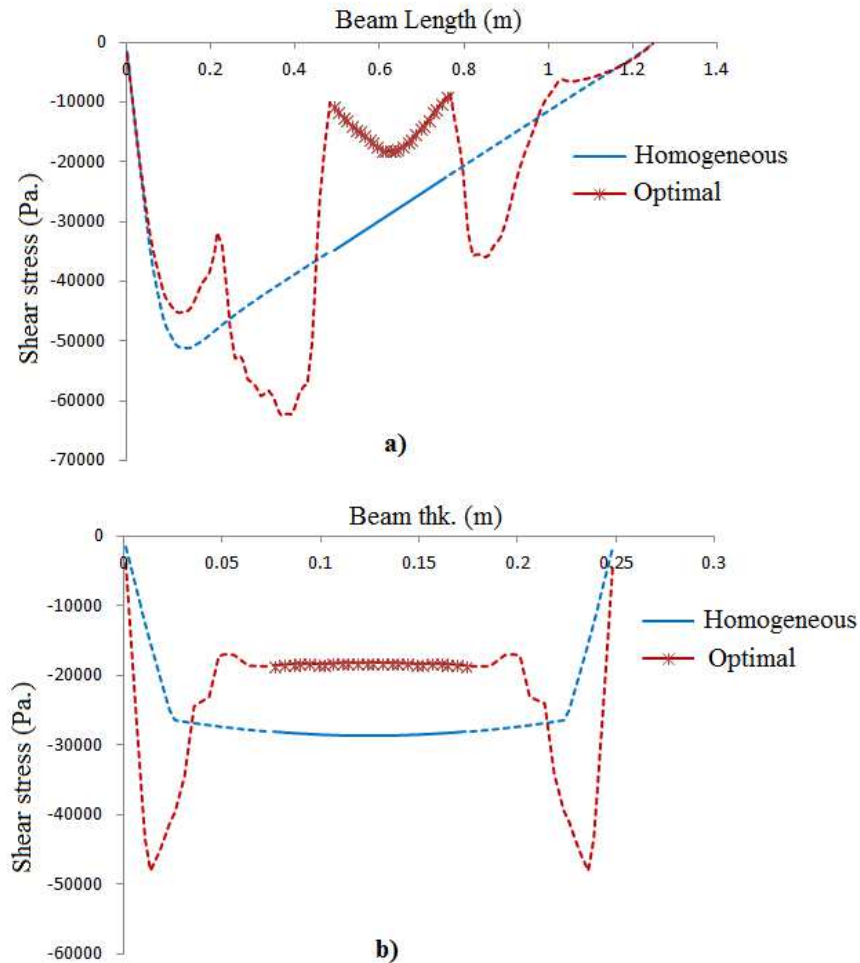
Figure 7.15: Shear stress profile for area #3 along a section at mid width (a) and mid length (b) of the beam considering homogeneous and optimal distribution of reinforcements. In both figures, dash lines refer to zones which are outside the interested area #3

As a final case, area of interest #4 is considered which includes interfacial elements in core of the beam (see Fig. 7.9). The optimal distribution of reinforcing ingredients and the history of the objective function are illustrated in Fig. 7.16(a) and (b), respectively.

Fig. 7.17 compares the shear stress at the interfacial elements of the core along the length of the beam. Fig. 7.17(a) is for the bottom interface and Fig. 7.17(b) is for the
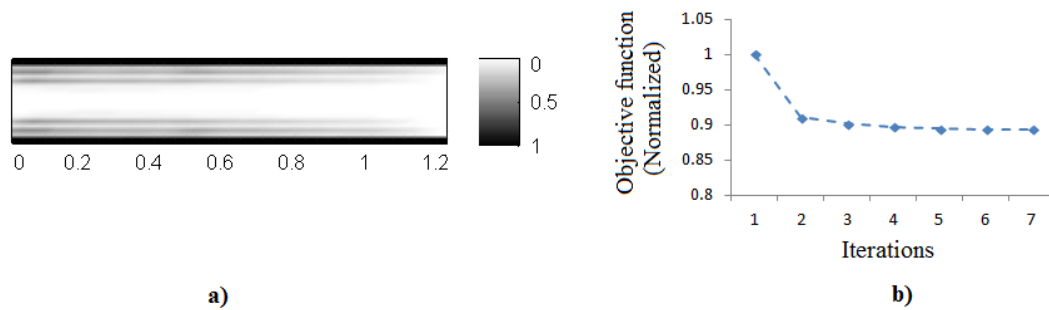
Figure 7.16: Optimal distribution of reinforcing ingredients considering area of interest #4 (a), objective function versus iterations (b)

top interface. In both graphs dashed lines show the shear stress for pure polymer (without any reinforcements). Adding 10% uniformly distributed reinforcing ingredients to the polymer matrix negligibly improves the shear stresses along the interfaces, while the same amount of reinforcements with optimal distribution, considerably reduces the interfacial shear stresses. This improvement has descending trend from the fixed left end (with the maximum shear load) to the free right end (with zero shear load).

The results in Fig. 7.17 are based on averaging shear stress inside each element. The similar results are presented in Fig. 7.18 by plotting nodal values of shear stress along longitudinal sections cutting through the area of interest #4. Fig. 7.18(a) and (b) correspond to the top and the bottom interfaces, respectively. These graphs prove that the beam with uniform FRP does not show considerable improvement in interfacial shear stress in comparison with pure polymer; while dominant improvement needs to optimal distribution of reinforcements.

7.5.3 Concluding remarks

Excessive shear stress in sandwich beams can yield to core shearing and core/face debonding. This chapter presents a computational algorithm for decreasing interfacial shear stress in sandwich beams with polymeric core. The output of the algorithm is the optimal distribution of reinforcing ingredients inside the polymer matrix. The algorithm can be also used for optimizing other stress components (i.e. peeling and bending stresses) in any arbitrary zone of the design domain. The present methodology takes advantages of NURBS basis functions for both analysis (IGA) and reinforcement distribution optimization (NURBS surface). Using IGA for model analysis, yields to high rate and smooth convergence to exact results. C^1 continuity is imposed at the interface to "truly" isolate the reinforcement distribution in the core from the face sheets using multi-patch and penalty techniques. The adjoint sensitivity technique provides flexibility in defining the area of interest over which the objective function is minimized
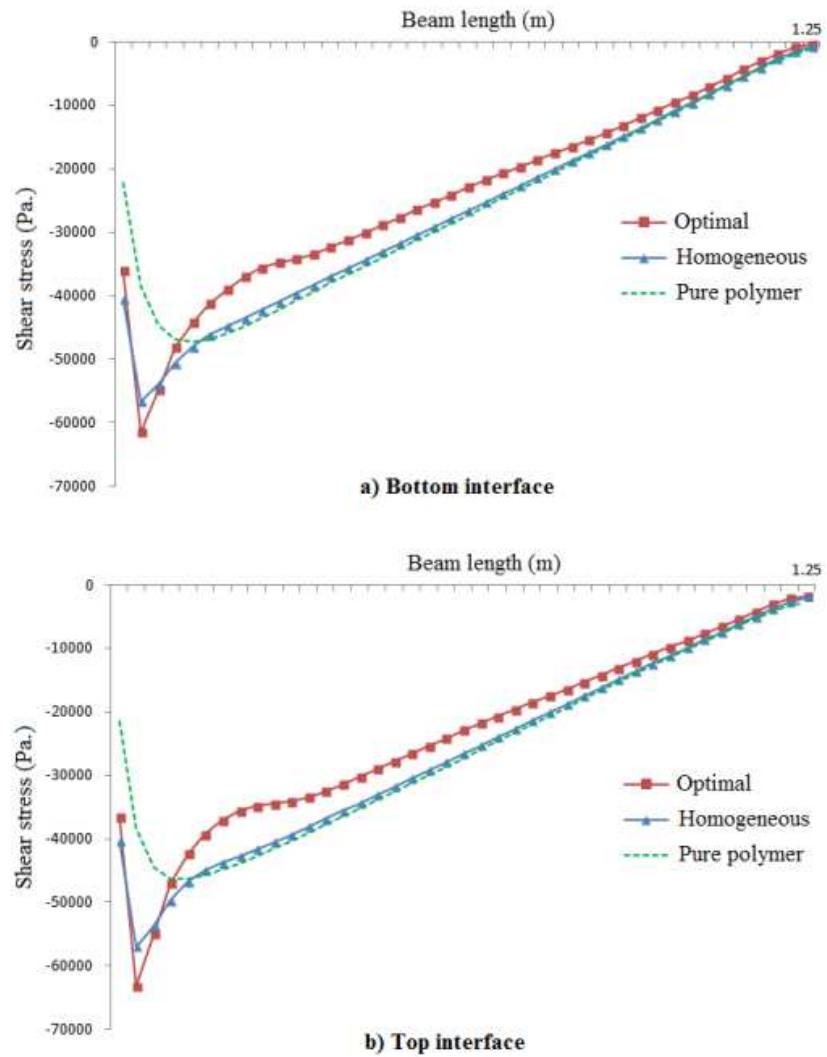
Figure 7.17: Average of shear stress in each interfacial element along the beam length considering area of interest #4 for pure polymer, homogeneous FRP and FRP with optimal distribution of reinforcements for (a) bottom interface and (b) top interface
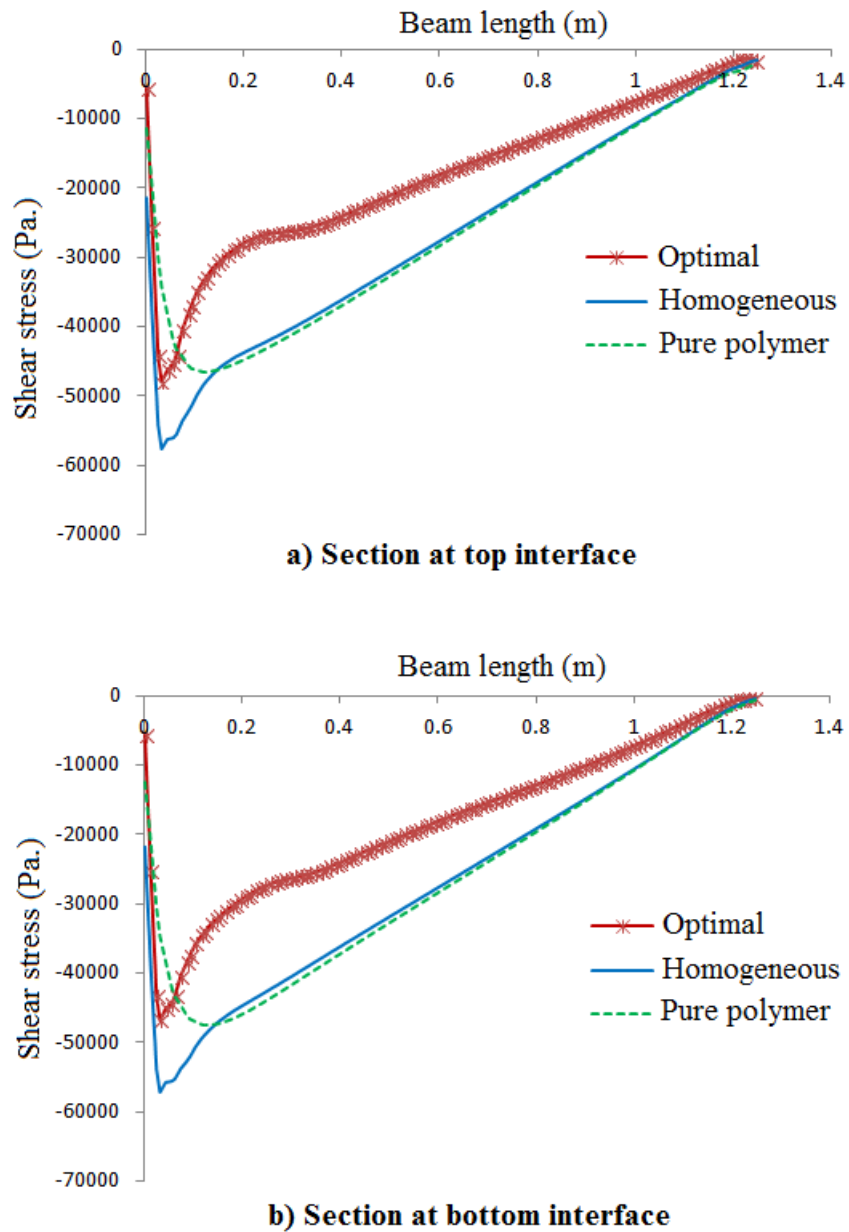
Figure 7.18: Nodal values of shear stress along a longitudinal sections at top interface (a) and bottom interface (b) in area of interest #4 comparing characteristics obtained by pure polymer, homogeneous FRP and FRP with optimal distribution of reinforcements

and also for efficient updating of the design variables through optimization iterations. Comparing the results of the case study illustrates that adding reinforcements homogeneously into polymers will slightly improve the interfacial shear stress but that considerable improvements are observed when the distribution of the reinforcement in the core is optimized.

Chapter 8

Application 2: Probabilistic multiconstraints optimization of cooling channels in ceramic matrix composites

8.1 Introduction

The main disadvantage of monolithic ceramics is their low fracture toughness. Thus, carbon fibers are added to increase their damage tolerance while maintaining other advantages (for instance lower density and higher maximum operating temperature compared to metals or high erosion and corrosion resistance).

As a common reinforcing ingredient, Carbon fibers (C-fibers) degrade in an oxidizing atmosphere beyond 450 degrees Celsius [Krenkel, 2005]. Although multilayer protection coatings hinder degradation to a degree, the coating process may itself result in formation of interphasial cracks. Preventing high temperature zones in the component might be a better solution. Such a solution however calls for a multidisciplinary approach accounting for material selection, coating and internal cooling design.

This chapter presents a computational framework for an efficient and reliable internal cooling network for a typical component made of Ceramic Matrix Composite (CMC). Although some attempts to optimize internal cooling system of a monotonic metallic turbine blade exist, the currently known approaches are limited to using heuristic optimization methods, particularly Genetic Algorithm (GA) which is computationally expensive. For example, Dennis *et al.*, 2003 used parallel genetic algorithm to optimize locations and discrete radii of a large number of small circular cross-section coolant passages. Nagaiah & Geiger, 2014 used NSGA-II as a multiobjective evolutionary algorithm optimizing the rib design inside a 2D cooling channel of a gas tur-

bine blade. In both works an external commercial finite element package is used for the thermal analysis.

Regardless of the optimization technique, another major drawback of current methods is their deterministic nature. Actual characteristics of a composite material (including CMC) involve many uncertainties. These emanate from a variety of sources such as constituent material properties, manufacturing and process imperfections, loading conditions and geometry (a classification is presented in chapter 5. Neglecting the role of uncertainties in composite materials might result in either unsafe or unnecessary conservative design. This chapter focuses not only on optimal but also on reliable design of a typical internal cooling network within a CMC using a non-heuristic method and accounting for uncertainties.

The double stage sequential optimization approach (see Chapter 6) is implemented. In the first stage, it is assumed that C-fibers are uniformly distributed in the ceramic matrix. Then by using RBDO, the outputs of the first stage which are optimal capacities of the cooling channels, are exported into the next stage. In the second stage, the optimizer takes these inputs and uses the adjoint sensitivity technique adopted for the coupled elastic and thermal fields and eventually provides an optimal distribution of the C-fibers within the design domain in order to enhance the target reliability of the component.

8.2 Thermoelastic formulation

The steady-state governing equation and boundary conditions for a temperature field in a 2D isotropic solid with domain Ω and boundary Γ are [Wu *et al.*, 2009]

$$\left(k_{ij}\theta_{,j}\right)_{,i} + Q = 0 \quad in\ \Omega \tag{8.1}$$

$$\theta = \theta_\Gamma \quad on\ \Gamma_1\ Essential\ boundary \tag{8.2}$$

$$-n_i k_{ij}\theta_{,j} = q_\Gamma \quad on\ \Gamma_2\ Heat\ flux\ boundary \tag{8.3}$$

$$-n_i k_{ij}\theta_{,j} = h(\theta - \theta_\infty) \quad on\ \Gamma_3\ Convection\ boundary \tag{8.4}$$

$$-n_i k_{ij}\theta_{,j} = 0 \quad on\ \Gamma_4\ Adiabatic\ boundary \tag{8.5}$$

where k_{ij}, Q, and θ denote the thermal conductivity, internal uniform heat source and temperature field, respectively; n_i is component of the unit outward normal to the boundary, h is the heat convection coefficient, q_Γ is the prescribed heat flux and θ_∞

is the temperature of the surrounding medium in convection process. The governing equation and boundary conditions for a linear elastic solid are given by

$$\sigma_{ij,j} + b_i = 0 \quad in \ \Omega \tag{8.6}$$

$$u_i = u_\Gamma \quad on \ \Gamma_u \ Essential \ boundary \tag{8.7}$$

$$\sigma_{ij} n_i = t_\Gamma \quad on \ \Gamma_t \ Heat \ flux \ boundary \tag{8.8}$$

where σ and b denote the stress and body force. u_Γ and t_Γ are the given displacement and traction on the essential and natural boundaries, respectively.

The heat and elastic problems are linked by the following stress, strain and thermal expansion relation

$$\sigma_{ij} = \delta_{ij} \lambda_L \varepsilon_{kk} + 2\mu_L \varepsilon_{ij} - \delta_{ij}(3\lambda_L + 2\mu_L)\alpha\Delta\theta \tag{8.9}$$

where λ_L and μ_L are Lamé constants, α is the thermal expansion coefficient and $\Delta\theta$ is the temperature change with respect to the reference temperature which is assumed zero here.

A weighted residual weak form of the boundary value problem (Eq. (8.1)- (8.5)) can be written as a generalized functional I

$$I(\theta) = \int_\Omega w \left[(k_{ij} \ \theta_{,j})_{,i} + Q \right] d\Omega = 0 \tag{8.10}$$

where w denotes the sufficiently differentiable test function. Differentiation by parts and using Green's theorem, the functional $I(\theta)$ can be written as

$$I(\theta) = \int_\Omega \frac{1}{2} \left[k_{x_1} \left(\frac{\partial\theta}{\partial x_1} \right)^2 + k_{x_2} \left(\frac{\partial\theta}{\partial x_2} \right)^2 \right] d\Omega - \int_\Omega \theta Q d\Omega + \int_{\Gamma_2} \theta q_\Gamma d\Gamma +$$
$$\int_{\Gamma_3} h\theta \left(\frac{1}{2}\theta - \theta_\infty \right) d\Gamma = 0 \tag{8.11}$$

considering δ as the variational operator, the Bubnov-Galerkin weak form for the heat transfer problem can be obtained as follows

$$\int_\Omega \delta(\nabla\boldsymbol{\theta})^T \boldsymbol{K}_c \nabla\boldsymbol{\theta} d\Omega - \int_\Omega \delta\boldsymbol{\theta}^T Q d\Omega + \int_{\Gamma_2} \delta\boldsymbol{\theta}^T q_\Gamma d\Gamma + \int_{\Gamma_3} \delta\boldsymbol{\theta}^T h\boldsymbol{\theta} d\Gamma -$$
$$\int_{\Gamma_3} \delta\boldsymbol{\theta}^T h\theta_\infty d\Gamma = 0 \tag{8.12}$$

The strains arising from boundary loadings and body forces induce only small temperature changes which can be ignored in the analysis. Thus, the semi-coupled theory

of thermoelasticity is employed here. The heat governing equations are firstly solved to obtain the temperature field. Then, the body forces induced by the temperature field are used along with the other applied forces to calculate the final response of the elastic body. Using the Bubnov-Galerkin weak form

$$\int_{\Omega} \delta(\boldsymbol{\varepsilon}(\boldsymbol{u}) - \boldsymbol{\varepsilon}_{\theta}(\boldsymbol{u}))^{T} \boldsymbol{C}(\boldsymbol{\varepsilon}(\boldsymbol{u}) - \boldsymbol{\varepsilon}_{\theta}(\boldsymbol{u})) d\Omega - \int_{\Gamma_{t}} \delta \boldsymbol{u}^{T} t_{\Gamma} d\Gamma - \int_{\Omega} \delta \boldsymbol{u}^{T} \boldsymbol{b} d\Omega = 0 \quad (8.13)$$

B-spline basis functions are selected as the test function w. They are also employed to approximate the displacement and temperature fields

$$u(x,y) = \sum_{i=1}^{n} \sum_{j=1}^{m} N_{i,j}^{p,q}(\xi, \eta) u_{i,j} = \boldsymbol{N} \boldsymbol{u} \quad (8.14)$$

$$\theta(x,y) = \sum_{i=1}^{n} \sum_{j=1}^{m} N_{i,j}^{p,q}(\xi, \eta) \theta_{i,j} = \boldsymbol{N}\boldsymbol{\theta} \quad (8.15)$$

where $\boldsymbol{u}$ and $\boldsymbol{\theta}$ denotes the vector of nodal displacements and temperatures, respectively. The strain-displacement and the heat flux-temperature gradient relationships can be written as:

$$\boldsymbol{\varepsilon} = \boldsymbol{B}_{e}\boldsymbol{u} \quad and \quad \boldsymbol{g} = \boldsymbol{B}_{heat}\boldsymbol{\theta} \quad (8.16)$$

$\boldsymbol{B}_{e}$ and $\boldsymbol{B}_{heat}$ are the matrices containing the derivatives of the shape functions, $\boldsymbol{N}$, corresponding to the elastic and thermal problems, respectively.

By substituting the B-spline approximation function into Eq. (8.12), the discretized system of equations can be expressed in the following matrix form

$$\boldsymbol{K}_{c}\boldsymbol{\theta} = \boldsymbol{f}_{heat} \quad (8.17)$$

The local conduction matrix, $\boldsymbol{K}_{c}$, and the heat force vector, $\boldsymbol{f}_{heat}$, are determined according to

$$\boldsymbol{K}_{c} = \int_{\Omega} \boldsymbol{B}_{heat}^{T} \boldsymbol{H} \boldsymbol{B}_{heat} d\Omega + \int_{\Gamma_{3}} h\boldsymbol{N}^{T}\boldsymbol{N}d\Gamma_{3} \quad (8.18)$$

$$\boldsymbol{f}_{heat} = \boldsymbol{f}_{Q} + \boldsymbol{f}_{h} + \boldsymbol{f}_{q} \quad (8.19)$$

where

$$\boldsymbol{f}_{Q} = \int_{\Omega} \boldsymbol{N}^{T} Q d\Omega \quad (8.20)$$

$$\boldsymbol{f}_{h} = \int_{\Gamma_{3}} \boldsymbol{N}^{T} h\theta_{\infty} d\Gamma_{3} \quad (8.21)$$

$$\boldsymbol{f}_{q} = -\int_{\Gamma_{2}} \boldsymbol{N}^{T} q_{\Gamma} d\Gamma_{2} \quad (8.22)$$

Superscript T is used in this chapter to denote transpose of a matrix; H is the heat conduction matrix. The first and the second integrals in Eq. (8.18) correspond to the heat conduction (in volume Ω) and the convection (on surface Γ_3). The heat force vector contains $\boldsymbol{f}_Q, \boldsymbol{f}_h$ and $\boldsymbol{f}_q$ induced by the uniform heat source Q, the heat convection and heat flux q_Γ, respectively. Substituting the test function and its derivatives into Eq. (8.13) leads finally the discretized linear system of equations for the thermoelasticity problem in the following matrix form

$$\boldsymbol{Ku} = \boldsymbol{f}_{total} \tag{8.23}$$

The global stiffness matrix of the elastic problem, $\boldsymbol{K}$, is obtained by

$$\boldsymbol{K} = \int_\Omega \boldsymbol{B}_e^T \boldsymbol{C} \boldsymbol{B}_e \ d\Omega \tag{8.24}$$

while

$$\boldsymbol{f}_{total} = \boldsymbol{f}_m + \boldsymbol{f}_\theta \tag{8.25}$$

where $\boldsymbol{f}_m$ is the force vector corresponding to mechanical loading

$$\boldsymbol{f}_m = \int_{\Gamma_t} \boldsymbol{N}^T \boldsymbol{t}_\Gamma d\Gamma + \int_\Omega \boldsymbol{N}^T \boldsymbol{b} d\Omega \tag{8.26}$$

The body forces induced by the temperature field, $\boldsymbol{f}_\theta$, are also calculated using the following equation

$$\boldsymbol{f}_\theta = \int_\Omega \boldsymbol{B}_e^T \boldsymbol{C} \boldsymbol{\varepsilon}_\theta d\Omega \tag{8.27}$$

where $\boldsymbol{C}$ is the elasticity matrix and $\boldsymbol{\varepsilon}_\theta$ is the thermal strain matrix which for the case of plane stress with an isotropic material is obtained by

$$\boldsymbol{\varepsilon}_\theta = \left\{ \begin{array}{c} \alpha\Delta\theta \\ \alpha\Delta\theta \\ 0 \end{array} \right\} \tag{8.28}$$

It is also noteworthy to declare that, in this work the cross section area of a typical cooling channel is assumed much smaller than the area of the design domain. Such a cooling source which exists within a small area only, may be idealized as a point heat sink. This point sink is modeled by simply including a node at the location of the point source in the discretized model [Logan, 2007]. In the two dimensional element, for a typical cooling source, Q_i, located at $x = x_0$ and $y = y_0$ one can write

$$\boldsymbol{f}_{Q_i} = \boldsymbol{N}_0^T Q_i \tag{8.29}$$

where $\boldsymbol{N}_0$ is the vector of shape functions evaluated at $x = x_0$ and $y = y_0$.

8.3 Reliability based design

8.3.1 Deterministic design versus reliability based design

Traditional factor of safety would provide a safety margin to cover uncertainties in loads, material parameters and in the model. This factor is in principle deterministic but its magnitude is usually obtained based on experience which may include stochastic data. There are two major concerns related to this concept of safety: 1) conservatism and 2) inability to reflect differing degrees of control on design variables [Nikolaidis *et al.*, 2005]. Both of these issues might lead to costly suboptimal designs.

New market demands along with shortcomings of traditional deterministic design approaches led to the development of nondeterministic approaches. One approach uses probability theory for capturing the uncertainties and measuring the reliability of the system. In probabilistic analysis, design variables and parameters are assumed to be random variables with selected joint probability density functions (pdf).

8.3.2 Probabilistic multiconstraints

In this chapter the probabilistic thermal and elastic design limit states are considered as a series constraints. It means that violation of at least one constraint yields to the entire system failure. As is shown in Fig. 8.1, the failure region is the union of two failure subsets corresponding to each limit state. In mathematical form the failure domain D with two limit state functions $g_i(x)$ where $i = 1, 2$ can be expressed as $D = \{x | \bigcup_i g_i(x) \le 0\}$.
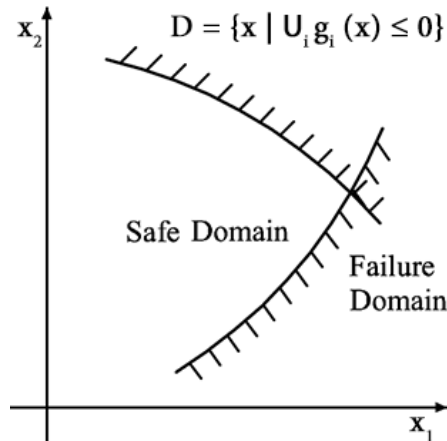
Figure 8.1: Schematic illustration of the failure domain with two probabilistic design constraints

The system failure probability can be obtained by $P_f = 1 - \Phi_m(B, R)$ where $\Phi_m(B, R)$ is the m-variant standard normal CDF with $B = \{\beta_1, ..., \beta_m\}$ and $R = \rho_{KL}$; $\rho_{KL} = \alpha_k \alpha_1^T$

where α_k is the unit normal to the hyperplane obtained by FORM approximation [Nikolaidis *et al.*, 2005]. The open source software FERUM 4.1 [Bourinet, 2010] has been extended to perform the reliability analysis for multiconstraints problems.

8.3.3 RBDO

RBDO deals with obtaining optimal design with low failure probability. A double-loop (nested) algorithm is employed where the outer loop finds the optimal values for the design variables and the inner loop performs the reliability analysis. Here, the RBDO is performed as the first stage of the optimization process. The first objective function is minimizing the total required cooling capacity of the heat sinks. The probabilistic constraints are defined on maximum deflection and maximum temperature of the component as the series constraints. Thus, the first stage of the optimization problem can be summarized as follows

$$
\begin{cases}
Minimize: \ C(\boldsymbol{Q}) = \sum_{i=0}^{n} Q_i \quad \text{where } n = number\ of\ cooling\ channels \\
subjected\ to: \\
Probabilistic\ Constraints\ : \begin{cases} P_{f,1} = Prob(\theta_{allow} - \theta_{max} < 0) \leq \bar{P}_f \\ \\ P_{f,2} = Prob\,(\delta_{all} - \delta_{max} < 0) \leq \bar{P}_f \end{cases} \\ \\
Deterministic\ Constraints\ : Q_j^L \leq Q_j \leq Q_j^U \quad \text{where } j \in \{1,2,\ldots,n\}
\end{cases}
\tag{8.30}
$$

where θ_{allow} and δ_{all} are the maximum allowable temperature and deflection, respectively. These two parameters as well as the prescribed failure probabilities (i.e. $\bar{P}_f$) should be decided by the designer at the beginning of the optimization process. Q_j denotes the cooling capacity of the jth channel; θ_{max} and δ_{max} are the corresponding maximum values obtained from the solution of the thermoelastic governing equations described in Section 8.2.

8.4 Adopting the double sequential stages optimization methodology

The optimization algorithm for this application includes two independent but sequentially linked stages. In the first stage, it is assumed that the C-fibers are uniformly distributed in the matrix. According to Eq. (8.30), the total required cooling capacity of the channels is optimized through the RBDO approach. Mechanical (maximum deflection) as well as thermal (maximum temperature) probabilistic design constraints are enforced. The deterministic design constraints also limit the capacities of the cooling channels. Random variables include constituent material properties (Young's modulus

and heat conduction coefficient for the both C-fibers and ceramic matrix), applied load, applied heat flux and film convection coefficient. The output of this stage is used as the input for the second stage.

$\varphi_{i,j}$ are the only design variables in the second optimization stage which are defined on the mesh control points. When the reinforcement volume fraction at each point is available (Eq. (4.9)), the equivalent properties are defined as follows

$$M_{eq}(x,y) = \left(1 - \eta_p\right) M_m + \eta_p M_c \quad with \quad M = E, k, \alpha \tag{8.31}$$

where, E, k and α denote the Young's modulus, thermal conductivity and thermal expansion coefficient, respectively. Subscripts eq, m and c represent homogenized, matrix and C-fibers respectively. For the sake of notation simplicity, M_{eq} is denoted by M in the following. The multiobjective optimization problem is defined as the weighted sum of different normalized objective functions. The target (total) objective function, $J(\boldsymbol{u}(\boldsymbol{\varphi}), \boldsymbol{\theta}(\boldsymbol{\varphi}), \boldsymbol{\varphi})$, consists of the structural compliance and the so called "thermal compliance" yielding

$$J(\boldsymbol{u}(\boldsymbol{\varphi}), \boldsymbol{\theta}(\boldsymbol{\varphi}), \boldsymbol{\varphi}) = \frac{W_1}{S_1} \left(\frac{1}{2} \int_{\Omega} (\boldsymbol{B}_e \boldsymbol{u})^T \boldsymbol{C} (\boldsymbol{B}_e \boldsymbol{u}) \, d\Omega \right) + \frac{W_2}{S_2} \left(\frac{1}{2} \int_{\Omega} (\boldsymbol{B}_{heat} \boldsymbol{\theta})^T \boldsymbol{H} (\boldsymbol{B}_{heat} \boldsymbol{\theta}) \, d\Omega \right) \tag{8.32}$$

where $\boldsymbol{\varphi}$ denotes the vector containing all $\varphi_{(i,j)}$ and Ω is the entire design domain; W_i and S_i denote the ith weight and scaling factor, respectively. The optimization problem in the second stage can then be summarized as follows

$$\begin{cases} Minimize : J(\boldsymbol{u}(\boldsymbol{\varphi}), \boldsymbol{\theta}(\boldsymbol{\varphi}), \boldsymbol{\varphi}) \\ Subjected \; to : \\ \\ V_f = \int_{\Omega} \eta_p \, d\Omega = V_{f0} \\ \mathbb{F}_1(\boldsymbol{\theta}(\boldsymbol{\varphi}), \boldsymbol{\varphi}) = \boldsymbol{K}_c \boldsymbol{\theta} - \boldsymbol{f}_{heat} = 0 \\ \mathbb{F}_2(\boldsymbol{u}(\boldsymbol{\varphi}), \boldsymbol{\theta}(\boldsymbol{\varphi}), \boldsymbol{\varphi}) = \boldsymbol{K}\boldsymbol{u} - \boldsymbol{f}_m - \boldsymbol{f}_\theta = 0 \\ \varphi_{i,j} - 1 \leq 0 \\ -\varphi_{i,j} \leq 0 \end{cases} \tag{8.33}$$

where V_f is the total C-fibers volume in each optimization iteration, V_{f0} is an arbitrary initial C-fibers volume which must be set at the beginning of the optimization process.

8.4.1 Adjoint sensitivity analysis

By using the chain-rule one can calculate the sensitivity of the objective function, $J(\boldsymbol{u}(\boldsymbol{\varphi}), \boldsymbol{\theta}(\boldsymbol{\varphi}), \boldsymbol{\varphi})$, with respect to $\boldsymbol{\varphi}$

$$\frac{dJ}{d\boldsymbol{\varphi}} = \frac{\partial J}{\partial \boldsymbol{u}} \frac{\partial \boldsymbol{u}}{\partial \boldsymbol{\varphi}} + \frac{\partial J}{\partial \boldsymbol{\theta}} \frac{\partial \boldsymbol{\theta}}{\partial \boldsymbol{\varphi}} + \frac{\partial J}{\partial \boldsymbol{\varphi}} \tag{8.34}$$

The last term of Eq. (8.34) is the explicit quantity and easy to calculate

$$
\frac{\partial J}{\partial \boldsymbol{\varphi}} = \frac{W_1}{S_1} \left(\frac{1}{2} \int_{\Omega} (\boldsymbol{B}_e \boldsymbol{u})^T \frac{\partial \boldsymbol{C}}{\partial \boldsymbol{\varphi}} (\boldsymbol{B}_e \boldsymbol{u}) \, d\Omega \right) +
$$
$$
\frac{W_2}{S_2} \left(\frac{1}{2} \int_{\Omega} (\boldsymbol{B}_{heat} \boldsymbol{\theta})^T \frac{\partial \boldsymbol{H}}{\partial \boldsymbol{\varphi}} (\boldsymbol{B}_{heat} \boldsymbol{\theta}) \, d\Omega \right)
$$
(8.35)

while

$$
\frac{\partial \boldsymbol{C}}{\partial \boldsymbol{\varphi}} = - \frac{\partial \eta_p}{\partial \boldsymbol{\varphi}} \left(\frac{E_m}{1 - v^2} \right) \begin{bmatrix} 1 & v & 0 \\ v & 1 & 0 \\ 0 & 0 & \left(\frac{1-v}{2} \right) \end{bmatrix} + \frac{\partial \eta_p}{\partial \boldsymbol{\varphi}} \left(\frac{E_c}{1 - v^2} \right) \begin{bmatrix} 1 & v & 0 \\ v & 1 & 0 \\ 0 & 0 & \left(\frac{1-v}{2} \right) \end{bmatrix}
$$
(8.36)

and

$$
\frac{\partial \boldsymbol{H}}{\partial \boldsymbol{\varphi}} = - \frac{\partial \eta_p}{\partial \boldsymbol{\varphi}} \begin{bmatrix} k_m & 0 \\ 0 & k_m \end{bmatrix} + \frac{\partial \eta_p}{\partial \boldsymbol{\varphi}} \begin{bmatrix} k_c & 0 \\ 0 & k_c \end{bmatrix}
$$
(8.37)

Moreover

$$
\frac{\partial \eta_p}{\partial \varphi_{i,j}} = N_{i,j}^{p,q} (\xi, \eta)
$$
(8.38)

The first and the second terms of Eq. (8.34) include implicit quantities (i.e. $\frac{\partial \boldsymbol{u}}{\partial \boldsymbol{\varphi}}$ and $\frac{\partial \boldsymbol{\theta}}{\partial \boldsymbol{\varphi}}$) which are accomplished by using the heat conduction and linear elasticity force equilibrium equations (see $\mathbb{F}_1$ and $\mathbb{F}_2$ in Eq. (8.33)) as adjoint equations.

By differentiating, we have

$$
\left(\frac{\partial \mathbb{F}_1}{\partial \boldsymbol{\theta}} \right)^T \frac{\partial \boldsymbol{\theta}}{\partial \boldsymbol{\varphi}} + \frac{\partial \mathbb{F}_1}{\partial \boldsymbol{\varphi}} = \boldsymbol{0}
$$
(8.39)

$$
\frac{\partial \boldsymbol{\theta}}{\partial \boldsymbol{\varphi}} = - \left(\frac{\partial \mathbb{F}_1}{\partial \boldsymbol{\theta}} \right)^{-T} \frac{\partial \mathbb{F}_1}{\partial \boldsymbol{\varphi}}
$$
(8.40)

Substitution Eq. (8.40) into the second term of Eq. (8.34) yields

$$
\frac{\partial J}{\partial \boldsymbol{\theta}} \frac{\partial \boldsymbol{\theta}}{\partial \boldsymbol{\varphi}} = - \frac{\partial J}{\partial \boldsymbol{\theta}} \left[\left(\frac{\partial \mathbb{F}_1}{\partial \boldsymbol{\theta}} \right)^{-T} \frac{\partial \mathbb{F}_1}{\partial \boldsymbol{\varphi}} \right]
$$
(8.41)

Assuming

$$
\boldsymbol{\gamma} = - \frac{\partial J}{\partial \boldsymbol{\theta}} \left(\frac{\partial \mathbb{F}_1}{\partial \boldsymbol{\theta}} \right)^{-T}
$$
(8.42)

and knowing that $\frac{\partial \mathbb{F}_1}{\partial \boldsymbol{\theta}} = \boldsymbol{K}_c$, we can write

$$
\boldsymbol{K}_c \boldsymbol{\gamma} = - \frac{\partial J}{\partial \boldsymbol{\theta}}
$$
(8.43)

$$K_c \gamma = -\frac{W_2}{S_2} \int_\Omega B_{heat}{}^T H B_{heat} \, \theta \, d\Omega \tag{8.44}$$

Eventually, Eq. (8.41) can be written in the form

$$\frac{\partial J}{\partial \theta} \frac{\partial \theta}{\partial \varphi} = (\gamma)^T \frac{\partial \mathbb{F}_1}{\partial \varphi} \tag{8.45}$$

$$\frac{\partial J}{\partial \theta} \frac{\partial \theta}{\partial \varphi} = \int_\Omega (B_{heat} \, \gamma)^T \frac{\partial H}{\partial \varphi} (B_{heat} \, \theta) \, d\Omega \tag{8.46}$$

Analogously, to calculate the first term of Eq. (8.34) one can differentiate $\mathbb{F}_2$ as

$$\left(\frac{\partial \mathbb{F}_2}{\partial u}\right)^T \frac{\partial u}{\partial \varphi} + \left(\frac{\partial \mathbb{F}_2}{\partial \theta}\right)^T \frac{\partial \theta}{\partial \varphi} + \frac{\partial \mathbb{F}_2}{\partial \varphi} = 0 \tag{8.47}$$

$$\frac{\partial u}{\partial \varphi} = \left(\frac{-\partial \mathbb{F}_2}{\partial u}\right)^{-T} \left[\left(\frac{\partial \mathbb{F}_2}{\partial \theta}\right)^T \frac{\partial \theta}{\partial \varphi} + \frac{\partial \mathbb{F}_2}{\partial \varphi}\right] \tag{8.48}$$

Substitution Eq. (8.40) into Eq. (8.48) gives

$$\frac{\partial u}{\partial \varphi} = \left(\frac{-\partial \mathbb{F}_2}{\partial u}\right)^{-T} \left[\left(\frac{\partial \mathbb{F}_2}{\partial \theta}\right)^T \left(-\left(\frac{\partial \mathbb{F}_1}{\partial \theta}\right)^{-T} \frac{\partial \mathbb{F}_1}{\partial \varphi}\right) + \frac{\partial \mathbb{F}_2}{\partial \varphi}\right] \tag{8.49}$$

The first term of Eq. (8.34) then becomes

$$\frac{\partial J}{\partial u} \frac{\partial u}{\partial \varphi} = \frac{\partial J}{\partial u} \left[\left(\frac{-\partial \mathbb{F}_2}{\partial u}\right)^{-T} \left[\left(\frac{\partial \mathbb{F}_2}{\partial \theta}\right)^T \left(-\left(\frac{\partial \mathbb{F}_1}{\partial \theta}\right)^{-T} \frac{\partial \mathbb{F}_1}{\partial \varphi}\right) + \frac{\partial \mathbb{F}_2}{\partial \varphi}\right]\right] \tag{8.50}$$

Manipulating Eq. (8.50) yields

$$\frac{\partial J}{\partial u} \frac{\partial u}{\partial \varphi} = \frac{\partial J}{\partial u} \left(\frac{-\partial \mathbb{F}_2}{\partial u}\right)^{-T} \left[\left(\frac{\partial \mathbb{F}_2}{\partial \theta}\right)^T \left(-\left(\frac{\partial \mathbb{F}_1}{\partial \theta}\right)^{-T} \frac{\partial \mathbb{F}_1}{\partial \varphi}\right)\right] + $$
$$\frac{\partial J}{\partial u} \left(\frac{-\partial \mathbb{F}_2}{\partial u}\right)^{-T} \frac{\partial \mathbb{F}_2}{\partial \varphi} \tag{8.51}$$

Knowing that $\frac{\partial \mathbb{F}_2}{\partial u} = K$ and assuming

$$\lambda = \frac{\partial J}{\partial u} \left(\frac{-\partial \mathbb{F}_2}{\partial u}\right)^{-T} \tag{8.52}$$

And hence

$$K\lambda = -\frac{\partial J}{\partial u} \tag{8.53}$$

$$K\lambda = -\frac{W_1}{S_1} \int_{\Omega} B_e{}^T C\, B_e\, u\, d\Omega \tag{8.54}$$

Moreover

$$\lambda_x \left(\frac{\partial \mathbb{F}_{2x}}{\partial \boldsymbol{\theta}}\right)^T \left(\left(\frac{\partial \mathbb{F}_1}{\partial \boldsymbol{\theta}}\right)^{-T}\right) = \lambda_x^* \tag{8.55}$$

Assuming $\Lambda = (B_e{}^T C\alpha)$ where $\boldsymbol{\alpha} = \begin{bmatrix} \alpha_{eq} \\ \alpha_{eq} \\ 0 \end{bmatrix}$

$$K_c \lambda_x^* = \int_{\Omega} N_{i,j}^{p;q} \Lambda_x \lambda_x\, d\Omega \tag{8.56}$$

Similarly, in the transverse direction (y) we have

$$K_c \lambda_y^* = \int_{\Omega} N_{i,j}^{p;q} \Lambda_y \lambda_y\, d\Omega \tag{8.57}$$

where Λ_i, λ_i and $\mathbb{F}_{2i}$ are related components of Λ, λ and $\mathbb{F}_2$ vectors corresponding to the i direction. By substituting λ_x^* and λ_y^* in Eq. (8.51) we obtain

$$\frac{\partial J}{\partial u}\frac{\partial u}{\partial \varphi} = \lambda_x^* \left(-\frac{\partial \mathbb{F}_1}{\partial \varphi}\right) + \lambda_y^* \left(-\frac{\partial \mathbb{F}_1}{\partial \varphi}\right) + \lambda\frac{\partial \mathbb{F}_2}{\partial \varphi} \tag{8.58}$$

In addition

$$\lambda\frac{\partial \mathbb{F}_2}{\partial \varphi} = -\left((B_e\lambda)^T \frac{\partial C}{\partial \varphi}\varepsilon_T\right) - \left((B_e\lambda)^T C\frac{\partial \alpha}{\partial \varphi}\Delta\theta\right) + \left((B_e\lambda)^T \frac{\partial C}{\partial \varphi}B_e u\right) \tag{8.59}$$

So, Eq. (8.58) becomes

$$\frac{\partial J}{\partial u}\frac{\partial u}{\partial \varphi} = \int_{\Omega} -\left((B_e\lambda)^T \frac{\partial C}{\partial \varphi}\varepsilon_T\right) - \left((B_e\lambda)^T C\frac{\partial \alpha}{\partial \varphi}\Delta\theta\right) + \left((B_e\lambda)^T \frac{\partial C}{\partial \varphi}B_e u\right)$$
$$+ \left((B_{heat}\lambda_x^*)^T \frac{\partial H}{\partial \varphi}B_{heat}\theta\right) + \left((B_{heat}\lambda_y^*)^T \frac{\partial H}{\partial \varphi}B_{heat}\theta\right) \quad d\Omega \tag{8.60}$$

Eventually, Eq. (8.34) becomes

$$\frac{dJ}{d\varphi} = \int_{\Omega} -\left((B_e\lambda)^T \frac{\partial C}{\partial \varphi}\varepsilon_T\right) - \left((B_e\lambda)^T C\frac{\partial \alpha}{\partial \varphi}\Delta\theta\right) + \left((B_e\lambda)^T \frac{\partial C}{\partial \varphi}B_e u\right)$$
$$+ \left((B_{heat}\lambda_x^*)^T \frac{\partial H}{\partial \varphi}B_{heat}\theta\right) + \left((B_{heat}\lambda_y^*)^T \frac{\partial H}{\partial \varphi}B_{heat}\theta\right) \quad d\Omega$$
$$+ \int_{\Omega} (B_{heat}\,\gamma)^T \frac{\partial H}{\partial \varphi}(B_{heat}\,\theta)\, d\Omega + \frac{W_1}{S_1}\left(\frac{1}{2}\int_{\Omega} (B_e\, u)^T \frac{\partial C}{\partial \varphi}(B_e\, u)\, d\Omega\right)$$
$$+ \frac{W_2}{S_2}\left(\frac{1}{2}\int_{\Omega} (B_{heat}\,\theta)^T \frac{\partial H}{\partial \varphi}(B_{heat}\,\theta)\, d\Omega\right) \tag{8.61}$$

The term $\frac{dV_f}{d\boldsymbol{\varphi}}$ can be also written as

$$\frac{dV_f}{d\boldsymbol{\varphi}} = \frac{\partial V_f}{\partial \boldsymbol{\varphi}} = \int_{\Omega} \frac{\partial \eta_p}{\partial \boldsymbol{\varphi}} \, d\Omega \tag{8.62}$$

8.5 Case studies

Consider a L-shaped CMC component shown in Fig. 8.2. An outward uniform pressure load and an inward uniform heat flux are applied on the left edge while a convection boundary condition is applied on the lower half of the right edge. Mechanical and thermal loadings and boundary conditions are also illustrated in Fig. 8.2(a) and Fig. 8.2(b), respectively. Cooling channels are modeled as point sources on the mid axis of the component and positioned as shown in Fig. 8.2(b). The model is discretized by a 32×16 quadratic B-spline mesh as shown in Fig. 8.2(c). Red dots represent control points.
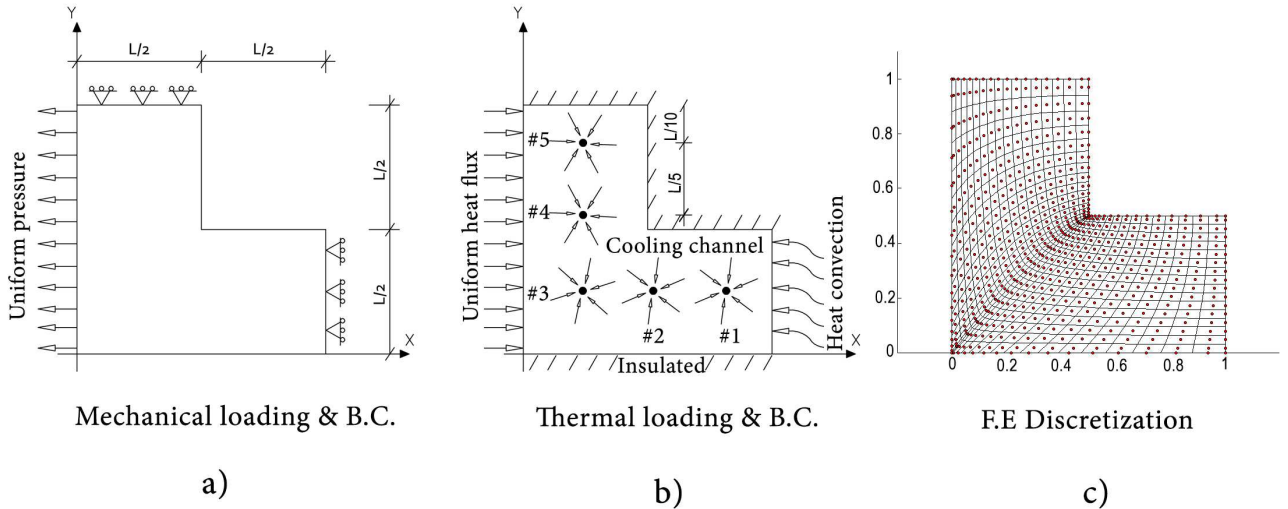
Figure 8.2: Mechanical loading and boundary conditions (a), Thermal loading and boundary conditions (b), FE discretization with red dots as control points (c)

8.5.1 The first stage of the optimization

Finding the optimal total capacity of the cooling channels is investigated in the first stage of the optimization process. Deterministic constraints are set on the first and the last channels (i.e. channels 1 and 5) so that their cooling capacities take a value less

Table 8.1: Design parameters of the L-shaped component under thermomechanical loadings

Parameter/Description(unit)	Value (v/σ)
L / Dimension in Meter (m)	1
E_m / Young's modulus of the matrix (GPa)	88/8
E_c / Young's modulus of the C-fibers (GPa)	200/20
v / Poisson's ratio	0.2
a_m / Thermal expansion coeff. of the matrix $\left(\frac{10^{-6}}{°C}\right)$	4.5
a_c / Thermal expansion coeff. of the C-fibers $\left(\frac{10^{-6}}{°C}\right)$	3.1
k_m / Heat conduction coeff. of the matrix $\left(\frac{W}{m°C}\right)$	45 / 3
k_c / Heat conduction coeff. of the C-fibers $\left(\frac{W}{m°C}\right)$	7 / 0.7
q / heat flux $\left(\frac{W}{m^2}\right)$	800 / 20
h / Convection coeff. $\left(\frac{W}{m^2·°C}\right)$	3 / 0.3
P / Applied load (KN)	1000 / 10
V_{f0} / The total C-fibers volume fraction	40%
θ_{allow} / Max. allowable temperature (°C)	450
δ_{allow} / Max. allowable deflection (mm)	1.5
β / Target reliability index	3
θ_∞ / the temperature of the fluid in convection process (°C)	50

Remarks : μ : *mean value*, σ : *standard deviation*, *Distribution* : *Log Normal*

than 100 *Watts*. The probabilistic constraints are also set on the maximum deflection and temperature of the design domain according to Table 8.1.

The results of the optimization are plotted in Fig. 8.3. The history of the design variables i.e. the capacities of the cooling channels are plotted versus the iterations in Fig. 8.3(a) and Fig. 8.3(b). The final reliability index converges to the target value as illustrated in Fig. 8.3(c) and the objective function finally takes the minimum value according to Fig. 8.3(d).

To show the correctness of the results and also demonstrate the fact that the final optimization output is independent from the initial guess, the maximum allowable capacities on Channels 1 and 5 are reduced from 100 W to 90 W and also the capacity of the Channel 3 is restricted to a value less than 90 W. Different starting points are also considered as the initial guesses for iterations commencement. As expected, the reduction in capacities is compensated by the increase in the cooling capacities of the other channels (i.e. Channels 2 and 4) so that the total required cooling capacity (i.e. the minimum of the objective function) takes the same value as in the previous case. The new results are illustrated in Fig. 8.4. The temperature plot is shown in Fig. 8.5(a), while the displacements in the X and Y directions are plotted in Fig. 8.5(b) and Fig. 8.5(c), respectively.
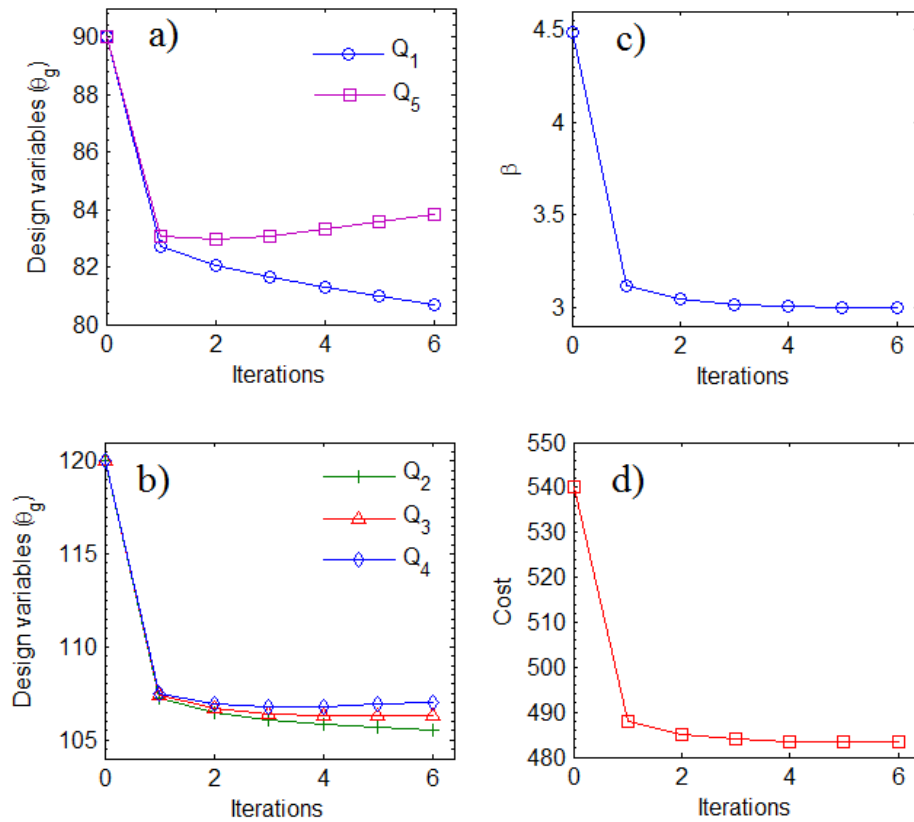
Figure 8.3: Optimization results for target reliability index equal to 3 and with following constraints on channels #1 and #5: $Q_1 \leq 100$ and $Q_5 \leq 100$; Obtained optimum design variables: $Q_1 = 80.71$, $Q_2 = 105.50$, $Q_3 = 106.27$, $Q_4 = 107.02$, $Q_5 = 83.82$; *Optimized cost = 483.32 W*
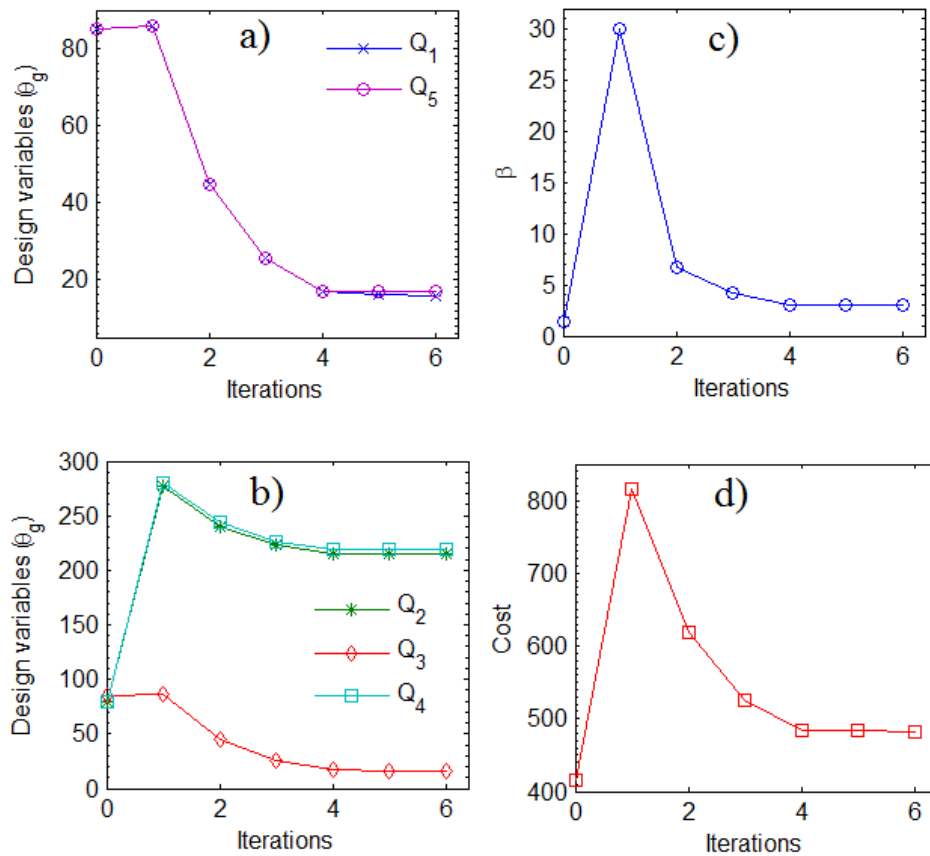
Figure 8.4: Optimization results for target reliability index equal to 3 and with following new constraints on Channels #1, #3 and #5: $Q_1 \leq 90$, $Q_3 \leq 90$ and $Q_5 \leq 90$; Obtained optimum design variables: $Q_1 = 15.81$, $Q_2 = 214.91$, $Q_3 = 16.42$, $Q_4 = 218.62$, $Q_5 = 17.02$; *Optimized cost* $= 482.80\,W$
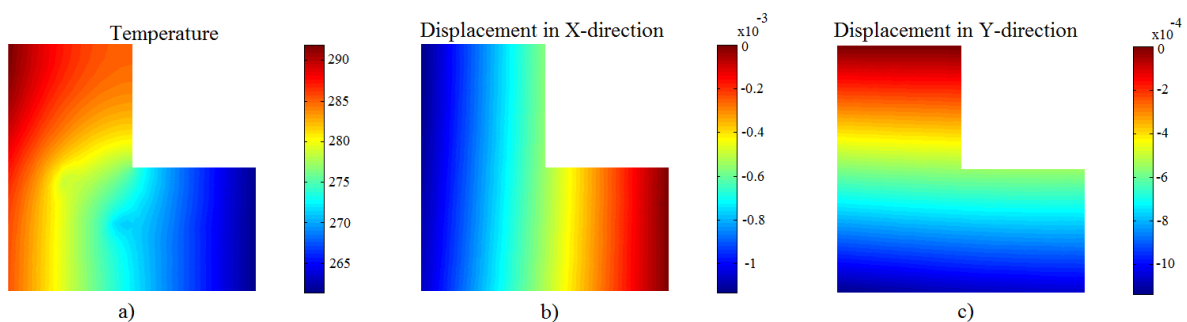
Figure 8.5: Temperature (a), displacement in X-direction (b) and displacement in Y-Direction (c) for CMC component with uniformly distributed C-fibers considering: $Q_1 = 15.81$, $Q_2 = 214.91$, $Q_3 = 16.42$, $Q_4 = 218.62$, $Q_5 = 17.02$

8.5.2 The second stage of the optimization

As discussed in Section 8.2, both mechanical and thermal loadings cause structural deformation. The total nodal displacements (u) consists in u_m which is the displacement caused by mechanical loading and u_θ which is caused by thermal loading. Both mechanical and thermal loading contribute to the formation of the total force vector. Next, two load cases are considered: in Load case-1, the higher temperature load causes u_θ to be around two orders of magnitude higher than u_m and in Load case-2 the high mechanical loading causes u_m to be one order of magnitude higher than u_θ.

8.5.2.1 Load case-1 (high thermal loading)

The lastly obtained optimal capacity of each channel (i.e. $Q_1 = 15.81$, $Q_2 = 214.91$, $Q_3 = 16.42$, $Q_4 = 218.62$, $Q_5 = 17.02$) are used as inputs of the second stage of the optimization process. According to Eq. (8.30), the final optimization results depend on the choice of the weight factors corresponding to the structural and the thermal compliances. Fundamentally, in the weighted sum optimization problem, it is the designer's responsibility to choose appropriate weights of each objective function based on their relative importance. In the present problem it is more straightforward than other multiobjective optimization problems. Since the violation of either mechanical or thermal constraints leads to design failure, the final reliability index, β_{target}, is dominated by β_m or β_t where the former is the reliability index associated with the probabilistic deformation constraint and the latter is associated with the temperature constraint. As the objective functions are contradictory, one can just consider extreme values of weights (i.e. zero or unity) depending on which factor dominates (i.e. is minimum). For instance in this load case having the CMC component with uniformly distributed C-fibers, β_{target} is equal to 3.0089 (which is the minimum of $\beta_m = 3.0089$ and $\beta_t = 4.6684$). Here, β_{target} is dominated by β_m. In order to increase β_{target}, β_m should be increased while minding about reversal of β_t.

Table 8.2 summarizes β_{target}, β_m and β_t for uniformly (item 0) and optimally (items 1 to 5) distributed C-fibers with different combinations of weight factors W_1 and W_2; subscripts 1 and 2 correspond to the mechanical and the thermal weight factors, respectively. One can see from Table 8.2 that item 1 and item 5 (which use the extreme values of the weight factors) provide respectively, the maximum reduction in structural and thermal compliances. However, neither these items nor other combinations of weight factors are able to improve β_m and consequently β_{target}.

To explain this, item 1 is investigated in more detail. The thermal term in the objective function is disregarded as W_2 is set to zero. The total objective function which contains only the structural compliance is minimized while the thermal compliance increases. Fig. 8.6(a) illustrates the history of the structural and thermal compliance terms over the iterations. The total objective function does not converge, smoothly,

Table 8.2: Summary of optimization results in Load case-1 for uniformly and optimally distributed C-fibers with different combinations of weight factors

	Item	W_1/W_2	Total objective	Structural compliance	β_m	Thermal compliance	β_t	β_{target}
Uniform	0	-	1	1	3.0089	1	4.6684	3.0089
Optimally distributed C-fibers	1	1/0	0.959	0.959	2.4976	1.083	4.6835	2.4976
	2	0.75/0.25	0.961	0.972	2.3783	0.929	4.6753	2.3783
	3	0.5/0.5	0.950	0.979	2.3518	0.920	4.6700	2.3518
	4	0.25/0.75	0.935	0.982	2.3748	0.920	4.6689	2.3748
	5	0/1	0.920	0.9840	2.4	0.920	4.6686	2.4

towards the minimum value.

This undesired phenomenon that a decrease in the structural compliance yields to a larger maximum structural deformation (which consequently causes lower β_m) is caused by the coupling between the thermal and the mechanical fields and the contradictory effects of C-fibers on these fields. In a typical elastic problem, when the stiffness increases as the force vector remains unchanged, the maximum structural deformation will decrease. In the coupled thermoelastic problem, the forces induced by the temperature field and consequently the total force vector does not remain unchanged. According to Eq. (8.12), the force induced by the temperature field will change when the Young's modulus, thermal expansion coefficient or nodal temperatures deviate. Since all of these items are functions of the volume fraction of C-fibers, the final magnitude of the force vector depends on the distribution of the C-fibers. Thus, any increase or decrease in the maximum deflection of a CMC component depends on the changes of structural stiffness and force induced by the temperature field and should be evaluated case by case based on the constituent material properties and the loading conditions.

To gain better insight into this issue, the same problem is solved assuming the mechanical and thermal fields are decoupled. This is accomplished by setting the thermal expansion coefficients of both the C-fibers and the matrix to zero. Fig. 8.6(b) shows the results for the decoupled problem. In this case the objective function smoothly converges towards the minimum value and the optimization process is stable.

In item 5 ($W_1 = 0$ and $W_2 = 1$) the structural term in the objective function is disregarded. Thus the total objective function consists only by the thermal compliance contribution. The optimal distribution of the C-fibers and the history of the objective functions over the iterations are presented in Fig. 8.7. As the mechanical field doesn't affect the thermal field, the optimization process is stable and the objective function smoothly converge towards its minimum value, though the problem is coupled.
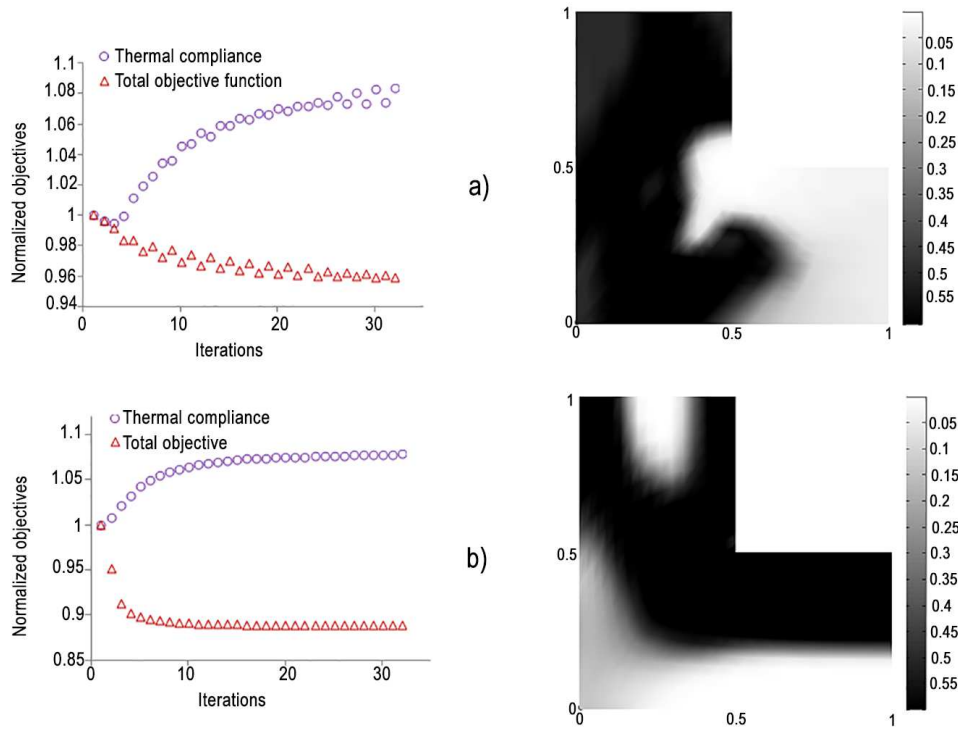
Figure 8.6: History of the objective functions and optimal distribution of the C-fibers inside the matrix considering $W_1 = 1$ and $W_2 = 0$ for coupled (a) and decoupled (b) cases. $Q_1 = 15.81$, $Q_2 = 214.91$, $Q_3 = 16.42$, $Q_4 = 218.62$ and $Q_5 = 17.02$ while the other design parameters are according to Table 8.1
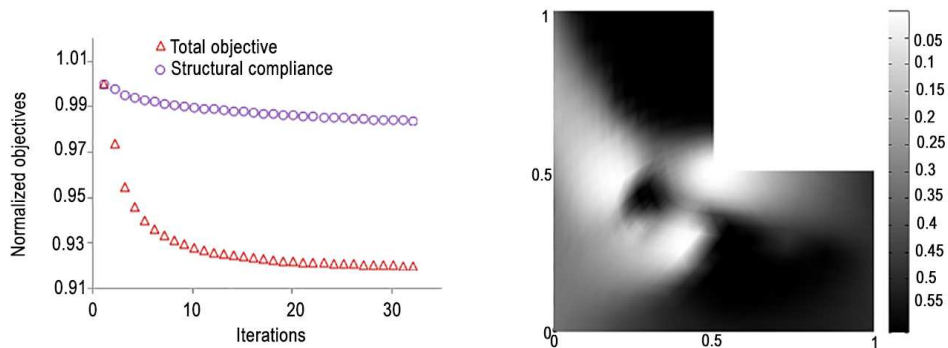
Figure 8.7: History of the objective functions and optimal distribution of the C-fibers inside the matrix considering $W_1 = 0$ and $W_2 = 1$ for coupled problem

8.5.2.2 Load case-2 (high mechanical loading)

Now, the applied mechanical load is increased so that it dominates the thermal one. Table 8.3 includes the new design parameters. Other design parameters remain unchanged according to Table 8.1. The results of the optimization for this load case are

Table 8.3: New design parameters of the L-shaped component under thermomechanical loading

Parameter / Description (unit)	Value (μ/σ)
P / Applied load (KN)	1000000 / 10000
σ_{allow} / Max. allowable deflection (mm)	50

other design parameters according to Table 8.1

summarized in Table 8.4. Item 0 refers to uniformly distributed C-fibers. In item 1 the thermal term is disregarded and the total objective function just includes the structural term while item 2 acts reversely. Fig. 8.8(a) shows the optimal distribution of

Table 8.4: Summary of optimization results in Load case-2 for uniformly and optimally distributed C-fibers with different combinations of weight factors

	Item	W_m/W_t	Structural compliance	β_m	Thermal compliance	β_t	β_{target}
Uniform	0	-	1	2.8916	1	4.6684	2.8913
Optimal	1	1 / 0	0.8963	4.4259	1.0814	4.5803	4.34
	2	0 / 1	1.060	2.3323	0.920	4.6686	2.3322

C-fibers and the history of the objective functions for item 1, respectively. Decreasing the structural compliance yields an increase in the structural stiffness. Since the C-fibers distribution is changed, f also changes. Contrary to the previous case, as the thermal force is smaller than the mechanical force, its deviation does not influence the total force vector severely, resulting in a decrease in the maximum structural deflection and consequently a considerable increase in β_m and eventually β_{target}.

The optimal distribution of C-fibers and the history of objective functions for different weights are illustrated in Fig. 8.8(b). The structural compliance is disregarded in the total objective function and increases while the objective function (i.e. thermal compliance) is minimized. Although the thermal compliance is decreased, the reduction in maximum temperature and consequently in β_t is trifle and not sensible. However, as β_m decreases (due to the increase in structural compliance), β_{target} also decreases.
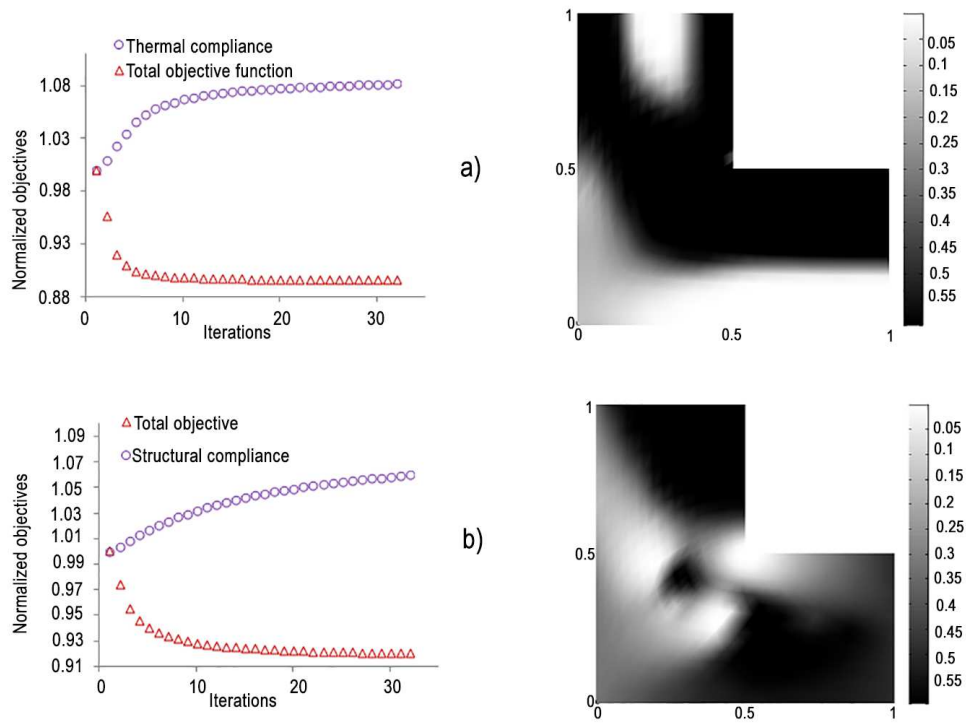
Figure 8.8: History of the objective functions and optimal distribution of the C-fibers inside the matrix considering $W_1 = 1$ and $W_2 = 0$ (a) and $W_1 = 0$ and $W_2 = 1$ (b). Both (a) and (b) are coupled problems

8.6 Concluding remarks

Ceramic matrix composites which are manufactured by adding reinforcements such as carbon fibers to a ceramic matrix show improved toughness properties in comparison with pure ceramics. Usually, components made of CMCs are cooled by internal cooling channels because typical C-fibers are vulnerable to high temperature oxidizing atmospheres. Firstly, the presented computational platform efficiently optimizes the capacity of cooling channels using RBDO approach. A series system reliability concept is adopted as a union of mechanical and thermal failure subsets. Secondly, the optimizer is supposed to increase the reliability of the component by optimally distributing the C-fibers inside the matrix within the design domain. Numerical results for the performed case studies demonstrate that optimal distribution of C-fibers can decrease structural and thermal compliances. In the decoupled elastic and thermal problems, the former yields an increase in β_m (the reliability index associated with the probabilistic deformation constraint) and the latter in an increase in β_t (the reliability index associated with the probabilistic thermal constraint). But, in the coupled thermoelastic problem, any prediction about final reliability indices depends on fiber and matrix constitutive material properties and contribution of mechanical and thermal loadings on the global force vector. When the mechanical loading dominates the thermal loading, fiber distribution can show promising advantage to have more reliable design by increasing β_m and consequently β_{target} (the final reliability index). However, its role for increasing the reliability index corresponding to thermal constraint is negligible.

Chapter 9

Application 3: A level-set based IGA formulation for topology optimization of flexoelectric materials

9.1 Introduction

The piezoelectric effect, which only exists in materials with non-centrosymmetric crystal structures, refers to a linear dependence between the electric polarization, $\boldsymbol{P}$ and the mechanical strain, $\boldsymbol{\varepsilon}$ given by

$$P_i = p_{ijk}\varepsilon_{jk} \tag{9.1}$$

where $\boldsymbol{p}$ is the third order piezoelectric tensor [Sharma *et al.*, 2007 ; Nanthakumar *et al.*, 2016 ; Nanthakumar *et al.*, 2014 and Nanthakumar *et al.*, 2013]. In contrast to piezoelectricity, flexoelectricity is possible in all dielectrics, including those with centrosymmetric crystal structures, and is thus a more general electromechanical coupling mechanism. When flexoelectric effects are accounted for, the polarization is written as

$$P_i = p_{ijk}\varepsilon_{jk} + \mu_{ijkl}\frac{\partial \varepsilon_{jk}}{\partial x_l} \tag{9.2}$$

where the electric polarization exhibits a linear response to the gradient of mechanical strain [Yudin & Tagantsev, 2013]. In Eq. (9.2) μ_{ijkl} are the flexoelectric coefficients; the first term on the right hand side is zero for non-piezoelectric materials.

Flexoelectricity in solids was introduced by Mashkevich & Tolpygo, 1957 but received little attention, likely because the flexoelectric effect is relatively insignificant for bulk crystalline materials. However recent developments in nanotechnology have shed a new light on flexoelectricity as a size dependent phenomenon due to the large strain gradients that are obtainable at small length scales, or alternatively in soft materials like biological membranes [Ahmadpour & Sharma, 2015]. For additional recent

reviews on flexoelectricity interested readers are referred to [Nguyen *et al.*, 2013] and [Zubko *et al.*, 2013].

While the theoretical basis for flexoelectricity in dielectrics has been developed in detail [Sharma *et al.*, 2007 ; Majdoub *et al.*, 2009 and Sharma *et al.*, 2010], there have been a correspondingly small number of numerical studies. Recently, Abdollahi *et al.*, 2014 presented a computational framework to evaluate the flexoelectric effect in dielectric solids using a meshfree method in 2D [Abdollahi *et al.*, 2014] and 3D [Abdollahi *et al.*, 2015]. They showed that available simplified analytical solutions only provide order of magnitude estimates in comparison with a more general model which considers the multidimensional coupling effects.

Topology optimization is a powerful approach that optimizes the material distribution within the design domain. The first computational model for topology optimization was presented by Bendse & Kikuchi, 1988. Topology optimization has since been successfully applied to a variety of applications such as structural design [Sigmund, 2001a], compliant mechanism [Sigmund, 1997] and microelectromechanical system [Sigmund, 2001b and Nanthakumar *et al.*, 2015]. To the author's best of knowledge, employing topology optimization for dielectric solids in order to enhance their flexoelectric behavior has not been done to-date.

Various techniques have been developed for topology optimization. Among them, the Solid Isotropic Material with Penalization (SIMP) technique [Rozvany *et al.*, 1992] is very common due to its simplicity. Although this technique has been widely applied to different problems, researchers have encountered difficulties with its numerical stability in some multiphysics and multiconstraint problems [Wang *et al.*, 2003]. Furthermore, in multiphysics problems the different sets of penalization parameters will directly and noticeably impact the final results in terms of the stability of the solution and the distinct void-solid representation.

To overcome the above mentioned difficulties, the Level Set Method (LSM) [Osher & Sethian, 1988] for topology optimization is employed here in order to exploit its intrinsic flexibility in handling topological changes. In the LSM, the boundaries of the domain are implicitly represented with a scalar level set function which changes in time, providing unique benefits such as smooth boundaries and distinct interfaces, integrated shape and topology optimization. IGA is also used instead of standard FEM because the fourth order PDEs of flexoelectricity demand at least C^1 continuous basis functions in a Galerkin method [Abdollahi *et al.*, 2014]. IGA also enables using the same data set for the analysis and the optimization as well as an exact representation of the geometry (see Chapter 2).

9.2 Flexoelectricity: theory and formulation

For a linear dielectric solid possessing only the piezoelectric effect, the electric enthalpy density, $\mathscr{H}$, is a function of $\boldsymbol{\varepsilon}$ and $\boldsymbol{E}$, i.e. $\mathscr{H}(\varepsilon_{ij}, E_i)$. When flexoelectric effects are accounted for, the enthalpy density $\mathscr{H}$ also becomes a function of the strain gradient and electric field gradient. Thus

$$\mathscr{H}(\varepsilon_{ij}, E_i, \varepsilon_{jk,l}, E_{i,j}) = \frac{1}{2}C_{ijkl}\varepsilon_{ij}\varepsilon_{kl} - e_{ikl}E_i\varepsilon_{kl} + (d_{ijkl}E_{i,j}\varepsilon_{kl} + f_{ijkl}E_i\varepsilon_{jk,l}) - \frac{1}{2}\kappa_{ij}E_iE_j \tag{9.3}$$

where $E_i = -\theta_{,i}$ is the electric field; $\boldsymbol{\theta}$ is the electric potential; $\boldsymbol{\varepsilon}$ is the mechanical strain; $\boldsymbol{e}$ is the third-order tensor of piezoelectricity; $\boldsymbol{\kappa}$ is the second-order dielectric tensor; $\boldsymbol{C}$ is the fourth-order elasticity tensor; $\boldsymbol{f}$ is the fourth-order direct flexoelectric tensor and $\boldsymbol{d}$ is the fourth-order converse flexoelectric tensor [Abdollahi *et al.*, 2014]. Let's consider the terms in the brackets on the RHS of Eq. (9.3) containing the direct and reverse flexoelectric effects. Integrating these terms over the volume and using integration by parts and the Gauss divergence theorem on the first term yields

$$\int_{\Omega}(d_{ijkl}E_{i,j}\varepsilon_{kl} + f_{ijkl}E_i\varepsilon_{jk,l})d\Omega = \int_{\Omega}d_{ijkl}E_{i,j}\varepsilon_{kl}d\Omega + \int_{\Omega}f_{ijkl}E_i\varepsilon_{jk,l}d\Omega$$

$$= \int_{\partial\Omega}d_{ijkl}E_i\varepsilon_{kl}ds - \int_{\Omega}d_{ijkl}E_i\varepsilon_{kl,j}d\Omega + \int_{\Omega}f_{ijkl}E_i\varepsilon_{jk,l}d\Omega$$

$$= \int_{\Omega}(f_{ijkl}E_i\varepsilon_{jk,l} - d_{ijkl}E_i\varepsilon_{kl,j})d\Omega + \int_{\partial\Omega}d_{ijkl}E_i\varepsilon_{kl}ds \tag{9.4}$$

$$= -\int_{\Omega}(d_{iljk} - f_{ijkl})E_i\varepsilon_{jk,l}d\Omega + \int_{\partial\Omega}d_{ijkl}E_i\varepsilon_{kl}ds$$

$$= -\int_{\Omega}\mu_{ijkl}E_i\varepsilon_{jk,l}d\Omega + \int_{\partial\Omega}d_{ijkl}E_i\varepsilon_{kl}ds$$

which is expressed in terms of only one material tensor, $\boldsymbol{\mu}$ where $\mu_{ijkl} = d_{iljk} - f_{ijkl}$. Therefore, one can rewrite Eq. (9.3) as

$$\mathscr{H}(\varepsilon_{ij}, E_i, \varepsilon_{jk,l}) = \frac{1}{2}C_{ijkl}\varepsilon_{ij}\varepsilon_{kl} - e_{ikl}E_i\varepsilon_{kl} - \mu_{ijkl}E_i\varepsilon_{jk,l} - \frac{1}{2}\kappa_{ij}E_iE_j \tag{9.5}$$

For a pure piezoelectric material we have

$$\sigma_{ij} = \frac{\partial\overline{\mathscr{H}}}{\partial\varepsilon_{ij}} \qquad and \qquad D_i = -\frac{\partial\overline{\mathscr{H}}}{\partial E_i} \tag{9.6}$$

while in the presence of flexoelectricity, the electromechanical stresses including the usual ($\widehat{\sigma}_{ij}/\widehat{D}_i$), higher-order ($\widetilde{\sigma}_{ijk}/\widetilde{D}_{ij}$) and physical ($\sigma_{ij}/D_i$) ones are defined through the following relations:

$$\widehat{\sigma}_{ij} = \frac{\partial\mathscr{H}}{\partial\varepsilon_{ij}} \qquad and \qquad \widehat{D}_i = -\frac{\partial\mathscr{H}}{\partial E_i} \tag{9.7}$$

$$\widetilde{\sigma}_{ijk} = \frac{\partial \mathcal{H}}{\partial \varepsilon_{ij,k}} \quad and \quad \widetilde{D}_{ij} = -\frac{\partial \mathcal{H}}{\partial E_{i,j}} \tag{9.8}$$

$$\sigma_{ij} = \widehat{\sigma}_{ij} - \widetilde{\sigma}_{ijk,k} \quad and \quad D_i = \widehat{D}_i - \widetilde{D}_{ij,j} \tag{9.9}$$

thus

$$\sigma_{ij} = \widehat{\sigma}_{ij} - \widetilde{\sigma}_{ijk,k} = C_{ijkl}\varepsilon_{kl} - e_{kij}E_k + \mu_{lijk}E_{l,k} \tag{9.10}$$

$$D_i = \widehat{D}_i - \widetilde{D}_{ij,j} = e_{ikl}\varepsilon_{kl} + \kappa_{ij}E_j + \mu_{ijkl}\varepsilon_{jk,l} \tag{9.11}$$

Since $\widetilde{D}_{ij}$ has no contribution in Eq. (9.5) thus, the essential and natural electrical boundary conditions are the same as electrostatics. So,

$$\theta = \overline{\theta} \quad on \quad \Gamma_\theta \tag{9.12}$$

$$D_i n_i = -\omega \quad on \quad \Gamma_D \tag{9.13}$$

$$\Gamma_\theta \cup \Gamma_D = \partial\Omega \quad and \quad \Gamma_\theta \cap \Gamma_D = \emptyset \tag{9.14}$$

where $\overline{\theta}$ and ω are the prescribed electric potential and surface change density; n_i is the unit normal to the boundary $\partial\Omega$ of the domain Ω.

For the mechanical boundary conditions we have

$$u_i = \overline{u}_i \quad on \quad \Gamma_u \tag{9.15}$$

$$t_k = n_j(\widehat{\sigma}_{jk} - \widetilde{\sigma}_{ijk,l}) - D_j(n_i\widetilde{\sigma}_{ijk}) - (D_p n_p)n_i n_j\widetilde{\sigma}_{ijk} = \overline{t}_k \quad on \quad \Gamma_t \tag{9.16}$$

$$\Gamma_u \cup \Gamma_t = \partial\Omega \ and \ \Gamma_u \cap \Gamma_t = \emptyset \tag{9.17}$$

where $\overline{u}_i$ and $\overline{t}_k$ are the prescribed mechanical displacements and tractions; D_j is the surface gradient operator. In addition to these, the strain gradients result in other types of boundary conditions as follows

$$u_{i,j}n_j = \overline{v}_i \quad on \ \Gamma_v \tag{9.18}$$

$$n_i n_j \widetilde{\sigma}_{ijk} = \overline{r}_k \quad on \ \Gamma_r \tag{9.19}$$

$$\Gamma_v \cup \Gamma_r = \partial\Omega \ and \ \Gamma_v \cap \Gamma_r = \emptyset \tag{9.20}$$

where $\bar{\upsilon}_i$ and $\bar{r}_k$ are the prescribed normal derivative of displacement and the higher order traction, respectively. Eq. (9.7) and Eq. (9.8) can be rewritten as

$$\partial \mathscr{H} = \widehat{\sigma}_{ij} \partial \varepsilon_{ij} \tag{9.21}$$

$$\partial \mathscr{H} = \widetilde{\sigma}_{ijk} \partial \varepsilon_{ij,k} \tag{9.22}$$

$$\partial \mathscr{H} = -\widehat{D}_i \partial E_i \tag{9.23}$$

and then by integrating over Ω we obtain

$$H = \frac{1}{2} \int_{\Omega} (\widehat{\sigma}_{ij} \varepsilon_{ij} + \widetilde{\sigma}_{ijk} \varepsilon_{ij,k} - \widehat{D}_i E_i) d\Omega \tag{9.24}$$

where H is the total electrical enthalpy.

The work done by the external surface mechanical and electrical forces can be written as

$$W_{ext} = \int_{\Gamma_t} \bar{t}_i u_i dS - \int_{\Gamma_D} \omega \theta dS \tag{9.25}$$

The kinetic energy for the system is also defined as

$$K_E = \frac{1}{2} \int_{\Omega} \rho \dot{u}_i \dot{u}_i d\Omega \tag{9.26}$$

where ρ denotes the density and the superimposed dot indicate time derivative. Using Hamilton principle without the damping term we have

$$\delta \int_{t_1}^{t_2} (K_E - H + W_{ext}) dt = 0 \tag{9.27}$$

and

$$
\begin{aligned}
\delta \int_{t_1}^{t_2} \Bigg(&\frac{1}{2} \int_{\Omega} \rho \dot{u}_i \dot{u}_i d\Omega - \frac{1}{2} \int_{\Omega} (\widehat{\sigma}_{ij} \varepsilon_{ij} + \widetilde{\sigma}_{ijk} \varepsilon_{ij,k} - \widehat{D}_i E_i) d\Omega \\
&+ \int_{\Gamma_t} \bar{t}_i u_i dS - \int_{\Gamma_D} \omega \theta dS \Bigg) dt = 0
\end{aligned}
\tag{9.28}
$$

moving the variation operation into the integral operations we obtain

$$
\begin{aligned}
\int_{t_1}^{t_2} \Bigg(&\frac{1}{2} \int_{\Omega} \delta(\rho \dot{u}_i \dot{u}_i) d\Omega - \frac{1}{2} \int_{\Omega} \delta(\widehat{\sigma}_{ij} \varepsilon_{ij} + \widetilde{\sigma}_{ijk} \varepsilon_{ij,k} - \widehat{D}_i E_i) d\Omega \\
&+ \int_{\Gamma_t} \bar{t}_i \delta u_i dS - \int_{\Gamma_D} \omega \delta \theta dS \Bigg) dt = 0
\end{aligned}
\tag{9.29}
$$

by changing the order of operations and using the chain rule of variation we have

$$\int_{t_1}^{t_2} \left[\frac{1}{2} \int_{\Omega} \delta(\rho \dot{u}_i \dot{u}_i) d\Omega \right] dt = - \int_{t_1}^{t_2} \left[\int_{\Omega} \rho(\delta u_i \ddot{u}_i) d\Omega \right] dt \qquad (9.30)$$

$$\int_{t_1}^{t_2} \left[\frac{1}{2} \int_{\Omega} \delta(\widehat{\sigma}_{ij}\varepsilon_{ij} + \tilde{\sigma}_{ijk}\varepsilon_{ij,k} - \widehat{D}_i E_i) d\Omega \right] dt = \int_{t_1}^{t_2} \left[\int_{\Omega} (\widehat{\sigma}_{ij}\delta\varepsilon_{ij} + \tilde{\sigma}_{ijk}\delta\varepsilon_{ij,k} - \widehat{D}_i \delta E_i) d\Omega \right] dt \qquad (9.31)$$

Eq. (9.29) now becomes

$$\int_{t_1}^{t_2} \left(- \int_{\Omega} \rho(\delta u_i \ddot{u}_i) d\Omega - \int_{\Omega} (\widehat{\sigma}_{ij}\delta\varepsilon_{ij} + \tilde{\sigma}_{ijk}\delta\varepsilon_{ij,k} - \widehat{D}_i \delta E_i) d\Omega \right.$$
$$\left. + \int_{\Gamma_t} \bar{t}_i \delta u_i dS - \int_{\Gamma_D} \omega \delta\theta dS \right) dt = 0 \qquad (9.32)$$

To satisfy Eq. (9.32) for all possible choices of u, the integrand of the time integration has to vanish, which leads to

$$\int_{\Omega} \rho(\delta u_i \ddot{u}_i) d\Omega + \int_{\Omega} (\widehat{\sigma}_{ij}\delta\varepsilon_{ij} + \tilde{\sigma}_{ijk}\delta\varepsilon_{ij,k} - \widehat{D}_i \delta E_i) d\Omega - \int_{\Gamma_t} \bar{t}_i \delta u_i dS + \int_{\Gamma_D} \omega \delta\theta dS = 0 \qquad (9.33)$$

The inertia term is neglected for a static problem yielding

$$\int_{\Omega} (\widehat{\sigma}_{ij}\delta\varepsilon_{ij} + \tilde{\sigma}_{ijk}\delta\varepsilon_{ij,k} - \widehat{D}_i \delta E_i) d\Omega - \int_{\Gamma_t} \bar{t}_i \delta u_i dS + \int_{\Gamma_D} \omega \delta\theta dS = 0 \qquad (9.34)$$

Substituting Eqs. (9.7)- (9.11) into Eq. (9.34)) yields

$$\int_{\Omega} \left(C_{ijkl}\delta\varepsilon_{ij}\varepsilon_{kl} - e_{kij}E_k\delta\varepsilon_{ij} - \mu_{lijk}E_l\delta\varepsilon_{ij,k} - \kappa_{ij}\delta E_i E_j - e_{ikl}\delta E_i\varepsilon_{kl} - \mu_{ijkl}\delta E_i\varepsilon_{jk,l} \right) d\Omega$$
$$- \int_{\Gamma_t} \bar{t}_i \delta u_i dS + \int_{\Gamma_D} \omega \delta\theta dS = 0 \qquad (9.35)$$

9.3 Discretization

In this section the NURBS basis functions are employed to approximate displacement u and electric potential θ fields as well as their derivatives according to

$$u_h(x,y) = \sum_{i=1}^{n} \sum_{j=1}^{m} N_{i,j}^{p,q}(\xi,\eta) u_{ij}^e = (N_u)^T u^e \qquad (9.36)$$

$$\theta_h(x,y) = \sum_{i=1}^{n} \sum_{j=1}^{m} N_{i,j}^{p,q}(\xi,\eta)\theta_{ij}^e = (\boldsymbol{N}_\theta)^T \boldsymbol{\theta}^e \tag{9.37}$$

$$\partial_j u_h = \partial_j \boldsymbol{N}_u \boldsymbol{u}^e = (\boldsymbol{B}_u)^T \boldsymbol{u}^e = \boldsymbol{\varepsilon} \tag{9.38}$$

$$\partial_j \theta_h = \partial_j \boldsymbol{N}_\theta \boldsymbol{\theta}^e = (\boldsymbol{B}_\theta)^T \boldsymbol{\theta}^e = -\boldsymbol{E} \tag{9.39}$$

$$\partial_j \partial_k u_h = \partial_j \partial_k \boldsymbol{N}_u \boldsymbol{u}^e = (\boldsymbol{H}_u)^T \boldsymbol{u}^e \tag{9.40}$$

where the superscript e denotes nodal parameters at the control points; $\boldsymbol{B}_u$, $\boldsymbol{B}_\theta$ and $\boldsymbol{H}_u$ are the matrices containing the gradient and Hessian of the corresponding basis functions (i.e. $\boldsymbol{N}_u$ and $\boldsymbol{N}_\theta$) which are defined as

$$\boldsymbol{B}_u = \begin{bmatrix} \frac{\partial N_1}{\partial x} & 0 & \frac{\partial N_1}{\partial y} \\ \frac{\partial N_2}{\partial x} & 0 & \frac{\partial N_2}{\partial y} \\ \vdots & \vdots & \vdots \\ \frac{\partial N_n}{\partial x} & 0 & \frac{\partial N_n}{\partial y} \\ 0 & \frac{\partial N_1}{\partial y} & \frac{\partial N_1}{\partial x} \\ 0 & \frac{\partial N_2}{\partial y} & \frac{\partial N_2}{\partial x} \\ \vdots & \vdots & \vdots \\ 0 & \frac{\partial N_n}{\partial y} & \frac{\partial N_n}{\partial x} \end{bmatrix} \tag{9.41}$$

$$\boldsymbol{B}_\theta = \begin{bmatrix} \frac{\partial N_1}{\partial x} & \frac{\partial N_1}{\partial y} \\ \vdots & \vdots \\ \frac{\partial N_n}{\partial x} & \frac{\partial N_n}{\partial y} \end{bmatrix} \tag{9.42}$$

$$\boldsymbol{H}_u = \begin{bmatrix} \frac{\partial^2 N_1}{\partial x^2} & 0 & \frac{\partial^2 N_1}{\partial y \partial x} & \frac{\partial^2 N_1}{\partial x \partial y} & 0 & \frac{\partial^2 N_1}{\partial y^2} \\ \frac{\partial^2 N_2}{\partial x^2} & 0 & \frac{\partial^2 N_2}{\partial y \partial x} & \frac{\partial^2 N_2}{\partial x \partial y} & 0 & \frac{\partial^2 N_2}{\partial y^2} \\ \vdots & \vdots & \vdots & \vdots & \vdots & \vdots \\ \frac{\partial^2 N_n}{\partial x^2} & 0 & \frac{\partial^2 N_n}{\partial y \partial x} & \frac{\partial^2 N_n}{\partial x \partial y} & 0 & \frac{\partial^2 N_n}{\partial y^2} \\ 0 & \frac{\partial^2 N_1}{\partial y \partial x} & \frac{\partial^2 N_1}{\partial x^2} & 0 & \frac{\partial^2 N_1}{\partial y^2} & \frac{\partial^2 N_1}{\partial x \partial y} \\ 0 & \frac{\partial^2 N_2}{\partial y \partial x} & \frac{\partial^2 N_2}{\partial x^2} & 0 & \frac{\partial^2 N_2}{\partial y^2} & \frac{\partial^2 N_2}{\partial x \partial y} \\ \vdots & \vdots & \vdots & \vdots & \vdots & \vdots \\ 0 & \frac{\partial^2 N_n}{\partial y \partial x} & \frac{\partial^2 N_n}{\partial x^2} & 0 & \frac{\partial^2 N_n}{\partial y^2} & \frac{\partial^2 N_n}{\partial x \partial y} \end{bmatrix} \tag{9.43}$$

By substituting Eq. (9.36) to Eq. (9.40) into Eq. (9.35) we obtain after some algebra the following discrete system of equations

$$
\begin{bmatrix} A_{UU} & A_{U\theta} \\ A_{\theta U} & A_{\theta\theta} \end{bmatrix} \begin{bmatrix} U \\ \theta \end{bmatrix} = \begin{bmatrix} f_U \\ f_\theta \end{bmatrix} \tag{9.44}
$$

where

$$
A_{UU} = \sum_e \int_{\Omega_e} (B_u) C (B_u)^T d\Omega_e \tag{9.45}
$$

$$
A_{U\theta} = \sum_e \int_{\Omega_e} \left[(B_u) e (B_\theta)^T + (H_u) \mu^T (B_\theta)^T \right] d\Omega_e \tag{9.46}
$$

$$
A_{\theta U} = \sum_e \int_{\Omega_e} \left[(B_\theta) e^T (B_u)^T + (B_\theta) \mu (H_u)^T \right] d\Omega_e \tag{9.47}
$$

$$
A_{\theta\theta} = -\sum_e \int_{\Omega_e} (B_\theta) \kappa (B_\theta)^T d\Omega_e \tag{9.48}
$$

$$
f_U = \sum_e \int_{\Gamma_{te}} N_u^T t_\Gamma d\Gamma_{te} \tag{9.49}
$$

$$
f_\theta = -\sum_e \int_{\Gamma_{De}} N_\theta^T \omega d\Gamma_{De} \tag{9.50}
$$

In Eqs. (9.45) - (9.50), the subscript, e, in Ω_e, Γ_{te} and Γ_{De} denotes the eth finite element where $\Omega = \cup_e \Omega_e$. Moreover, C, κ, e and μ can be written in matrix form as

$$
C = \left(\frac{E}{(1+v)(1-2v)} \right) \begin{bmatrix} 1-v & v & 0 \\ v & 1-v & 0 \\ 0 & 0 & \left(\frac{1}{2}-v\right) \end{bmatrix} \tag{9.51}
$$

$$
\kappa = \begin{bmatrix} \kappa_{11} & 0 \\ 0 & \kappa_{33} \end{bmatrix} \tag{9.52}
$$

$$
e^T = \begin{bmatrix} 0 & 0 & e_{15} \\ e_{31} & e_{33} & 0 \end{bmatrix} \tag{9.53}
$$

$$
\mu = \begin{bmatrix} \mu_{11} & \mu_{12} & 0 & 0 & 0 & \mu_{44} \\ 0 & 0 & \mu_{44} & \mu_{12} & \mu_{11} & 0 \end{bmatrix} \tag{9.54}
$$

Interested readers can also refer to [Sharma *et al.*, 2007] and [Majdoub *et al.*, 2009] for more details about the theory of flexoelectricity.

9.4   Level Set Method (LSM) and optimization problem

9.4.1   LSM

In this section the LSM fundamentals are briefly described. Let's assume $\Omega \subset D \subset \mathbb{R}^d$ ($d = 2$ or 3), where D is the whole structural domain including all admissible shapes, Ω. A level set function $\Phi(\boldsymbol{x})$ is defined as

$$\begin{cases} Solid : \Phi(\boldsymbol{x}) > 0 & \forall \boldsymbol{x} \in \Omega \setminus \partial\Omega \\ Boundary : \Phi(\boldsymbol{x}) = 0 & \forall \boldsymbol{x} \in \partial\Omega \cap D \\ Void : \Phi(\boldsymbol{x}) < 0 & \forall \boldsymbol{x} \in D \setminus \Omega \end{cases} \tag{9.55}$$

The design boundary $\Gamma(\boldsymbol{x})$ is then implicitly represented by the iso-surface (in this text zero surface) of $\Phi(\boldsymbol{x})$ such that

$$\Gamma(\boldsymbol{x}) = \left\{ \boldsymbol{x} \in \mathbb{R}^d | \Phi(\boldsymbol{x}) = 0 \right\} \tag{9.56}$$

and by letting the level set function dynamically change in time, the dynamic model is expressed as

$$\Gamma(t) = \left\{ \boldsymbol{x}(t) \in \mathbb{R}^d | \Phi(\boldsymbol{x}(t), t) = 0 \right\} \tag{9.57}$$

and by differentiating both sides of Eq. (9.57) with respect to time and applying the chain rule we have

$$\frac{\partial \Phi(\boldsymbol{x}(t), t)}{\partial t} + \nabla\Phi(\boldsymbol{x}(t), t) \cdot \frac{dx}{dt} = 0 \tag{9.58}$$

where $\boldsymbol{V} = \frac{dx}{dt}$ is the velocity vector of the design boundary and its normal component is $V_n = \boldsymbol{V} \cdot \boldsymbol{n}$ where $\boldsymbol{n} = \frac{\nabla\Phi}{|\nabla\Phi|}$ is the unit outward normal to the boundary. Eq. (9.58) is the so-called Hamilton-Jacobi equation and can be written in the form of

$$\frac{\partial \Phi}{\partial t} + V_n |\nabla\Phi| = 0 \tag{9.59}$$

which defines an initial value problem for the time dependent function Φ. In optimization process V_n is the movement of a point on a surface driven by the objective of the optimization. The optimal structural boundary is then expressed as a solution of Eq. (9.59) obtained by a so called "up-wind scheme" [Wang *et al.*, 2003].

In this section, the LS function at the point (x, y) is denoted by $\Phi(x, y)$ and defined as

$$\Phi(x, y) = \sum_{i=1}^{n} \sum_{j=1}^{m} N_{i,j}^{p,q}(\xi, \eta) \varphi_{i,j} \tag{9.60}$$

where $N_{i,j}^{p,q}$ and $\varphi_{i,j}$ are B-spline basis functions and corresponding nodal values of LS, respectively. $\varphi_{i,j}$ are the only design variables which are defined on the control points mesh being set as the signed distance to the given boundary of the initial design.

The density-based approach is used for mapping the geometry to the mechanical model. Using this approach, the material domain (density field $0 < \rho_{min} \leq \rho(\boldsymbol{x}) \leq 1$) flows through a fixed discretization of the design domain in each optimization iteration. In other words, these densities are used to directly scale the stiffness of the material, known as the "Ersatz material" approach. $\rho = 1$ represents the solid material while $\rho_{min} = 1e^{-4}$ is the lower bound to avoid singularity of the stiffness matrix.

Using point-wise mapping to control an element-wise constant density distribution we have

$$\rho_e = (1 - \rho_{min})\widetilde{H}(\Phi(X_e)) + \rho_{min} \tag{9.61}$$

where X_e is the center of a finite element e. $\widetilde{H}(\Phi)$ is a smooth approximation of the Heaviside function defined by [Wang *et al.*, 2003]

$$\widetilde{H}(\Phi) = \begin{cases} 0 & for \quad \Phi < -h \\ -\frac{1}{4}\left(\frac{\Phi}{h}\right)^3 + \frac{3}{4}\left(\frac{\Phi}{h}\right) + \frac{1}{2} & for \quad -h \leq \Phi \leq h \\ 1 & for \quad h < \Phi \end{cases} \tag{9.62}$$

Having ρ, the volume integrals of some functional f over a material domain can then be defined as

$$\int_{\Omega} f dV = \int_{D} f\widetilde{H}(\Phi)dV \approx \int_{D} f\rho(\Phi)dV \tag{9.63}$$

Meanwhile ρ is embedded in the electromechanical problem as

$$M(x,y) = \rho(\Phi)M_0 \quad with \quad \boldsymbol{M_0} = \boldsymbol{C}, \boldsymbol{e}, \boldsymbol{\kappa}, \boldsymbol{\mu} \tag{9.64}$$

where $\boldsymbol{C}, \boldsymbol{e}, \boldsymbol{\kappa}$ and $\boldsymbol{\mu}$ denote elastic, piezoelectricity, permittivity and flexoelectricity tensors, respectively. Subscript 0 represents properties of the solid material.

The derivative of the density function with respect to the level set nodal values is obtained by

$$\frac{\partial \rho_e}{\partial \varphi_{i,j}} = (1 - \rho_{min})\widetilde{\delta}(\Phi(X_e))\frac{\partial \Phi(X_e)}{\partial \varphi_{i,j}} \tag{9.65}$$

where $\widetilde{\delta}(\Phi) = \frac{\partial \widetilde{H}}{\partial \Phi}$ is the approximate Dirac delta function defined by

$$\widetilde{\delta}(\Phi) = \begin{cases} \frac{3(1 - \rho_{min})}{4h}\left(1 - \left(\frac{\Phi}{h}\right)^2\right) & for -h \leq \Phi \leq h \\ 0 & otherwise \end{cases} \tag{9.66}$$

and $\frac{\partial \Phi(X_e)}{\partial \varphi_{i,j}}$ is calculated by

$$\frac{\partial \Phi(X_e)}{\partial \varphi_{i,j}} = R_{i,j}^{p,q}(\xi, \eta) \tag{9.67}$$

9.4.2 Optimization problem

The electromechanical coupling coefficient, c_{em}, is defined as

$$c_{em} = \frac{w_{elec}}{w_{mech}} \tag{9.68}$$

where w_{elec} and w_{mech} are the electrical and mechanical (or strain) energies, respectively. By extending w_{elec} and w_{mech} in Eq. (9.68) and defining the objective function, $J(\boldsymbol{u}(\boldsymbol{\varphi}), \boldsymbol{\theta}(\boldsymbol{\varphi}), \boldsymbol{\varphi})$, as the inverse of c_{em} we have

$$J(\boldsymbol{u}(\boldsymbol{\varphi}), \boldsymbol{\theta}(\boldsymbol{\varphi}), \boldsymbol{\varphi}) = \frac{1}{c_{em}} = \frac{w_{mech}}{w_{elec}} = \frac{\frac{1}{2}\int_{\Omega} \boldsymbol{\varepsilon}^T \boldsymbol{C} \boldsymbol{\varepsilon} d\Omega}{\frac{1}{2}\int_{\Omega} \boldsymbol{E}^T \boldsymbol{\kappa} \boldsymbol{E} d\Omega} \tag{9.69}$$

where $\boldsymbol{\varepsilon}$ and $\boldsymbol{E}$ are obtained according to Eqs. (9.38)- (9.39) and $\boldsymbol{\varphi}$ denotes the vector containing all $\varphi_{i,j}$. Eventually, the optimization problem can be summarized as follows

$$\begin{cases} Minimize : J(\boldsymbol{u}(\boldsymbol{\varphi}), \boldsymbol{\theta}(\boldsymbol{\varphi}), \boldsymbol{\varphi}) \\ S.t : \\ V_f = \int_D \rho(\Phi) dV = V_{f0} \\ \begin{bmatrix} \boldsymbol{A}_{UU} & \boldsymbol{A}_{U\theta} \\ \boldsymbol{A}_{\theta U} & \boldsymbol{A}_{\theta\theta} \end{bmatrix} \begin{bmatrix} \boldsymbol{U} \\ \theta \end{bmatrix} = \begin{bmatrix} \boldsymbol{f}_U \\ \boldsymbol{f}_\theta \end{bmatrix} \end{cases} \tag{9.70}$$

where V_f is the total volume in each optimization iteration; V_{f0} is an arbitrary volume which must be set at the beginning of the optimization process. By introducing a proper Lagrangian objective function, l, and Lagrange multiplier, Ψ, we obtain

$$l = J - \Psi(V_f - V_{f0}) \tag{9.71}$$

To find the minimum of l, the first derivatives of Eq. (9.71) with respect to $\boldsymbol{\varphi}$ is set as zero. So,

$$\frac{dl}{d\boldsymbol{\varphi}} = \frac{dJ}{d\boldsymbol{\varphi}} - \Psi\frac{dV_f}{d\boldsymbol{\varphi}} = 0 \tag{9.72}$$

To update the design variables, sensitivity analysis is required which is presented in Section 9.4.3.

9.4.3 Sensitivity analysis

To solve Eq. (9.72), one should differentiate the objective and constraint functions with respect to the design variables. Considering the coupled system of equations in residual form, we have

$$R(\boldsymbol{u}, \boldsymbol{\theta}) = 0 \tag{9.73}$$

$$H(\boldsymbol{u}, \boldsymbol{\theta}) = 0 \tag{9.74}$$

where R and H are residuals that must be simultaneously satisfied, and $\boldsymbol{u}$ and $\boldsymbol{\theta}$ are solution (i.e. displacement and electric potential) fields. By assembling Eq. (9.73) and Eq. (9.74) into a single global residual $\mathfrak{R}$ we have

$$\mathfrak{R}(\mathfrak{U}) = \begin{bmatrix} R(\boldsymbol{u}, \boldsymbol{\theta}) \\ H(\boldsymbol{u}, \boldsymbol{\theta}) \end{bmatrix} = \mathfrak{R}(\mathfrak{U}(\boldsymbol{\varphi}), \boldsymbol{\varphi}) = 0 \tag{9.75}$$

where

$$\mathfrak{U} = \begin{bmatrix} \boldsymbol{u} \\ \boldsymbol{\theta} \end{bmatrix} \tag{9.76}$$

Thus, the objective function takes the form $J(\mathfrak{U}(\boldsymbol{\varphi}), \boldsymbol{\varphi})$. Recalling Eq. (9.72), the chain-rule is used to calculate the sensitivity of $J(\mathfrak{U}(\boldsymbol{\varphi}), \boldsymbol{\varphi})$ with respect to $\boldsymbol{\varphi}$. Employing partial derivatives $(\frac{\partial (.)}{\partial (.)})$ we have

$$\frac{dJ}{d\boldsymbol{\varphi}} = \frac{\partial J}{\partial \mathfrak{U}} \frac{\partial \mathfrak{U}}{\partial \boldsymbol{\varphi}} + \frac{\partial J}{\partial \mathfrak{U}} \tag{9.77}$$

The last term of Eq. (9.77) is the explicit quantity and easy to calculate

$$\frac{\partial J}{\partial \boldsymbol{\varphi}} = \frac{1}{w_{elec}} \left(\frac{1}{2} \int_\Omega \boldsymbol{B}_u \boldsymbol{u}^T \frac{\partial \boldsymbol{C}}{\partial \boldsymbol{\varphi}} \boldsymbol{B}_u^T \boldsymbol{u} d\Omega \right) - \frac{w_{mech}}{w_{elec}^2} \left(\frac{1}{2} \int_\Omega \boldsymbol{B}_\theta \boldsymbol{\theta}^T \frac{\partial \boldsymbol{\kappa}}{\partial \boldsymbol{\varphi}} \boldsymbol{B}_\theta^T \boldsymbol{\theta} d\Omega \right) \tag{9.78}$$

while w_{elec} and w_{mech} are calculated according to Eq. (9.69); For plane strain problem

$$\frac{\partial \boldsymbol{C}}{\partial \boldsymbol{\varphi}} = \frac{\partial \rho_e}{\partial \boldsymbol{\varphi}} \left(\frac{Y}{(1+v)(1-2v)} \right) \begin{bmatrix} 1-v & v & 0 \\ v & 1-v & 0 \\ 0 & 0 & (\frac{1}{2}-v) \end{bmatrix} \tag{9.79}$$

and

$$\frac{\partial \boldsymbol{\kappa}}{\partial \boldsymbol{\varphi}} = \frac{\partial \rho_e}{\partial \boldsymbol{\varphi}} \begin{bmatrix} \kappa_{11} & 0 \\ 0 & \kappa_{33} \end{bmatrix} \tag{9.80}$$

To calculate $\frac{\partial \mathfrak{U}}{\partial \boldsymbol{\varphi}}$ as an implicit quantity, Eq. (9.73) is differentiated as

$$\left(\frac{\partial \mathfrak{R}}{\partial \mathfrak{U}} \right)^T \frac{\partial \mathfrak{U}}{\partial \boldsymbol{\varphi}} + \frac{\partial \mathfrak{R}}{\partial \boldsymbol{\varphi}} = \boldsymbol{0} \tag{9.81}$$

$$\frac{\partial \mathfrak{U}}{\partial \boldsymbol{\varphi}} = - \left(\frac{\partial \mathfrak{R}}{\partial \mathfrak{U}} \right)^{-T} \frac{\partial \mathfrak{R}}{\partial \boldsymbol{\varphi}} \tag{9.82}$$

substitution Eq. (9.82) into the first term of Eq. (9.77) right hand side yields

$$\frac{\partial J}{\partial \mathfrak{U}} \frac{\partial \mathfrak{U}}{\partial \varphi} = -\frac{\partial J}{\partial \mathfrak{U}} \left[\left(\frac{\partial \mathfrak{R}}{\partial \mathfrak{U}} \right)^{-T} \frac{\partial \mathfrak{R}}{\partial \varphi} \right] \tag{9.83}$$

assuming

$$\boldsymbol{\lambda} = -\frac{\partial J}{\partial \mathfrak{U}} \left(\frac{\partial \mathfrak{R}}{\partial \mathfrak{U}} \right)^{-T} \tag{9.84}$$

and knowing that $\frac{\partial \mathfrak{R}}{\partial \mathfrak{U}} = \boldsymbol{K}_{total}$, we can write

$$\boldsymbol{K}_{total}\boldsymbol{\lambda} = -\frac{\partial J}{\partial \mathfrak{U}} \tag{9.85}$$

$$\boldsymbol{K}_{total}\boldsymbol{\lambda} = -\frac{1}{w_{elec}} \int_{\Omega} \boldsymbol{B}_u \boldsymbol{C} \boldsymbol{B}_u^T \boldsymbol{u} d\Omega + \frac{w_{mech}}{w_{elec}^2} \int_{\Omega} \boldsymbol{B}_\theta \boldsymbol{\kappa} \boldsymbol{B}_\theta^T \boldsymbol{\theta} d\Omega \tag{9.86}$$

eventually, Eq. (9.83) can be written in the form

$$\frac{\partial J}{\partial \mathfrak{U}} \frac{\partial \mathfrak{U}}{\partial \varphi} = (\boldsymbol{\lambda})^T \frac{\partial \mathfrak{R}}{\partial \varphi} \tag{9.87}$$

$$\frac{\partial J}{\partial \mathfrak{U}} \frac{\partial \mathfrak{U}}{\partial \varphi} = \begin{bmatrix} \boldsymbol{A}'_{UU} & \boldsymbol{A}'_{U\theta} \\ \boldsymbol{A}'_{\theta U} & \boldsymbol{A}'_{\theta\theta} \end{bmatrix} [\boldsymbol{\lambda}] \tag{9.88}$$

$$\boldsymbol{A}'_{UU} = \int_{\Omega} \boldsymbol{u}^T \left(\boldsymbol{B}_u \frac{\partial \boldsymbol{C}}{\partial \boldsymbol{\varphi}} \boldsymbol{B}_u^T \right) d\Omega \tag{9.89}$$

$$\boldsymbol{A}'_{U\theta} = \int_{\Omega} \boldsymbol{u}^T \left(\boldsymbol{B}_u \frac{\partial \boldsymbol{e}}{\partial \boldsymbol{\varphi}} \boldsymbol{B}_\theta^T + \boldsymbol{H}_u \frac{\partial \boldsymbol{\mu}}{\partial \boldsymbol{\varphi}} \boldsymbol{B}_\theta^T \right) d\Omega \tag{9.90}$$

$$\boldsymbol{A}'_{\theta U} = \int_{\Omega} \boldsymbol{\theta}^T \left(\boldsymbol{B}_\theta \frac{\partial \boldsymbol{e}}{\partial \boldsymbol{\varphi}} \boldsymbol{B}_u^T + \boldsymbol{B}_\theta \frac{\partial \boldsymbol{\mu}}{\partial \boldsymbol{\varphi}} \boldsymbol{H}_u^T \right) d\Omega \tag{9.91}$$

$$\boldsymbol{A}'_{\theta\theta} = -\int_{\Omega} \boldsymbol{\theta}^T \left(\boldsymbol{B}_\theta \frac{\partial \boldsymbol{\kappa}}{\partial \boldsymbol{\varphi}} \boldsymbol{B}_\theta^T \right) d\Omega \tag{9.92}$$

where

$$\frac{\partial \boldsymbol{e}^T}{\partial \boldsymbol{\varphi}} = \frac{\partial \rho_e}{\partial \boldsymbol{\varphi}} \begin{bmatrix} 0 & 0 & e_{15} \\ e_{31} & e_{33} & 0 \end{bmatrix} \tag{9.93}$$

and

$$\frac{\partial \boldsymbol{\mu}}{\partial \boldsymbol{\varphi}} = \frac{\partial \rho_e}{\partial \boldsymbol{\varphi}} \begin{bmatrix} \mu_{11} & \mu_{12} & 0 & 0 & 0 & \mu_{44} \\ 0 & 0 & \mu_{44} & \mu_{12} & \mu_{11} & 0 \end{bmatrix} \tag{9.94}$$

and finally, for the last term of Eq. (9.72) we have

$$\frac{dV_f}{d\boldsymbol{\varphi}} = \frac{\partial V_f}{\partial \boldsymbol{\varphi}} = \int_{\Omega} \frac{\partial \rho_e}{\partial \boldsymbol{\varphi}} d\Omega \tag{9.95}$$

which is already obtained according to Eq. (9.65).

9.5 Numerical examples

In this section, firstly the analysis model is verified by comparing the results with some benchmark examples. The verified IGA model is then employed in the optimization algorithm to demonstrate its validity and usefulness. Isotropic linear elasticity under plane strain conditions is assumed in all examples. Commonly studied flexoelectric configurations (cantilever beam and truncated pyramid) with different electrical boundary conditions are solved. Electrodes are assumed as very thin deposited layers on the structures to impose equipotential boundary conditions, and have no contribution to the structural stiffness.

9.5.1 Verification of the IGA model

9.5.1.1 Cantilever beam (Mechanical loading)

Fig. 9.1(a) and Fig. 9.1(b) schematically represent the cantilever beam with mechanical and electrical boundary conditions. The model is discretized by 50×10 B-spline elements of order 3. The red dots represent the control points as shown in Fig. 9.1(c). Material properties of $BaTiO_3$ and loading data as listed in Table 9.1 are considered based on [Abdollahi *et al.*, 2014].
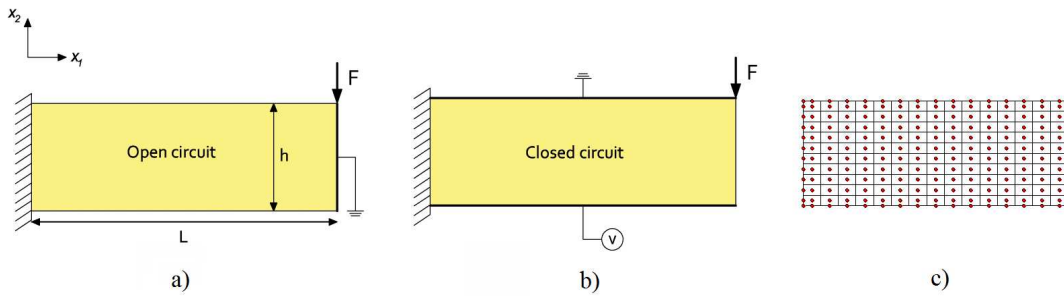
Figure 9.1: Electromechanical boundary conditions for open circuit (a) and closed circuit (b), FE discretization with red dots representing the control points (c)

Table 9.1: The cantilever beam problem: material properties, geometry and load data

L/h	υ	Y	e_{31}	μ_{12}	κ_{11}	κ_{33}	χ_{33}	F
20	0.37	100 GPa	-4.4 C/m^2	1 $\mu C/m$	11 nC/Vm	12.48 nC/Vm	1408	100 μN

$\frac{L}{h}$: *beam aspect ratio*, υ : *Poisson' ratio*, Y : *Young's modulus*, e_{31} : *piezoelectric constant*, μ_{12} : *flexoelectric constant*, κ_{11} *and* κ_{33} : *dielectric constants*, χ_{33} : *electric susceptibility*, F : *point load*

Following the terminologies of the benchmark examples [Abdollahi *et al.*, 2014], the electromechanical coupling factor is defined by

$$k_{eff}^2 = \frac{w_{elec}}{w_{mech}} \tag{9.96}$$

Assuming that the only non-zero components of the stress is σ_{11} and of the electric field is E_2, for one-dimensional coupling, Eq. (9.96) is analytically estimated in [Majdoub *et al.*, 2009] as

$$k_{eff} = \frac{\chi}{1+\chi}\sqrt{\frac{k}{Y}\left(e^2 + 12\left(\frac{\mu}{h}\right)^2\right)} \qquad (9.97)$$

where the normalized effective piezoelectric constant is

$$e^{'} = \frac{k_{eff}}{k_{piezo}} \qquad (9.98)$$

where k_{piezo} is obtained by neglecting flexoelectricity ($\mu = 0$) in Eq. (9.96).

To numerically simulate a 1-D coupling, the model is simplified by setting Poisson's ratio as well as all piezoelectric and flexoelectric constants to zero except e_{31} and μ_{12} which take the corresponding values of Table 9.1. Fig. 9.2 compares the results of the present and the analytical methods for both piezoelectric and non-piezoelectric materials. Here $h^{'}$ is the normalized beam thickness and for the open circuit condition is obtained by $h^{'} = -eh/\mu$. The non-piezoelectric materials are also obtained by setting $e_{31} = 0$. Fig. 9.2 illustrates that when the thickness of the beam decreases, the electromechanical response of the beam increases. This enhancement in electromechanical response at small length scales has also been observed for non-piezoelectric materials. Furthermore, as expected the flexoelectric effect vanishes for larger beam thicknesses. Overall, one can observe excellent agreement between the results of the current method and the analytical solutions.
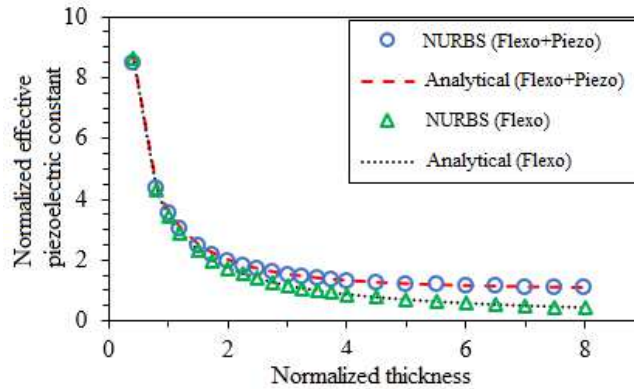
Figure 9.2: Normalized effective piezoelectric constant $e^{'}$ versus normalized beam thickness $h^{'}$. Graphs are for open circuit conditions and contain both piezoelectric and non-piezoelectric materials. The results for analytic solutions are reproduced according to Eq. (9.97).

9.5.1.2 Cantilever beam (Electrical loading)

For the next example a cantilever beam acting as an electromechanical actuator is studied. The beam is 50 μm long, 2.5 μm high, is made of non-piezoelectric material and has the closed circuit configuration as illustrated in Fig. 9.1. A voltage V equal to -20 MV is applied to the bottom edge while the top edge is grounded. The mechanical point load, F, is also set to zero. For above settings, the only phenomenon that deforms the beam is flexoelectricity, which acts as a result of polarization gradients. To demonstrate this, the distribution of the electric field across the beam thickness at the mid length of the beam is graphed in Fig. 9.3. It is observed that the results are slightly dependent on the order of the basis functions. In particular, larger gradients near the surfaces are obtained with increasing basis functions order. The present results, which are converged on a sufficiently fine discretization, are in good agreement with the benchmark example [Abdollahi *et al.*, 2014] from both values and field distribution points of view. All graphs clearly represent the high gradients at the top and bottom surfaces of the beam, which generate mechanical stresses and eventually deform the beam. The electric field is represented more smoothly away from the surfaces using higher orders basis functions.
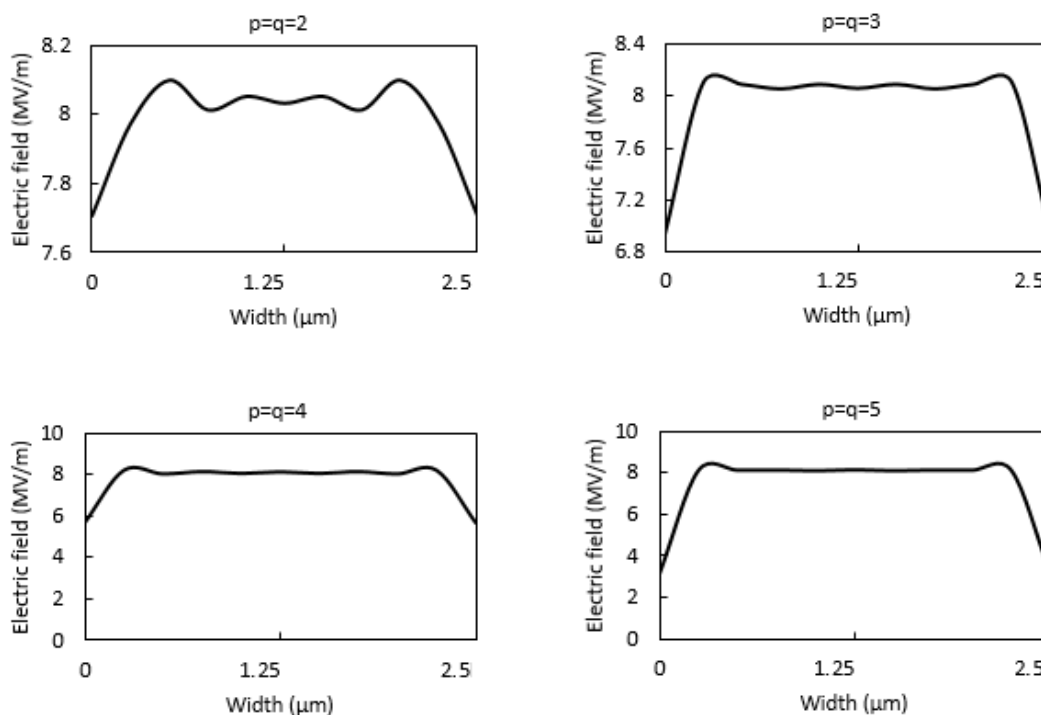
Figure 9.3: Distribution of electric field across the beam thickness for different orders of basis functions. p and q are order of basis functions in direction of length and width of the beam, respectively

9.5.1.3 Truncated pyramid

For the next example the flexoelectric effect in a truncated pyramid under compression is investigated. This geometry has been widely studied in flexoelectricity [Zhu et al., 2006] because of the intrinsic generation of strain gradients due to the different widths of the top and bottom surfaces. A uniformly distributed force of magnitude F is applied on the top edge while the bottom edge is mechanically fixed. The problem configuration and its FE discretization are shown in Fig. 9.4. The material parameters are according to Table 9.1 while the other design parameters are listed in Table 9.2.

Table 9.2: The truncated pyramid problem: geometry and load data

a_1	a_2	h	F
$750\mu m$	$2250\mu m$	$750\mu m$	$6\frac{N}{\mu m}$
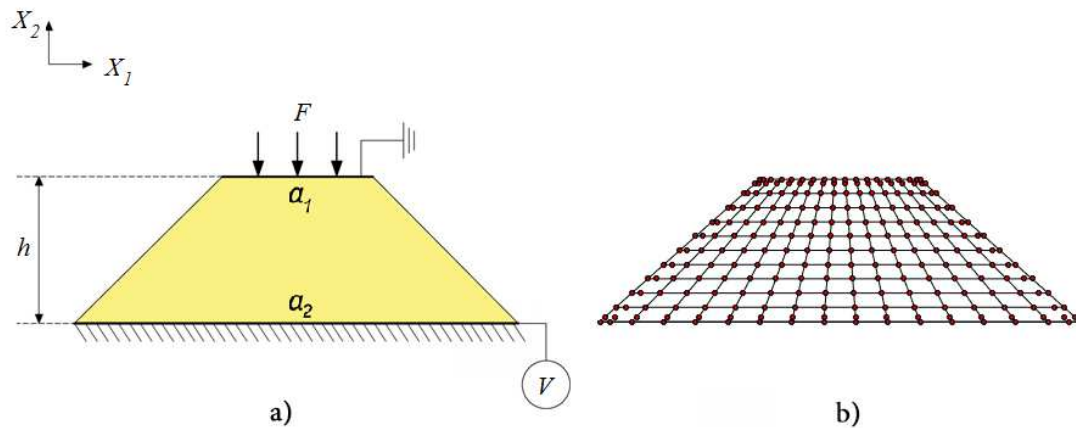
Figure 9.4: Truncated pyramid under compression, problem setup (a) FE discretization (b)

Fig. 9.5 shows the distribution of the electric potential (left) and the resulted strain in Y direction, ε_{22}, (right). Once again there is an acceptable agreement, in both patterns and values, between the results of the present method and [Abdollahi et al., 2014].

9.5.2 Topology optimization of the flexoelectric beam

Since there is no benchmark topology optimization example available for flexoelectricity, the methodology is verified for an elastic cantilever beam subjected to a mechanical load [Shojaee et al., 2012]. This is done by setting all the electrical parameters to zero. A cantilever beam of length 60 μm with an aspect ratio (defined by the beam length over its height) of 7 is considered. It is made of non-piezoelectric material $(e_{31} = 0)$
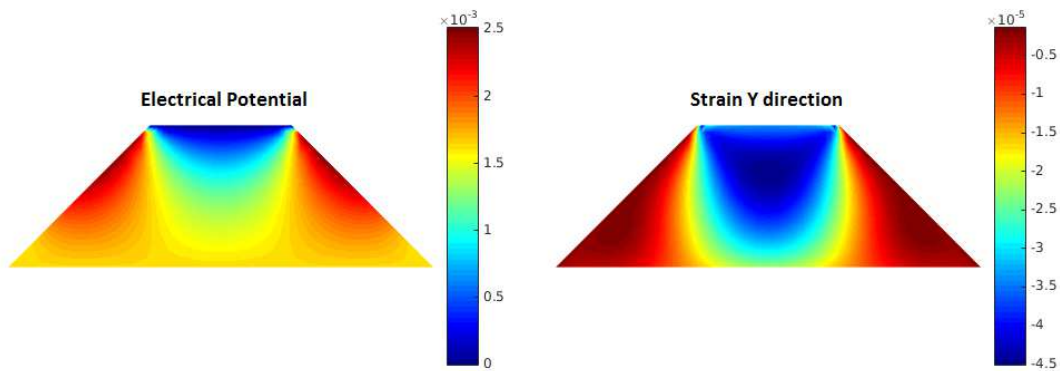
Figure 9.5: Distribution of the electric potential (left) and strain in Y direction, ε_{22} (right)

with open circuit boundary conditions. The loading and other material constants are according to Table 9.1. Fig. 9.6(a-c) show the initial (9.6(a)) and the optimized (9.6(b)) topologies constrained by 70% of the solid beam volume as the design limit. To un-
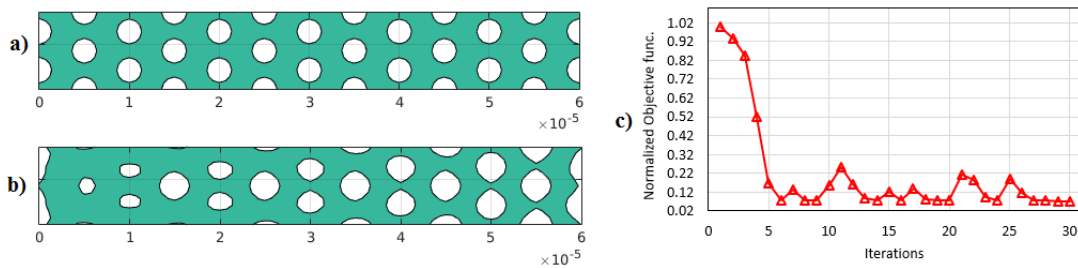
Figure 9.6: Initial (a) and the optimized (b) topologies considering 70% of the solid beam volume as design constraint. Normalized objective function versus iterations is plotted in (c). The beam is made of non-piezoelectric material with open circuit boundary conditions. The length of the beam is 60 μm with aspect ratio of 7.

derstand the optimum topology seen in Fig. 9.6(b), it is noteworthy to mention that for flexoelectric materials, electric polarization displays a linear relationship to the gradient of mechanical strain (see Eq. (9.2)) while for piezoelectric materials, the electric polarization and the mechanical strain are interrelated (see Eq. (9.1)). Thus, for flexoelectric structures, recognizing the zones with high strain gradients in the structure is the key to interpret the optimal topology. In Fig. 9.6(b) it is observed that more material is available in the left half (including fixed edge) of the structure (where the strain and strain gradients are higher) rather than the right half (including free edge). Within the left half, the material is also more available in top and bottom edges rather than the central part of the beam, for the same reason. The shape of the fixed edge is also in line with more electrical energy generation, as more detailed investigations

have shown that material reduction along the fixed edge will increase the generated electrical energy. Thus overall, the optimized geometry is in line with maximizing the electromechanical coupling coefficient which is equivalent to minimizing the objective function. The history of the objective function, which converges towards the minimum value, is presented in Fig. 9.6(c).

Let's define c_{em}^{sld} and c_{em}^{opt} as parameters that define the electromechanical coupling coefficients of the solid and optimized structures, respectively. In this case $c_{em}^{sld} = 4.75e^{-5}$ and $c_{em}^{opt} = 315e^{-5}$ and their ratio, $c_{em}^N = \frac{c_{em}^{opt}}{c_{em}^{sld}} = 66.32$, is the normalized electromechanical coupling coefficient. That would be a reasonable argument that such an increase in energy conversion is partially due to 30% decrease in structural volume; It should be noted that the electromechanical coupling coefficient for the initial structure (Fig. 9.6(a)), c_{em}^{ini}, which have nearly the same volume as the optimized structure (i.e. 70% of the solid beam volume), is equal to $22.5e^{-5}$. By comparison of these numbers ($\frac{c_{em}^{opt}}{c_{em}^{ini}} = 14$) we can determine how significant the role of topology optimization in increasing c_{em} is. The similar analysis for different beam aspect ratios are performed and the results are plotted in Fig. 9.7. It is observable that, the higher aspect ratio, the higher c_{em}^N is obtained. It means topology optimization shows profound advantages in higher aspect ratios.
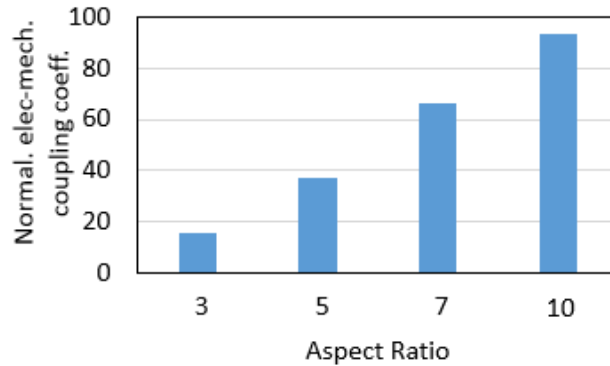
Figure 9.7: c_{em}^N versus beam aspect ratio. c_{em}^N is the ratio of the electromechanical coupling coefficients of the optimized structure to the solid structure. For all cases, the length of the beam is 60 μm and the optimized topology has 70% of the solid beam volume.

The flexoelectric truncated pyramid under a 10 μN point load applied at the midpoint of the top edge is considered as the next example. Other design parameters and dimensions are listed in Table 9.1 and Table 9.2 considering 70% of the solid truncated pyramid volume as design constraint. Boundary conditions are according to Fig. 9.4. The optimized topology is shown in (Fig. 9.8(a)). The region with high strain gradients is located underneath the point load where the crown shape topology increases the

strain gradients and consequently, the generated electrical energy. It is also observable that the length of the top edge has shortened, which also causes larger strain gradients. The graph related to the history of the normalized objective function (Fig. 9.8(b)) and the graph for structural volume (Fig. 9.8(c)) converge relatively smoothly. The small jumps in graph of Fig. 9.8(b) at iterations 10, 20, 30 and 40 are related to re-initialization in optimization process. For this example $\frac{c_{em}^{opt}}{c_{em}^{ini}} = 2.47$ which shows again the impact of topology optimization on enhancing electromechanical behavior of dielectric solids possessing flexoelectric effect.
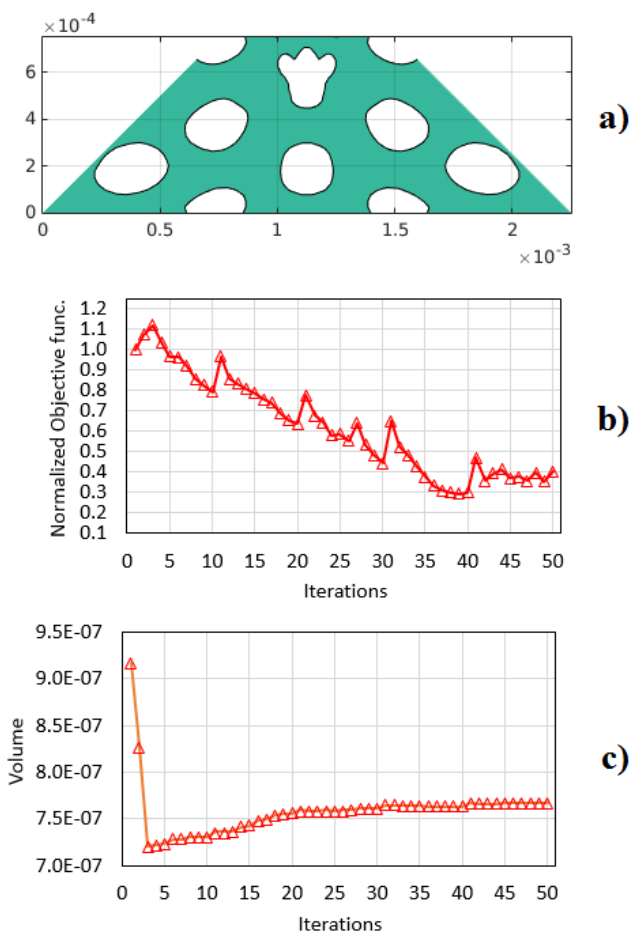
Figure 9.8: The optimized topology (a) considering 70% of the solid truncated pyramid volume as design constraint. The normalized objective function versus iterations is plotted in (b) and the volume history is shown in (c). The pyramid is made of non-piezoelectric material under a $10\mu N$ point load at mid of the top edge. The other design parameters listed in Table 9.1 and Table 9.2. The boundary conditions are shown in Fig. 9.4.

9.6   Concluding remarks

A computational framework for topology optimization of flexoelectric micro and nanostructures is presented to enhance their energy conversion efficiency. The methodology is based on a combination of isogeometric analysis (IGA), level set and point wise density mapping techniques. The smoothness of the IGA basis functions is used to discretize the fourth order partial differential equations of flexoelectricity, while the level set provide clear boundaries and gives stable convergence. The point wise density mapping is directly used in the weak form of the governing equations and its derivative can be consistently derived. The nodal level set values on control points and the inverse of the electromechanical coupling coefficient are defined as design variables and objective function, respectively. The numerical results demonstrate that B-spline elements can successfully model the flexoelectric effect in dielectrics. For a cantilever beam with constant length, it is shown that when the thickness of the beam decreases, the electromechanical response increases. The topology optimization is also able to noticeably increase the electromechanical coupling coefficient, with substantial enhancements observed for higher aspect ratios.

Chapter 10

Conclusions

10.1   Summary of achievements

The methodology and achievements of this research work are highlighted within following four items:

1. Fiber distribution optimization:
   An efficient gradient based computational technique for fiber distribution optimization in fiber reinforced continuum elements, has been developed through the use of Non-Uniform Rational B-spline (NURBS) functions. Nodal volume fraction of fiber has been used as the optimization design variable, whose distribution function has been smoothly approximated by using a NURBS surface. The methodology allows considering different material models and generic objective functions. The main advantage of the proposed approach is that domain discretization and definition of fiber distribution function have common data sets. It also allows to get a high rate and smooth convergence to the optimum condition sought.

2. Uncertainties propagation:
   Deterministic approaches for nanocomposite modeling and optimization might be unrealistic for certain applications and may yield to either catastrophic failure or unnecessary conservatism. Detailed investigations on uncertainties and their propagation have been performed for obtaining realistic and reliable Polymeric Nano Composite (PNC) structures. Potential uncertainties have been categorized in material, structural and modeling levels. To fully address uncertainties in material level, a stochastic multi-scale material model (which includes all important aspects of the Carbon Nano Tube Reinforced Polymer (CNTRP) including CNT length, orientation, dispersion, agglomeration and waviness, at different length scales from nano-, up to macro-scale) has been utilized. To improve the compu-

tational efficiency, the evaluation of material properties has been surrogated by a metamodel. The results for two selected examples show that the failure probability of a polymeric nanocomposite structure, strongly depends on the CNT parameters, especially the CNT volume fraction and the waviness. The influence of the CNT agglomeration is nearly negligible. It was observed that neglecting the CNT agglomeration can simplify the model and decrease the computational time without remarkable loss in model accuracy. Furthermore, the loading condition and discretization affect the reliability of the system. Coarse meshes underestimate the failure probability of a beam while fine meshes admittedly increase computational cost. Thus sufficiently refined discretization should be investigated in order to have realistic assessment of the reliability of PNC structures. An increase in the standard deviation of the applied load, which physically means more uncertainties in the system, resulted in the structure with a smaller reliability index. Finding the optimal content of CNT was also presented to optimized the material instead of the geometry. As a further step forward, concurrent optimization of material parameters and geometrical parameters (hybrid optimization) was conducted to present a comprehensive solution for current demands in fully optimized designs of nanocomposite components.

3. Sequential optimization approach:
The two previous items are integrated resulted in an efficient sequential algorithm for finding the optimal fiber volume fraction and its distribution in structures made of Fiber Reinforced Composite (FRC) materials. To overcome the cumbersome computational burden in stochastic optimization problems, finding the optimal fiber volume fraction and fiber distribution are performed sequentially, not concurrently. This technique along with using NURBS finite elements, allows us to get a noticeable reduction in the computational cost, without a noticeable loss in accuracy of the results. Assuming a (simplified energy-based material model) random orientation of fibers in the matrix, in the first optimization module (i.e. finding the optimal fiber volume fraction) uncertainties in the parameters (such as constituents materials and loading) are fully addressed and Limit State Function (LSF) is evaluated by using First Order Reliability Method (FORM). In the second module (i.e. fiber distribution optimization) a NURBS surface which smoothly defines the fiber distribution pattern, is adopted. The presented numerical examples show as an increase in model uncertainties gives rise to unreliability of the system. More specifically, either the rise in the number of uncertain fields in the problem or the increase in the standard deviation of random variables needs more fiber content. It can be also concluded that when there is a higher level of uncertainties in design parameters, the fiber distribution optimization is more influential on increasing the reliability of the structure.

4. Innovative applications:

The methodology is applied in three novel applications with following achievements / observations:

- Interfacial shear stress optimization in sandwich beams:
  A computational algorithm for decreasing interfacial shear stress in sandwich beams with polymeric core is presented. The algorithm can be also used for optimizing other stress components (i.e. peeling and bending stresses) in any arbitrary zone of the design domain. C^{-1} continuity is imposed at the interface to "truly" isolate the reinforcement distribution in the core from the face sheets using multi-patch and penalty techniques. Comparing the results of the case study illustrates that adding reinforcements homogeneously into polymers will slightly improve the interfacial shear stress but that considerable improvements are observed when the distribution of the reinforcement in the core is optimized.

- Probabilistic multiconstraints optimization of cooling channels in Ceramic Matrix Composites (CMC):
  The presented computational platform efficiently optimizes the capacity of cooling channels in a components made of CMC using Reliability Based Design Optimization (RBDO) approach. A "series system" reliability concept is adopted as a union of mechanical and thermal failure subsets. Afterwards, the optimizer is supposed to increase the reliability of the component by optimally distributing the C-fibers inside the matrix within the design domain. Numerical results for the performed case studies demonstrate that optimal distribution of C-fibers can decrease structural and thermal compliances. In the decoupled elastic and thermal problems, the former yields an increase in β_m (the reliability index associated with the probabilistic deformation constraint) and the latter in an increase in β_t (the reliability index associated with the probabilistic thermal constraint). But, in the coupled thermoelastic problem, any prediction about final reliability indices depends on fiber and matrix constitutive material properties and contribution of mechanical and thermal loadings on the global force vector. When the mechanical loading dominates the thermal loading, fiber distribution can show promising advantage to have more reliable design by increasing β_m and consequently β_{target} (the final reliability index). However, its role for increasing the reliability index corresponding to thermal constraint is negligible.

- Topology optimization of flexoelectric materials:
  A computational framework for topology optimization of flexoelectric micro and nanostructures is presented to enhance their energy conversion efficiency. The methodology is based on a combination of isogeometric analysis (IGA), level set and point wise density mapping techniques. The smoothness of the IGA basis functions is used to discretize the fourth order partial differ-

ential equations of flexoelectricity, while the level set provide clear boundaries and gives stable convergence. The point wise density mapping is directly used in the weak form of the governing equations and its derivative can be consistently derived. The nodal level set values on control points and the inverse of the electromechanical coupling coefficient are defined as design variables and objective function, respectively. The numerical results demonstrate that B-spline elements can successfully model the flexoelectric effect in dielectrics. For a cantilever beam with constant length, it is shown that when the thickness of the beam decreases, the electromechanical response increases. The topology optimization is also able to noticeably increase the electromechanical coupling coefficient, with substantial enhancements observed for higher aspect ratios.

10.2   Outlook

The presented work established the framework for probabilistic optimization of fiber reinforced composites with some promising applications. It is also extended and used as a topology optimization tool for flexoelectric micro-nano devices. A few possible extensions to the current work can be suggested as follows:

- Extend the methodology to 3-D to be able to address more general problems

- Investigate different failure criteria as limit state functions

- Contributing the developed methodology towards the design of micro and nanoscale energy harvesters / sensors with optimized electromechanical performance

- Addressing the available uncertainties in optimization of micro-nano electromechanical devices

- Contributing towards the design of multi-material micro and nano-scale energy harvesters / sensors

Bibliography

Abdollahi, Amir, Peco, Christian, Millan, Daniel, Arroyo, Marino, & Arias, Irene. 2014. Computational evaluation of the flexoelectric effect in dielectric solids. *JOURNAL OF APPLIED PHYSICS*, **116**, 093502. 108, 109, 120, 122, 123

Abdollahi, Amir, Millan, Daniel, Peco, Christian, Arroyo, Marino, & Arias, Irene. 2015. Revisiting pyramid compression to quantify flexoelectricity: A three-dimensional simulation study. *PHYSICAL REVIEW B*, **91**, 104103. 108

Ahmadpour, F., & Sharma, P. 2015. Flexoelectricity in two-dimensional crystalline and biological membranes. *nanoscale*, **7**, 16555–16570. 107

Almeida, F.S., & Awruch, A.M. 2009. Design optimization of composite laminated structures using genetic algorithms and finite element analysis. *Compos. Struct.*, **88**, 443–454. 3

Antonio, C. C., & Hoffbauer, L. N. 2009. An approach for reliability-based robust design optimization of angle-ply composites. *Compos. Struct.*, **90**, 53–59. 4

Apalak, M. Kemal, & Yildirim, Mustafa. 2008. Layer optimization for maximum fundamental frequency of laminated composite plates for different edge conditions. *Compos. Struct.*, **68**, 537–550. 3

Bendse, M. P., & Kikuchi, N. 1988. Generating Optimal Topologies in Structural Design using a Homogenization Method. *Computer Methods in Applied Mechanics and Engineering*, **71**. 108

Bendsoe, MP., & Sigmund, O. 2003. *Topology optimization:Theory, Methods, and Applications*. Germany: Springer. 72

Bourinet, J.-M. 2010. FERUM 4.1 user's guide. *available online at: http://www.ifma.fr/cache/offonce/lang*. 16, 42, 92

Brighenti, R. 2004a. A mechanical model for fiber reinforced composite materials with elasto-plastic matrix and interface debonding. *Int. J. Comput. Mater. Sci.*, **29**, 475–493. 18, 19

Brighenti, R. 2004b. Numerical modeling of the fatigue behavior of fiber-reinforced composites. *Int. J. Compos. B: Eng.*, **35**. 19

Brighenti, R. 2004c. Optimum patch repair shapes for cracked members. *Int. J. Mech. Mater. Des.*, **1**. 3

Brighenti, R. 2005. Fiber distribution optimization in fiber-reinforced composites by a genetic algorithm. *Compos. Struct.*, **71**, 1–15. viii, 2, 3, 17, 27, 28

Brighenti, R. 2007. Patch repair design optimization for fracture and fatigue improvements of cracked plates. *J. Sol. Struct.*, **44**. 3

Brighenti, R. 2012. *A micromechanical model and reinforcing distribution optimization approach for fiber-reinforced materials. In: Qingzheng (George) Cheng (ed) Fiber Reinforced Composites*. Hauppauge, NY: Nova Science Publishers, Inc. viii, 19, 20

Brighenti, R., & Scorza, D. 2012. A micro-mechanical model for statistically unidirectional and randomly distributed fiber-reinforced solids. *Math. Mech. Solids*, **17**. 21

Brighenti, R., Carpinteri, A., & Vantadori, S.A. 2006. genetic algorithm applied to optimization of patch repairs for cracked plates. *Comp. Meth. App. Mech. Eng.*, **1960**, 466–475. 3

Bui, TQ., Kosravifard, A., Zhang, CH., Hematiyan, Mr., & Golub, MV. 2013. Dynamic analysis of sandwich beam with functionally graded core using a truly meshfree radial point interpolation method. *Eng. struct.*, **47**, 90–104. x, 66, 67, 77

Cai, Y., Zhuang, X., & Zhu, H. 2013. A generalized and efficient method for finite cover generation in the numerical manifold method. *Int. J. of Comput. Methods*, **10**. 68

Chiachio, M., Chiachio, J., & Rus, G. 2012. Reliability in composites - A selective review and survey of current development. *Composites*, **43**. 14

Cottrell, J.A., Hughes, T.J.R., & Bazilevs, Y. 2009. *Isogeometric Analysis towards integration of CAD and FEA*. UK: Wiley. 8, 9, 10, 71

Dennis, B., Egorov, I., Dulikravich, G., & Yoshimura, S. 2003. Optimization of a large number of coolant passages located close to the surface of a turbine blade. *In: Proceedings of ASME Turbo Expo 2003, Power for Land, Sea and Air Conference. Atlanta, Georgia, June 16-19*. 86

Ditlevsen, O., & Madsen, H. 1996. *Structural reliability methods*. UK: John Wiley Sons. 12

Du, J., & Olhoff, N. 2007. Topological design for freely vibrating continuum structures for maximum values of simple and multiple eigenfrequencies and frequency gaps. *Struct. Multidisc. Opt.*, **34**, 91–110. 21

Duddu, R., Bordas, SPA., Chopp, D., & Moran, B. 2008. A combined extended finite element and level set method for biofilm growth. *Int. J. Numer. Meth. Engng.*, **74**. 68

Ghorashi, SS., Valizadeh, N., & Mohammadi, S. 2012. Extended isogeometric analysis for simulation of stationary and propagating cracks. *Int. J. Numer. Meth. Engng.*, **89**, 1069–1101. 68

Gomes, H.M., & Awruch, A.M. 2011. Reliability based optimization of laminated composite structures using genetic algorithms and Artificial Neural Networks. *Struct. saf.*, **33**, 186–195. 4

Hashin, Z. 1962. The elastic moduli of heterogeneous materials. *J Appl. Mech.*, **29**, 143–150. 18

Hashin, Z., & Shtrikman, S. 1963. A variational approach to the theory of elastic behavior of multiphase materials. *J. Mech. Phys. Solids*, **11**, 127–140. 18

Hasofer, A.M., & Lind, N. 1974. An Exact and Invariant First-Order Reliability Format. *J. Eng. Mech. ASCE*, **100**, 111–121. 12

Hill, R. 1965. A self-consistent mechanics of composite materials. *J. Mech. Phys. Solids*, **13**, 213–222. 18

Honda, Shinya, & Narita, Yoshihiro. 2011. Vibration design of laminated fibrous composite plates with local anisotropy induced by short fibers and curvilinear fibers. *Compos. Struct.*, **93**, 902–910. 3

Hu, H., Belouettar, S., Ferry, MP., & Daya, EM. 2008. Review and assessment of various theories for modeling sandwich composites. *Compos. Struct.*, **84**, 282–292. 65

Huang, J., & Haftka, R.T. 2005. Optimization of fiber orientations near a hole for increased load-carrying capacity of composite laminates. *Struct. Multidisc. Optim.*, **30**, 335–341. 3

Hughes, TJR., Cottrell, JA., & Bazilevs, Y. 2005. Isogeometric Analysis: CAD, finite elements, NURBS, exact geometry and mesh refinement. *Comput. Methods Appl. Mech. Eng.*, **194**, 4135–4195. 8

Jha, DK., Kant, T., & Singh, RK. 2013. A critical review of recent research on functionally graded plates. *Compos. Struct.*, **96**, 833–849. 65

Jia, Y., Anitescu, C., Ghorashi, SS., & Rabczuk, T. 2014. Extended isogeometric analysis for material interface problems. *IMA J. of Appl. Math.* 68

Jiang, C., Han, X., & Liu, G.P. 2008. Uncertain optimization of composite laminated plates using a nonlinear interval number programming method. *Comput. and struct.*, **86**, 1696–1703. 4

Kim, Taeseong, & Lim, Jaehoon. 2013. Structural design optimization of a tiltrotor aircraft composite wing to enhance whirl flutter stability. *Compos. Struct.*, **95**, 283–294. 3

Krenkel, W. 2005. *Carbon fiber reinforced Silicon Carbide composites (C/SIC, C/C-SIC). In: Bansal Narottam P, editor. Hand book of ceramic composites*. US: Springer. 86

Krour, B., Bernard, F., & Tounsi, A. 2013. Fibers orientation optimization for concrete beam strengthened with a CFRP bonded plate: A coupled analyticalnumerical investigation. *Eng. struct.*, **56**, 218–227. 65

Kulasegaram, S., & Karihaloo, B.L. 2012. Fibre-reinforced, self-compacting concrete flow modelled by smooth particle hydrodynamics. *Proc. ICE Eng. Comput. Mech.*, **166**. 3

Kulasegaram, S., Karihaloo, B.L., & Ghanbari, A. 2011. Modelling the flow of self-compacting concrete, International Journal for Numerical and Analytical Methods in Geomechanics. *Int. J. Numer. Anal. Meth. Geomech.*, **35**. 3

Lau, K.T., Gu, C., & Hui, D. 2006. A critical review on nanotube and nanotube/nanoclay related polymer composite materials. *Compos: Part B-Eng.*, **37**, 425–436. 35

Lee, D.S., & Morillo, C. 2012. Multilayered composite structure design optimization using distributed/parallel multi-objective evolutionary algorithms. *Compos. Struct.*, **94**, 1087–1096. 3

Lee, Gyeong-Chan, & Kweon, Jin-Hwe. 2013. Optimization of composite sandwich cylinders for underwater vehicle application. *Compos. Struct.*, **96**, 691–697. 3

Liu, GR., Wang, Z., Zhang, GY., Zong, Z., & Wang, S. 2012. An Edge-Based Smoothed Point Interpolation Method for Material Discontinuity. *Mech. of Adv. Mater. and Struct.*, **19**. 76

Logan, DL. 2007. *A first course in the finite element method*. CA: Nelson. 90

Lophaven, S.N., Nielsen, H.B., & Sondergaard, J. 2002. DACE a Matlab kriging toolbox version 2.0, Technical Report IMM-TR-2002-12. *Informatics and mathematical modeling*. 39, 41

Lousdad, A., Megueni, A., & Bouchikhi, AS. 2010. Geometric edge shape based optimization for interfacial shear stress reduction in fiber reinforced polymer plate retrofitted concrete beams. *Comput. mat. sci.*, **47**, 911–918. 65

Majdoub, M. S., Sharma, P., & Cagin, T. 2009. Enhanced size-dependent piezoelectricity and elasticity in nanostructures due to the flexoelectric effect. *PHYSICAL REVIEW B*, **79**, 119904 (E). 108, 114, 121

Manalo, AC, Aravinthan, T., & Karunasena, W. 2009. Flexural behavior of laminated fiber composite sandwich beams. *Proceedings of the second official international conference of international institute for FRP in construction for Asia-Pacific region, Seoul*, 407–412. 65

Marler, R.T., & Arora, J.S. 2004. Survay of multi-objective optimization methods for engineering. *Struct. Multidisc. Opt.*, **26**, 369–395. 21

Mashkevich, V. S., & Tolpygo, K. B. 1957. Electrical, optical and elastic properties of diamond crystals. *Soviet Physics*, **5**. 107

Mori, T., & Tanaka, K. 1973. Average stress in matrix and average elastic energy of materials with mis-fitting inclusions. *Acta Metal*, **21**, 571–583. 18, 38, 66, 67

Murugan, Senthil, & Flores, Erick I. Saavedra. 2012. Optimal design of variable fiber spacing composites for morphing aircraft skins. *Compos. Struct.*, **94**, 1626–1633. 3

Nadeau, J.C., & Ferrari, M. 1999. Microstructural optimization of a functionally graded transversely isotropic layer. *Mechanics of Materials*, **31**, 637–651. 3

Nagaiah, NR:, & Geiger, CD. 2014. Evolutionary numerical simulation approach for design optimization of gas turbine blade cooling channels. *Int. J. Simul. Multisci. Des. Optim.*, **5**, A22. 86

Nanthakumar, S., Lahmer, T., & Rabczuk, T. 2013. Detection of flaws in piezoelectric structures using XFEM. *International Journal of Numerical Methods in Engineering*, **96**. 107

Nanthakumar, S., Lahmer, T., & Rabczuk, T. 2014. Detection of multiple flaws in piezoelectric structures using XFEM and Level sets. *Computer Methods in Applied Mechanics and Engineering*, **275**, 98–112. 107

Nanthakumar, S., Valizadeh, N., Park, Harold S., & Rabczuk, T. 2015. Surface effects on shape and topology optimization of nanostructures. *Comput Mech*, **56**, 97–112. 108

Nanthakumar, S., Lahmer, T., Zhuang, X., Zi, G., & Rabczuk, T. 2016. Detection of material interfaces using a regularized level set method in piezoelectric structures. *Inverse Problems in Science and Engineering*, **24**. 107

Nguyen, T. D., Mao, S., Yeh, Y-W, Purohit, P. K., & McAlpine, M. C. 2013. Nanoscale flexoelectricity. *Adv. Mater.*, **25**, 946–74. 108

Nguyen, VP., Kerfriden, P., & Bordas, SPA. 2014. Two- and three-dimensional isogeometric cohesive elements for composite delamination analysis. *Compos. Part B: Eng.*, **60**, 193–212. 68

Nguyen, VP., Anitescu, Cosmin, Rabczuk, T., & Bordas, SPA. 2015. Isogeometric analysis: An overview and computer implementation aspects. *Math. and Comput. in Simul.*, **117**, 89–116. 76

Nikolaidis, E., Ghiocel, DM., & Singhal, S. 2005. *Engineering design reliability handbook*. US: CRC Press. 91, 92

Noh, Y.J., & Kang., Y.J. 2013. Reliability-based design optimization of volume fraction distribution in functionally graded composites. *Comp. Mater. Sci.*, **69**, 435–442. 4

Omkar, S.N., & Mudigere, Dheevatsa. 2008. Vector evaluated particle swarm optimization (VEPSO) for multi-objective design optimization of composite structures. *Comput. Struct.*, **86**, 1–14. 3

Osher, S., & Sethian, J.A. 1988. Front propagating with curvature dependent speed: algorithms based on Hamilton-jacobi formulations. *J. Comp. Physics*, **78**, 12–49. 108

Park, Hong-Seok, & Dang, Xuan-Phuong. 2010. Structural optimization based on CAD-CAE integration and metamodeling techniques. *Comput. Aided Des.*, **42**, 889–902. 39

Paul, B. 1960. Prediction of elastic constants of multiphase materials. *Trans. Metall. Soc. AIME*, 36–41. 18

Rabczuk, T., & Belytschko, T. 2004. Particles: a simplified meshfree method for arbitrary evolving cracks. *Int. J. Numer. Meth. Engng.*, **61**, 2316–2343. 68

Rabczuk, T., & Belytschko, T. 2007. A three-dimensional large deformation meshfree method for arbitrary evolving cracks. *Comput. Methods Appl. Mech. Eng.*, **196**, 2777–2799. 68

Rabczuk, T., Areias, P., & Belytschko, T. 2007. A meshfree thin shell method for non-linear dynamic fracture. *Int. J. Numer. Meth. Engng.*, **72**. 68

Rouhi, M., & Rais-Rohani, M. 2013. Modeling and probabilistic design optimization of a nanofiber-enhanced composite cylinder for buckling. *Compos. Struct.*, **95**, 346–353. 4, 36, 44, 45

Rozvany, GIN, Zhou, M., & Birker, T. 1992. Generalized shape optimization without homogenization. *Struct Multidisc Optim*, **4**, 250254. 108

Salzar, R.S. 1995. Functionaly graded metal matrix composite tubes. *Compos. Eng.*, **5**, 891–900. 3

Sharma, N.D., Maranganti, R., & Sharma, P. 2007. On the possibility of piezoelectric nanocomposites without using piezoelectric materials. *Journal of the Mechanics and Physics of Solids*, **55**, 23282350. 107, 108, 114

Sharma, N.D., Landis, C.M., & Sharma, P. 2010. Piezoelectric thin-film super-lattices without using piezoelectric materials. *J. Appl. Phys.*, **108**, 024304. 108

Shi, D.L., Feng, X.Q., Huang, Y.Y., Hwang, K.C., & Gao, H. 2004. The Effect of Nanotube Waviness and Agglomeration on the Elastic Property of Carbon Nanotube-Reinforced Composites. *J. Eng. Mater. Technol*, **126**. 38

Shojaee, S., Mohamadian, M., & Valizadeh, N. 2012. Composition of isogeometric analysis with level set method for structural topology optimization. *Int. J. Optim. Civil Eng.*, **2**. 123

Shokrieh, M.M., & Rafiee, R. 2010a. Investigation of nanotube length effect on the reinforcement efficiency in carbon nanotube based composites. *Compos. Struct.*, **92**, 2415–2420. 36

Shokrieh, M.M., & Rafiee, R. 2010b. Prediction of mechanical properties of an embedded carbon nanotube in polymer matrix based on developing an equivalent long fiber. *Mech. Res. Commun.*, **37**, 235–240. 36, 38

Shokrieh, M.M., & Rafiee, R. 2010c. A review of the mechanical properties of isolated carbon nanotubes and carbon nanotube composites. *Mech. Compos. Mater.*, **46**. 4, 35, 36

Shokrieh, M.M., & Rafiee, R. 2010d. Stochastic multi-scale modeling of CNT/polymer composites. *Comput. Mater. Sci.*, **50**. ix, 36, 38, 39, 40, 44

Shokrieh, M.M., & Rafiee, R. 2012. Development of a full range multi-scale model to obtain elastic properties of CNT/polymer composites. *Iranian Polym. J.*, **21**, 397–402. 35

Sigmund, Ole. 1997. On the Design of Compliant Mechanisms Using Topology Optimization. *Mech. Struct. Mach.*, **25**. 108

Sigmund, Ole. 2001a. A 99 line topology optimization code written in Matlab. *Structural and Multidisciplinary Optimization*, **21**. 108

Sigmund, Ole. 2001b. Design of multiphysics actuators using topology optimization Part I: One material structures. *Comput. Methods Appl. Mech. Engrg.*, **190**, 6577–6604. 108

Svanberg, K. 1987. The method of moving asymptotes- a new method for structural optimization. *Int. J. Numer. Meth. Eng.*, **24**, 359–373. 23

Thanedar, P.B., & Chamis, C.C. 1995. Reliability considerations in composite laminates tailoring. *Comput. and struct.*, **54**. 4

Togan, V., & Daloglu, A. 2006. Reliability and reliability based design optimization. *Turkish J. Eng. Env. Sci.*, **30**, 237–249. 58

Triantafillou, TC., & Gibson, LJ. 1989. Debonding in foam-core sandwich panels. *Mater. and Struct.*, **22**, 64–69. 65

Wang, Michael Yu, Wang, Xiaoming, & Guo, Dongming. 2003. A level set method for structural topology optimization. *Comput. Methods Appl. Mech. Engrg.*, **192**, 227–246. 108, 115, 116

Wu, SC., Liu, GR., Zhang, HO., & Zhang, GY. 2009. A node-based smoothed point interpolation method (NS-PIM) for thermoelastic problems with solution bounds. *International Journal of Heat and Mass Transfer*, **52**, 1464–1471. 87

Yudin, P. V., & Tagantsev, A. K. 2013. TOPICAL REVIEW: Fundamentals of flexoelectricity in solids. *Nanotechnology*, **24**, 36pp. 107

Zehnder, N., & Ermanni, P. 2006. A methodology for the global optimization of laminated composite structures. *Compos. Struct.*, **72**, 311–320. 3

Zhao, X., Bordas, SPA., & Qu, J. 2013. A hybrid smoothed extended finite element/level set method for modeling equilibrium shapes of nano-inhomogeneities. *Comput Mech.*, **52**, 1417–1428. 68

Zhao, Yan-Gang, & Ono, Tetsuro. 1999. A general procedure for first/second-order reliability method (FORM/SORM). *Struct. Saf.*, **21**, 95–112. 14

Zhou, M., & Rozvany, G.I.N. 1991. The COC algorithm part II: topological, geometry and generalized shape optimization. *Comput. Meth. Appl. Mech. Eng.*, **89**, 197–224. 23, 71

Zhu, W.Y., Fu, J.Y., Li, N., & Cross, L. 2006. Piezoelectric composite based on the enhanced flexoelectric effects. *Applied Physics Letters*, **89**, 192904. 123

Zhuang, X., Augarde, C., & Mathisen, K. 2012. Fracture modeling using meshless methods and level sets in 3D: framework and modeling. *Int. J. Numer. Meth. Engng.*, **92**, 969–998. 68

Zong, Z., Lam, KY, & Zhang, YY. 2005. The multidomain differential quadrature approach to plane elastic problems with material discontinuity. *Math. and comput. model.*, **41**, 539–553. 74

Zubko, P., Catalan, G., & Tagantsev, A. K. 2013. Flexoelectric effect in solids. *Annu. Rev. Mater. Res.*, **43**, 38742. 108

Academic Curriculum Vitae

Hamid Ghasemi Meyghani

Institute of Structural Mechanics
Bauhaus-Universität Weimar
Marienstrasse 15, 99423 Weimar, Germany
Email: hamid.ghasemi@uni-weimar.de
Date of Birth: June 06th, 1981
Place of Birth: Arak, Iran
Citizenship: Iranian

Education

- Ph.D: Computational Mechanics, Institute of Structural Mechanics, Bauhaus-Universität Weimar, Germany, 2012-2016.
- M.Sc: Mechanical Engineering, Iran University of Science and Technology, Tehran, Iran 2004-2006
- B.S: Mechanical Engineering, Tabriz University, Tabtiz, Iran 1999-2003

Publications

1. Hamid Ghasemi, Harold park, Timon Rabczuk *A level-set based IGA formulation for topology optimization of flexoelectric materials*. Comput. Methods Appl. Mech. Engrg. 313: 239-258, 2017

2. Hamid Ghasemi, Pierre Kerfriden, Stephane P. A. Bordas, Jacob Muthu, Goangseup Zi, Timon Rabczuk *Probabilistic multiconstraints optimization of cooling channels in ceramic matrix composites*. Composites Part B 81:107-119, 2015

3. H. Ghasemi, R. Brighenti, X. Zhuang, J. Muthu, T. Rabczuk *Optimum fiber content and distribution in fiber-reinforced solids using a reliability and NURBS based sequential optimization approach*. Structural and Multidisciplinary Optimization 51(1):99-112, 2015

4. Hamid Ghasemi, Pierre Kerfriden, Stephane P. A. Bordas, Jacob Muthu, Goangseup Zi, Timon Rabczuk *Interfacial shear stress optimization in*

sandwich beams with polymeric core using non-uniform distribution of reinforcing ingredients. Composite Structures 120:221-230, 2015

5. H. Ghasemi, R. Brighenti, X. Zhuang, J. Muthu, T. Rabczuk *Optimization of fiber distribution in fiber reinforced composite by using NURBS functions*. Computational Material Science 83: 463473, 2014

6. H. Ghasemi, Roham Rafiee, X. Zhuang, J. Muthu, T. Rabczuk *Uncertainties propagation in metamodel-based probabilistic optimization of CNT/polymer composite structure using stochastic multi-scale modeling*. Computational Material Science 85: 295-305, 2014